AN INVESTIGATION OF THE MAGNETIC STRUCTURE IN SMALL REGULARLY SHAPED PARTICLES USING TRANSMISSION ELECTRON MICROSCOPY

by Stephen McVitie

submitted for the degree of Ph.D at the University of Glasgow.

September 1988

'Um sick and disgusted and um no sayin' another word'

Jock Wallace c.1980.

ACKNOWLEDGEMENTS

This thesis would not have been possible without the help of many others throughout the course of this work. Foremost I would like to thank Professor J. N. Chapman for his help and invaluable discussions and Professor R. P. Ferrier for his encouragement and provision of the electron microscope facilities in the Solid State Group at the University of Glasgow. Also I am grateful to Professor C. D. W. Wilkinson and Dr S. P. Beaumont for the provision of facilities for specimen preparation in the Department of Electrical Engineering. I must thank Professor Chapman and Dr I. R. McFadyen for assistance in operating the HB5 STEM at Glasgow. I would also like to thank Dr C. P. Scott for his help with the calculations given in the appendix.

For maintenance of the electron microscope facilities at Glasgow I would like to thank Mr J. Simms and Miss M. Low for maintaining the CTEM machines and Dr W. A. P. Nicholson and Mr A. Howie for maintaining the HB5 STEM. For help in specimen preparation I am especially indebted to Mr A. Stark for his unfailing patience and all who assisted me in the Sub-Nanometre Group in Electrical Engineering.

Preparation of this thesis would not have been possible without the help of Miss M. Low and Mrs M. Waterson who prepared many of the diagrams and Mr I. McVicar for assistance in producing the photographic prints.

Finally I would like to thank SERC for the provision of a grant and equipment.

DECLARATION

This thesis is a record of the work carried out by me in the Department of Physics and Astronomy at the University of Glasgow. The work described herein is my own with the exception of the manufacture of the Si_3N_4 membranes (chapter 4) which were provided by the Department of Electrical Engineering. Some of the work given in this thesis can be found in the following papers:

'An investigation of the magnetic structures in small regularly shaped particles', S. McVitie and J. N. Chapman, Proc. 11th Int. Cong. on Electron Microscopy, eds. T. Imura, S. Maruse and T. Suzuki, Japanese Society of Microscopy Tokyo, p1735 (1986).

'Magnetic structure determination by scanning transmission electron microscopy', J. N. Chapman, S. McVitie and I. R. McFadyen, Proc. 5th Pfefferkorn Conf. on Physical Aspects of Characterisation of Materials, (AMF O' Hare Chicago), p221 (1986).

'Magnetic structure determination in small regularly shaped particles using transmission electron microscopy', S. McVitie and J. N. Chapman, IEEE Tans. Mag., **MAG-24**, p1778 (1988).

This thesis has not previously been submitted for a higher degree.

CONTENTS

SUMMARY

The work described in this thesis is a study of the domain structures in small regularly shaped particles of a soft magnetic material using the techniques of Lorentz microscopy. By using such a material the observed domain structures are primarily determined by the shape of the particle. The basic concepts of ferromagnetism and a discussion of the theoretical framework of micromagnetics is given in chapter 1.

Electron microscopy is a powerful tool for the observation of the magnetisation distributions within magnetic materials and in chapter 2 the most important techniques are reviewed in context with the two modes used throughout this work namely the Fresnel and differential phase contrast (DPC) mode. Also briefly discussed in chapter 2 is the theory of image formation in a scanning transmission electron microscope (STEM) for DPC imaging which allows the induction distributions within thin film magnetic objects to be mapped.

Previous studies of regularly shaped magnetic particles are reviewed in chapter 3 along with a discussion of the different types of domain walls encountered in magnetic thin films. The shapes to be studied in this project are introduced in this chapter. Fabrication of the particles was performed using the technique of electron beam lithography and the implementation of this process is described in chapter 4.

The main body of results in this thesis is presented in chapters 5-7. Chapter 5 deals with preliminary studies of the square and rectangular shapes (PAT1) using the Fresnel mode which was useful in identifying the domain geometries within the particles. The regular domain structures observed in these particles were categorised and the variation of the domain structure with the precise shape of the particle was noted. Further

investigation of these structures was made using the DPC mode and described in chapter 6. This mode allowed confirmation of the domain structures observed in chapter 5 to be made as well as providing direct observation of stray fields emanating from particles which did not possess flux closure domain configurations. The techniques used to obtain quantitative information on the domain wall widths are also given in chapter 6. Variation of the particle shape and its influence on the observed domain structures is the subject of chapter 7 where the diamond (PAT2) and triangular (PAT3) shapes are investigated.

Chapter 8 contains conclusions drawn from the observations of chapters 5-7 along with suggestions for possible continuation of this work.

CHAPTER 1

FERROMAGNETISM IN THIN FILMS

1.1 Ferromagnetic Materials

A ferromagnetic material is one which possesses a spontaneous magnetic moment below a certain temperature called the Curie temperature. The existence of this magnetic moment indicates that the atomic moments of the material have a strong interaction which tends to order them to lie parallel to one another. Orbital motion of the electron and its own intrinsic spin contribute to the net atomic moment of the individual atom. In paramagnetic materials the spins of the atoms are randomly oriented due to thermal agitation and a field of ~$3x10^9$ $A.m^{-1}$ would be required to align them. Alignment of the atomic magnetic moments in ferromagnetic materials was proposed to be possible by the postulation of a molecular field (Weiss 1907) within the material which itself is of the order $3x10^9 A.m^{-1}$. The existence of this field means that parallel spin orientations are favoured for the atomic moments in ferromagnetic materials up to the Curie temperature at which point the thermal agitation becomes energetically sufficient to overcome this field.

The nature of the interaction between the atomic moments in a ferromagnetic material can be understood in terms of a quantum mechanical exchange force. For a system of two electrons the electrostatic energy depends on the orientation of the two spins. In the case of two electrons with parallel spins this energy is a minimum when the spatial part of the wavefunction is anti-symmetric. The total wavefunction of the system is the product of the spatial and spin wavefunctions and for a system of electrons

this must be anti-symmteric by the Pauli exclusion principle. Heisenberg (1928) proposed the concept of an exchange interaction which provides a contribution to the total energy of a ferromagnetic body and is itself responsible for ferromagnetism.

1.2 Total Energy of a Magnetic System

Consideration of the different energy contributions which make up the total energy associated with a ferromagnetic material leads to an explanation of the varied magnetisation distributions found in magnetic materials.

1.2.1 Exchange energy

As explained in the previous sections the exchange interaction is fundamental to the existence of ferromagnetic phenomena. It is related to the relative orientation of the spins of the atomic moments and for two atoms with spins $\underline{s}_i$ and $\underline{s}_j$ separated by a distance r_{ij} the potential energy is given by,

$$E_A = - J(r_{ij})\, \underline{s}_i \cdot \underline{s}_j \qquad (1.1)$$

where J(r) is called the exchange integral. It is positive for ferromagnetism and normally decreases as the distance r_{ij} increases and for ferromagnetic materials only nearest neighbour interactions need be taken into account. The negative sign in the equation means that the lowest exchange energy configuration is for parallel spins. Also the exchange interaction strength means that within the material the angle between the spins θ_{ij} will be small.

With α, β and γ representing the direction cosines of the magnetisation vector, $\underline{M} = M_S(\alpha(\underline{r}),\beta(\underline{r}),\gamma(\underline{r}))$ the exchange energy can be written as,

$$E_A = A \int_v [(\nabla \alpha)^2 + (\nabla \beta)^2 + (\nabla \gamma)^2] \, dV \qquad (1.2)$$

where A is the exchange constant of the material given by

$$A = \frac{k J S^2}{a} \qquad (1.3)$$

with a being the lattice constant of the material, k a constant depending on the crystalline structure (=1 for simple cubic, 2 for bcc and 4 for fcc) and S the magnitude of the magnetic moment of the atom. It is obvious that a consideration of the exchange energy alone would lead to completely uniformly magnetised ferromagnetic materials. This is not the case for most materials as other energy contributions do not favour this configuration.

1.2.2 Magnetostatic Energy

The magnetostatic interaction of the dipoles with magnetic fields is also a source of energy in a ferromagnetic system. In the case of demagnetising (or stray) fields the energy expression is,

$$E_m = -\frac{1}{2}\mu_0 \int_v \underline{M} \cdot \underline{H}_d \, dV \qquad (1.4)$$

where $\underline{H}_d$ is the demagnetising field which is calculated from,

$$\underline{H}_d(\underline{R}) = \frac{1}{4\pi}\int_V \frac{-\nabla.\underline{M}}{R^2} dV + \frac{1}{4\pi}\int_S \frac{(\underline{M}.\underline{n})}{R^2} dS \qquad (1.5)$$

The integration is performed over the source with $\underline{n}$ being the outward pointing unit vector normal to the surface of the object and $\underline{R}$ is the vector directed between the source and field points. Here $\nabla.\underline{M}$ is equivalent to a magnetic volume charge whereas discontinuities of $\underline{M}$ at surface boundaries can be thought of as giving a magnetic surface charge $\underline{M}.\underline{n}$. When the magnetic field is due to external sources then the energy is given by,

$$E_m = -\mu_0 \int \underline{M} \cdot \underline{H} \; dV \qquad (1.6)$$

The magnetostatic energy of a uniformly magnetised ferromagnetic body will have a large amount of stray field energy from the contributions of $\underline{M}.\underline{n}$ at the edges as in fig1.1(a). This can be reduced by forming domains such as in fig 1.1(b). The reduction in stray field energy is offset by an increase in exchange energy as the number of domains increases. Equilibrium is reached by balancing the two energy contributions to give a minimum energy configuration. The exchange energy comes from the regions separating the domains. Such regions are known as domain walls and they may also have some magnetostatic energy associated with them. The magnetisation

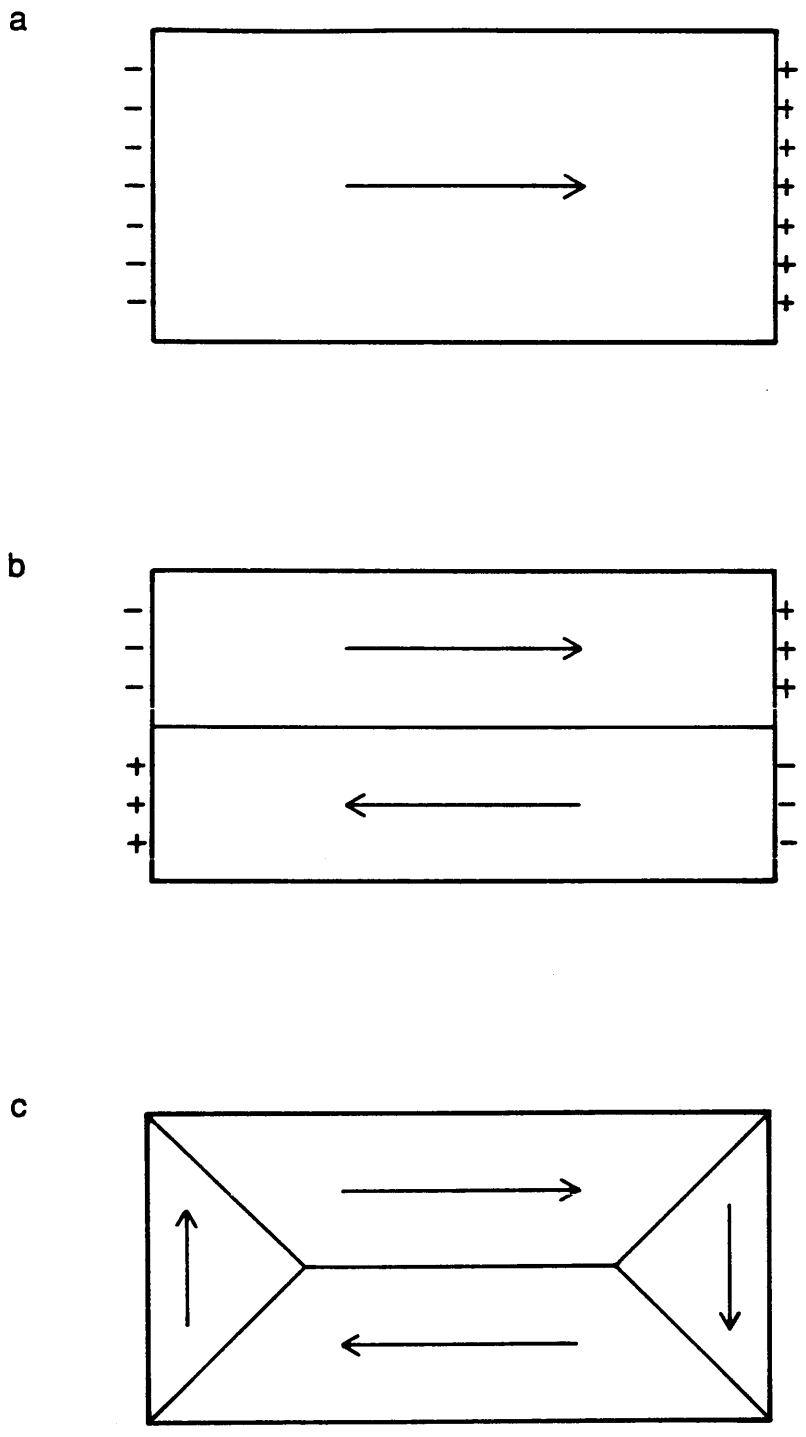

Fig 1.1 Possible magnetisation distributions in thin film objects: (a) uniformly magnetised single domain particle, (b) particle with single domain wall with reduced magnetostatic energy compared with (a), and (c) particle with solenoidal domain configuration.

distribution in these regions is considered in greater detail in chapter 3.

1.2.3 Anisotropy Energy

Magnetic anisotropy describes the dependance of the energy of a ferromagnetic body on the direction of the magnetisation. Preferred directions of magnetisation exist within some materials and these depend on the crystallographic orientation of the material. The expression for the anisotropy energy can be written as a series expansion in the terms α, β and γ and usually only the first two terms are given. Thus for a cubic crystal,

$$E_k = \int_v [K_1 (\alpha^2 \beta^2 + \beta^2 \gamma^2 + \gamma^2 \alpha^2) + K_2 \alpha^2 \beta^2 \gamma^2] dV \qquad (1.7)$$

where the crystal and co-ordinate axes are co-incident. For hexagonal or uniaxial crystals,

$$E_k = \int_v [K_1 (1 - \gamma^2) + K_2 (1 - \gamma^2)^2] dV \qquad (1.8)$$

where the c axis coincides with the symmetry axis. The constants K_1 and K_2 are called the anisotropy constants of the material.

1.3 Magnetisation Distributions in Magnetic Materials

The energy terms discussed in the previous section essentially determine how the magnetisation direction will vary throughout a magnetic material. The long range nature of the magnetostatic interaction makes

calculations of magnetisation distributions difficult. From a consideration of the different energy contributions it is seen that the exchange interaction favours uniformly magnetised structures whereas magnetostatic contributions favour having a large number of domains or a structure in which a closed flux path exists such as fig 1.1(c). Such a domain structure is termed to possess flux closure or alternatively have a solenoidal magnetisation distribution. Magnetocrystalline anisotropy means that certain directions are preferred for the magnetisation vector so that well defined domain structures are also favoured from this point of view. There are two approaches to the treatment of magnetisation distributions in magnetic materials and these are discussed in the following sections. The micromagnetic approach is that of Brown (1962).

1.3.1 The Domain Theory

The early domain theory relied on acceptance of the fact that domains existed in ferromagnetic materials (Becker 1930). Experimental evidence of this was confirmed by the observations of Bitter (1931). At that point domain and domain wall regions were considered as separate entities in the treatment of domain configurations in ferromagnetic objects. Calculation of domain wall energies was based on a one dimensional minimisation of energy and Landau and Lifschitz (1935) considered the configurations in ferromagnetic objects by calculating the energies of the domain and domain wall regions. The surface domain wall energy is used to calculate the total energy contribution from the length of the domain wall and the anisotropy and magnetostatic contributions from the domains are included to give the total energy of the system. Landau and Lifschitz considered structures in the demagnetised state in which the flux path was closed within the object

(solenoidal distribution) so that the minimum energy of the configuration was calculated by minimising the length of domain wall and anisotropy energy.

1.3.2 Micromagnetic Theory

Micromagnetic theory is based on the consideration of the forces exerted on the individual magnetic moments and involves the energy equations given in section 1.2. Theoretically the domain structure of any object should be able to be derived from application of these equations. The problem is that a rigorous treatment of these equations even for the simplest of objects leads to unmanageable equations and approximations have to be made. The micromagnetic approach is elaborated in the next section following the work of Brown (1962) and Van den Berg (1984).

1.4 Micromagnetics of Soft Ferromagnetic Materials

Equilibrium states in ferromagnetic materials can be found by calculating the effect of a small displacement of the magnetisation vector on the total energy of the system. This has been performed by Brown using variational theory to give the following relationships,

$$\underline{v} \times \left[2A \nabla^2 \underline{v} - \frac{\partial e_k}{\partial \underline{v}} + \mu_0 M_s \underline{H} \right] = 0 \quad \text{in } V \qquad (1.9)$$

$$\underline{v} \times \left[-2A \frac{\partial \underline{v}}{\partial n} - K_s (\underline{n} . \underline{v}) \underline{n} \right] = 0 \quad \text{on } S \qquad (1.10)$$

where $\underline{H}$ is the total Maxwell field and e_K is the anisotropy energy density. $\underline{M}$ has been replaced by $M_S \underline{v}$ where $\underline{v}$ is the unit vector in the direction of $\underline{M}$, and K_S is a surface anisotropy constant. The terms in the brackets are interpreted as effective fields $\underline{\mathfrak{H}}$ and $\underline{\mathfrak{H}}_S$ so that in this equilibrium condition the torques on the magnetic moments given by $\underline{M} \times \underline{\mathfrak{H}}$ is zero. An ideal soft magnetic material is characterised by a very small value of anisotropy so that only the magnetostatic and exchange energies need be considered. In such materials Van den Berg considers these energy contributions and concludes that the overall magnetisation distribution in the domains is dominated by the magnetostatic interaction whereas the exchange interaction ensures that the spins are aligned to each other locally and vary very slowly with position so that equations (1.9) and (1.10) become,

$$\underline{M} \times \underline{H} = 0 \text{ in } V \qquad (1.11)$$

$$\underline{M} \times 0 = 0 \text{ on } S \qquad (1.12)$$

which means that the following relation can be established,

$$\underline{H} = c(x,y,z)\,\underline{M} \text{ in } V \qquad (1.13)$$

Van den Berg goes on to show that the only stable solution for these equation occurs for $c(x,y,z) \geq 0$. His treatment of the equilibrium magnetisation distributions in soft magnetic thin films is based on the structures having solenoidal distributions. In his argument for this he gives the example of Hubert's (1969) calculations of two dimensional domain wall structures in which the distributions were initially assumed to be stray field free. The fact that these calculations agreed with exact calculations made by La Bonte (1969) to within a few per cent shows this assumption to be

accurate. Van den Berg thus included this condition at the start of his calculations so that,

$$\nabla . \underline{M} = 0 \text{ in } V \qquad (1.14)$$

$$\underline{M} . \underline{n} = 0 \text{ on } S \qquad (1.15)$$

along with equation (1.13) are his constitutive equations.

Using differential geometry Van den Berg (1984) showed that the magnetisation distribution in soft magnetic thin film objects decomposes into uniformly magnetised regions separated by lines of discontinuity of the magnetisation direction. These lines of discontinuity identify the positions of the domain walls within the object. The procedure for determining these domain structures (Van den Berg 1986) is outlined below,

1. The centre of any circles which touch the edge of the shape at two or more points and lie completely within the area of the object lie at positions of the domain walls.
2. The locus of the centres of these circles represent the positions of the domain walls.
3. The direction of magnetisation within each domain is easily constructed by remembering that $\underline{M} . \underline{n} = 0$ and the normal component of magnetisation is continuous at the domain walls.

An example of the structure produced by this method is derived in fig 1.2(a) for a square. This simple structure consists of four domains separated by walls in which the angle of rotation of the magnetisation is 90^{o} as in fig 1.2(b). Obviously the structure is not completely unique as the magnetisation direction can be rotated by 180^{o}. Van den Berg also pointed out that other structures may be constructed by dividing the shape into subregions and

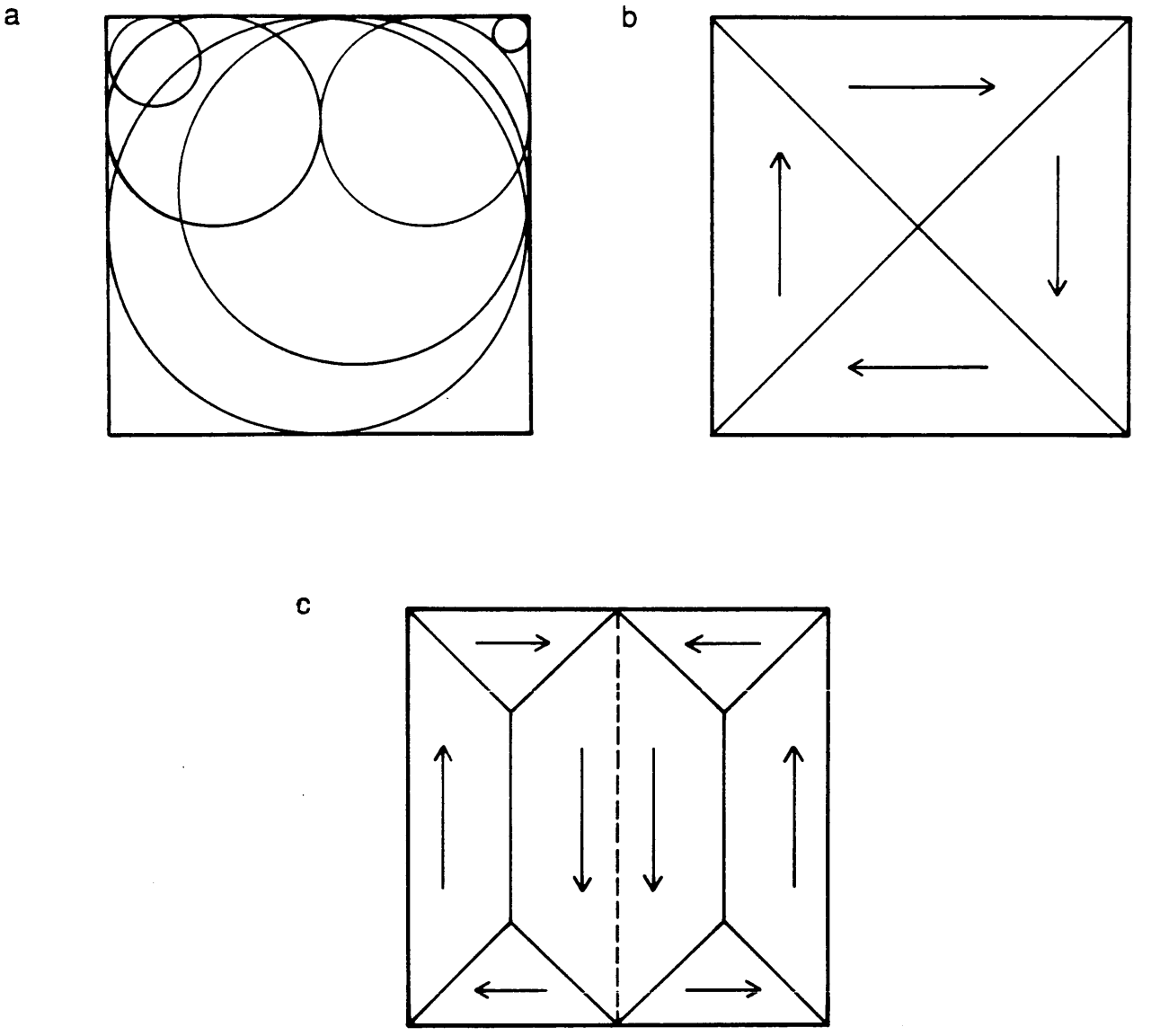

Fig 1.2 Examples of Van den Berg algorithm applied to regularly shaped particles. (a) The centres of the circles which lie completely within the shape define the locus of points for the position of the domain walls. (b) The simple structure for a square shape. (c) a composite structure which is made by making a sub-division within the shape and applying the algorithm to both halves.

applying the algorithm to each subregion. This is shown in fig 1.2(c) for the square shape. Not only is this a plausible structure but another structure can be made by having the line dividing the two subregions as a domain wall itself. It can be seen therefore that an infinite number of domain structures can be made from a single shape using this algorithm. One would expect the simple structures to be energetically favourable as this reduces the total domain wall length present in the structure. The significance of these predictions to the present work which involves observations of a soft magnetic material is noted and considered again in conclusion in chapter 8.

CHAPTER 2

INSTRUMENTATION AND IMAGE FORMATION IN STEM

2.1 Introduction

The purpose of this chapter is to describe the techniques of observing magnetic domains by electron microscopy. In particular the instrumentation and image formation in a STEM is considered in detail as much of the work described in this thesis was performed using an extended Vacuum Generators HB5 STEM.

Magnetic domains were first observed optically by Bitter (1931). The technique he used involved coating the surface of a ferromagnetic crystal with a drop of a colloidal suspension of fine ferromagnetic paricles. These particles accumulate at regions where magnetic charge is present and are thus attracted to the domain walls (chapter 3) in a sample. This decoration technique identifies the domain geometry at the surface of magnetic samples.

Other optical techniques include those which make use of the Kerr and Faraday effects on polarised light. The former utilises the fact that rotation of the plane of polarization of polarized light occurs upon reflection from a surface of a magnetic sample whilst the latter depends on the rotation of polarization of light transmitted through a magnetic thin film. Rotation of polarization in each case allows the magnetisation direction in the domains to be observed. Examples of these techniques are given by Roberts and Born (1954) and Dillon (1958) for the Kerr and Faraday effect respectively. A recent development involving the Kerr effect has been taken up by Argyle et al (1987) in which laser illumination is used. This technique, which

is known as the laser magneto-optical microscope (LAMOM), has a resolution of 0.25μm and has been used initially to monitor in-situ magnetisation experiments on permalloy particles.

These optical techniques are limited due to the restriction of surface observation or, in the case of the Faraday effect, to transparent materials. They are, however, useful in that dynamic experiments are easy to implement and monitor using these techniques. With the advent of the electron microscope many more methods of observing magnetic structures were made possible and these are discussed in the following section.

2.2 Magnetic Domain Observation by Electron Microscopy

There are many techniques available for observing magnetic domains using electron microscopy and for the purpose of this discussion they shall be outlined under the categories of CTEM, SEM and STEM.

The branch of electron microscopy dealing with observations of magnetic structure is termed Lorentz microscopy as it is the Lorentz force due to magnetic fields which is responsible for the interaction between the specimen and the electrons. Firstly a classical definition of the important quantities involved in the microscopy of magnetic materials will be given. Fig 2.1 shows plane wave electron illumination incident on a thin ferromagnetic foil containing two antiparallel domains separated by a domain wall. As the electrons are deviated by the Lorentz force it is possible to define a deflection angle, in this case in the x direction, to be,

$$\beta_x(x) = \frac{e\lambda}{h}\int_{-\infty}^{\infty} B_y(x,z)\,dz \qquad (2.1)$$

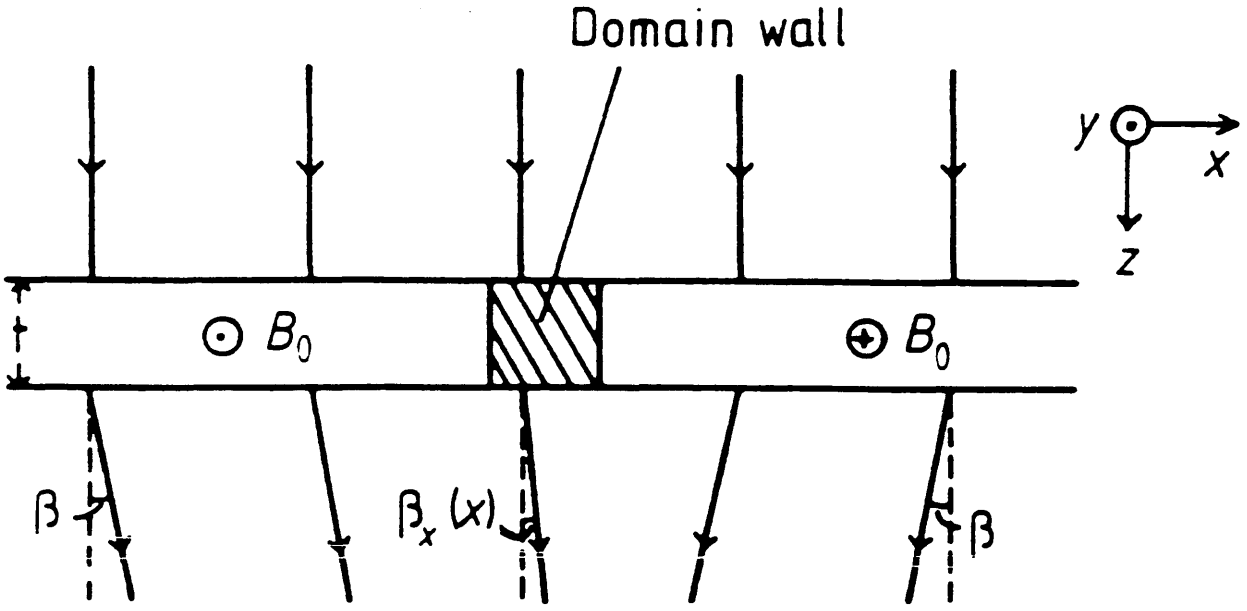

Fig 2.1 Definition of deflection angle for electrons passing through a thin film magnetic object.

where B_y (x,z) is the y component of magnetic induction at the point (x,z), e is the electronic charge, λ is the electron wavelength and h is Planck's constant. In the region of the domains the induction is constant throughout the thickness as is the saturation induction, $B_S=\mu_0 M_S$, of the material so that the deflection angle is given by,

$$\beta = \frac{e B_s \lambda t}{h} \qquad (2.2)$$

An example of the magnitude of this angle for 100keV electrons passing through a 50nm thick film of a material with a saturation induction of 1T gives a value of $\beta = 0.06$mrad. This angle is considerably less than the typical first order Bragg angle for a magnetic material which is the order of 10^{-2} rad.

2.2.1 CTEM

The diagram of fig 2.1 can be used to give a classical explanation of the most widely used modes for generating magnetic contrast in a CTEM. In order to enable the magnetic domain structure of thin films to be observed in an electron microscope the objective lens of the machine must be switched off as the field from this lens at the specimen plane in normal operation is typically in the range 0.5-1.0T which is enough to eliminate completely the magnetic structure of interest. With this lens switched off the magnification is limited and in the machine used in the present work, described in chapter 5, the top magnification available was ~5000X.

Fresnel mode

In the Fresnel mode contrast is produced by defocussing the image

forming lens so that its object plane does not coincide with the specimen plane. Contrast occurs in the final image at positions where the magnetisation direction in the specimen varies, for example at domain walls. From fig 2.1 it is seen that the electrons either side of the domain wall are deflected in different directions so that, in this case, they are converging. By making the object plane of the lens to lie below the specimen the image intensity at the position of the domain wall in the final image will be increased and observed as a narrow light band. In the case of diverging electrons the wall will be shown as a dark band. Estimation of domain wall widths can be made from the images produced by this technique by measuring the divergent wall width at different defocus values and extrapolating to zero defocus to give the width (Reimer and Kappert 1968). Problems can be encountered using this technique if one wants to measure very thin domain walls, for example in hard magnetic materials, as the measured width depends on the defocus range used due to the Fresnel edge wave (Gong and Chapman 1987). Examples of the types of images produced by this technique are given in chapters 5 and 7 of this work.

Foucault mode

The Foucault mode of Lorentz microscopy can also be explained classically with reference to fig 2.1. As electrons passing through a domain are deflected through the same angle they are all imaged at the same point in the back focal plane of the image forming lens (if one neglects scattering due to the crystalline nature of the material). Normally it is possible to insert an aperture into the beam path at this point and it can be positioned so that electrons predominantly scattered in a specific direction contribute to forming the final image. Thus all domains deflecting the electrons through this angle will appear bright in the final image whereas the rest of the image will appear dark.

Low angle diffraction

In the discussion of the Foucault mode the important factor for consideration was the intensity distribution in the back focal plane of the image forming lens. This distribution forms the far field diffraction pattern of the illuminated area of the specimen and is of interest in magnetic studies when one considers the central spot which is unscattered by the crystal lattice. In a sample containing two domains, such as that of fig 2.1, the central spot is actually split as the unscattered wave is deflected in a different direction by the oppositely directed $\underline{M}$ vector in the two domains. Analysis of the fine structure of the pattern can also give an indication of the the type of wall separating the two domains as the pattern essentialy displays a map of β (e.g. Tsukahara 1984).

The three modes so far discussed can be used to provide useful information on the magnetic structure of thin films. The Fresnel and Foucault modes can be used to give an idea of the domain structure within a material although it must be noted that the relation between the detected signal and the induction variation from the material is highly nonlinear in both cases. A more recent development on the CTEM which allows direct measurement of the induction distribution from materials is that of electron holography which is discussed in the folllowing section. This technique along with DPC imaging in STEM maintains a simple relationship between the detected signal and the induction distribution of the specimen.

Electron holography

The techniques described in the preceding paragraphs could all be explained on a purely classical basis. In order to be able to extract quantitative information using Lorentz microscopy the electron specimen interaction must be described on a quantum mechanical level. Aharonov

and Bohm (1959) showed that the phase difference of two electrons which have the same start and end points is proportional to the magnetic flux enclosed by the two paths. Thus for the case of two electrons travelling along x_1 and x_2 in fig 2.1, the phase difference is

$$\Delta\phi(x) = \frac{2\pi et}{h} \int_{x_1}^{x_2} B_y(x)\, dx \qquad (2.3)$$

where $B_y(x)$ is the average value of $B_y(x,z)$ and is defined by,

$$B_y(x) = \frac{1}{t} \int_{-\infty}^{\infty} B_y(x,z)\, dz \qquad (2.4)$$

Equation (2.3) shows that ideal ferromagnetic specimens may be regarded as pure phase objects.

Electron holography is a means by which the phase information of an object can be recovered and displayed in the final image. This is achieved through interference of the deflected electron beam from the specimen with a reference beam which passes through free space in the specimen plane. The beams are brought together by a biprism, which is essentially a charged wire at a suitable point below the specimen in the beam path. A strict requirement of this technique is that a coherent relationship exists between the specimen beam and the reference beam in order to produce the proper interference effects. This work has been developed since the late 1970's by Tonomura and co-workers.

Electron holograms produced in this way are used to generate contour

maps of fringes which correspond to lines of magnetic force (Tonomura et al 1980). This technique has been used to show stray field distributions from magnetic films (Matsuda et al 1982) and to directly verify the Aharonov-Bohm effect (Tonomura et al 1983). This technique is limited to fairly thin films due to the detrimental effect on the image quality of increased inelastic scattering in thicker films.

2.2.2 SEM

There are a number of ways of investigating the surface domain structure and stray field distribution of a magnetic specimen in a scanning electron microscope. The interaction of secondary electrons with stray fields above the specimen surface can be utilised to produce what is called Type I magnetic contrast. Alternatively Type II contrast is used to detect the domain structure at the surface and interior of a material and more recently electron spin polarization analysis has been used to investigate the surface magnetic structure of materials.

Type I contrast makes use of the fact that the deflection of secondary electrons by stray fields above the surface of the specimen affects the detected distribution as shown in fig 2.2. Use of a directionally sensitive detector allows this contrast to be displayed and has been used in the study of written tracks in digital recording media (Ferrier et al 1986).

By comparison, Type II contrast arises from the interaction of the electron beam with the magnetic induction within the material. This induction affects the trajectory of the incident beam so that it may be brought closer or deflected further from the surface of the material as shown in fig 2.3. In both cases the backscattered electron count will be affected. This technique has recently been used to study the domain structures in thin film recording heads from in-situ experiments (Ferrier and Geiss 1986).

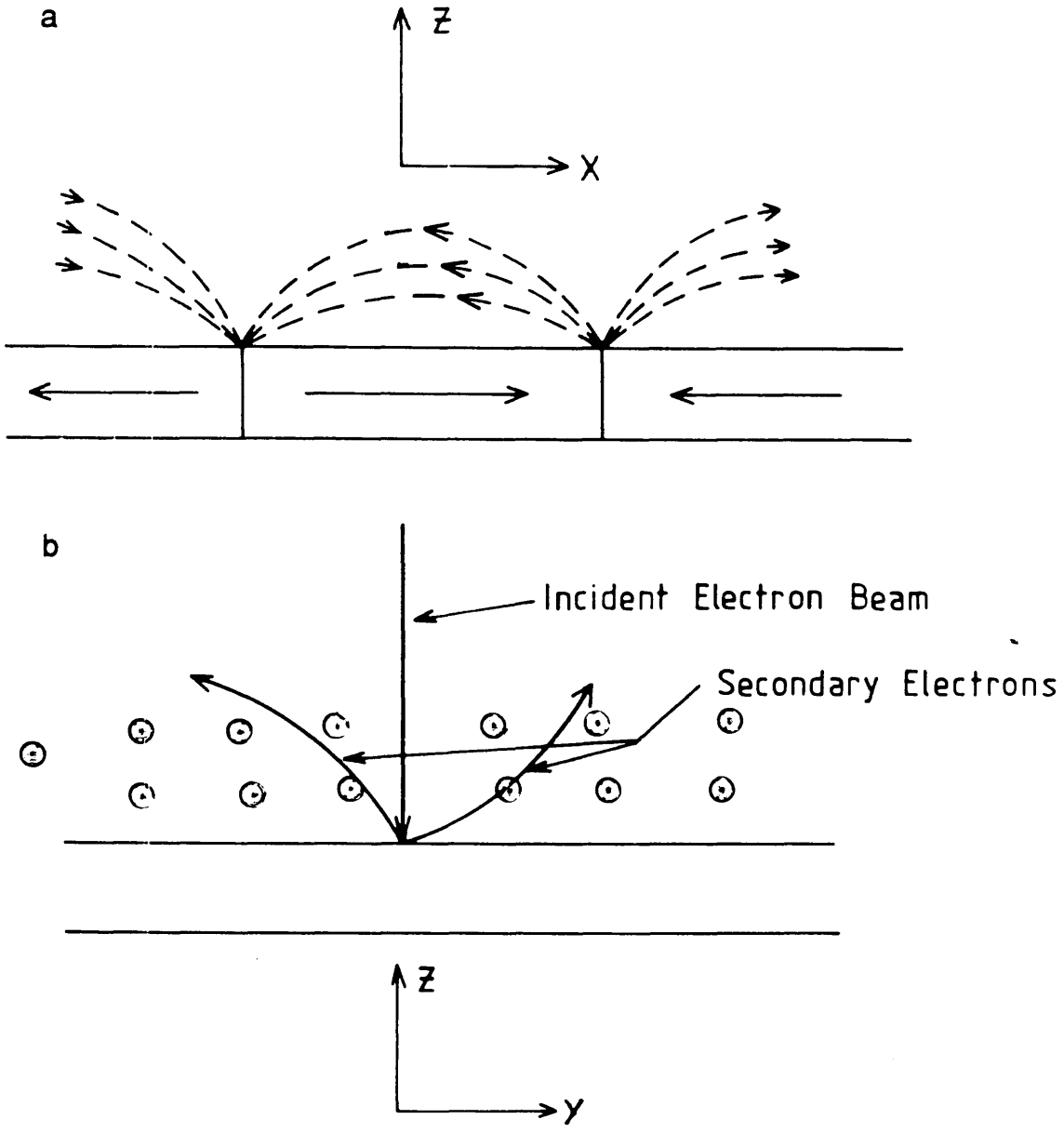

Fig 2.2 Influence of stray field on secondary electrons, in a specimen of written tracks, which can be used to detect type I magnetic contrast in an SEM.

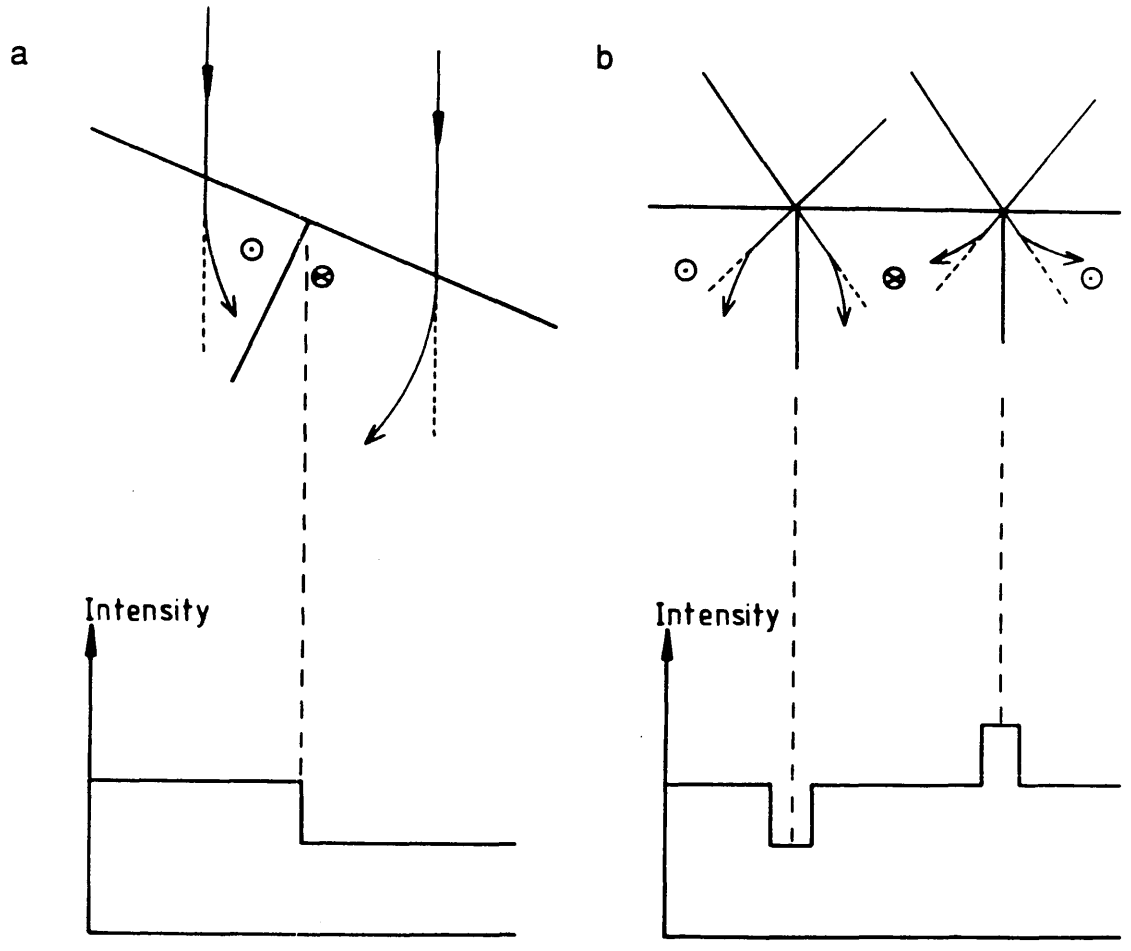

Fig 2.3 The formation of domain (a) and domain wall (b) contrast due to the effect of the in-plane component of magnetic induction on the trajectories of incident electrons which can be used to detect type II magnetic contrast.

A new method of magnetic imaging in the SEM has been developed recently which makes use of the spin polarization of secondary electrons (Koike et al (1985)). The observation of domain structure is possible because secondary electrons from a magnetic sample are polarized in a direction anti-parallel to the direction of magnetisation at the scattering point (Chorbok and Hofmann 1976). So far the resolution attainable by this mode is of the order of 40nm.

2.2.3 STEM

Fresnel and Foucault imaging may be performed on a STEM according to the principle of reciprocity (Cowley 1969). Another form of magnetic imaging which can be practised on a STEM is the differential phase contrast (DPC) mode which was first suggested by Dekkers and de Lang (1974). This technique requires a configured detector, split or quadrant for example, and contrast is achieved by taking difference signals from opposite segments of the detector. Signals recorded in this way represent maps of in-plane components of induction, integrated along the electron path, from magnetic specimens (Chapman and Morrison 1983). STEM instrumentation and the requirements necessary to implement this mode of operation are the subject of the following section.

2.3 The Scanning Transmission Electron Microscope

Images are formed in a STEM by scanning a focussed electron probe across a specimen and detecting some portion of the scattered or unscattered beam. Thus each pixel of the resulting image is acquired sequentially unlike in CTEM where the whole image is acquired

simultaneously. Reciprocity (Cowley 1969) states that any imaging mode performed in CTEM may also be performed on STEM provided that the detector response and source functions of the STEM and CTEM respectively are equivalent and there is no inelastic scattering in the material. This has been shown to be true for magnetic imaging by a number of authors e.g. Chapman et al (1979). Although the imaging modes of CTEM may be performed on STEM, under the proper circumstances, the ability to vary the detector response function in STEM allows for novel imaging modes to be performed such as the DPC mode described in this section.

The work detailed in this thesis in chapter 6 and 7 was performed on an extended VG HB5 STEM. Fig 2.4 shows the layout of this microscope with the positions of the various lenses, detectors, apertures etc. The most important features of the microscope with regard to magnetic work are discussed below.

The HB5 at Glasgow is equipped with a field emission gun the cathode of which is a single crystal tungsten wire held at a negative potential of a few kV with respect to the extraction electrode (3-4kV usually). This voltage difference gives rise to an electric field of $\sim 5 \times 10^7$ Vcm^{-1} at the top surface of the cathode (radius 50-100nm) which produces the tunnel emission of electrons. A second electrode accelerates the electrons through 100kV. Both of these electrodes have the effect of an electrostatic lens so that, in fact, the electrons appear to be originating from a virtual source. Morrison (1981) performed calculations for the operating conditions of the HB5 and found that in the present case the source of electrons can be approximated by a virtual source with a diameter of roughly 6.5nm and situated at ~171mm below the first condenser lens C1. These figures are useful as they are needed in the calculation of the incoherent probe size which is just the demagnification of this extended source by the pre-specimen lenses.

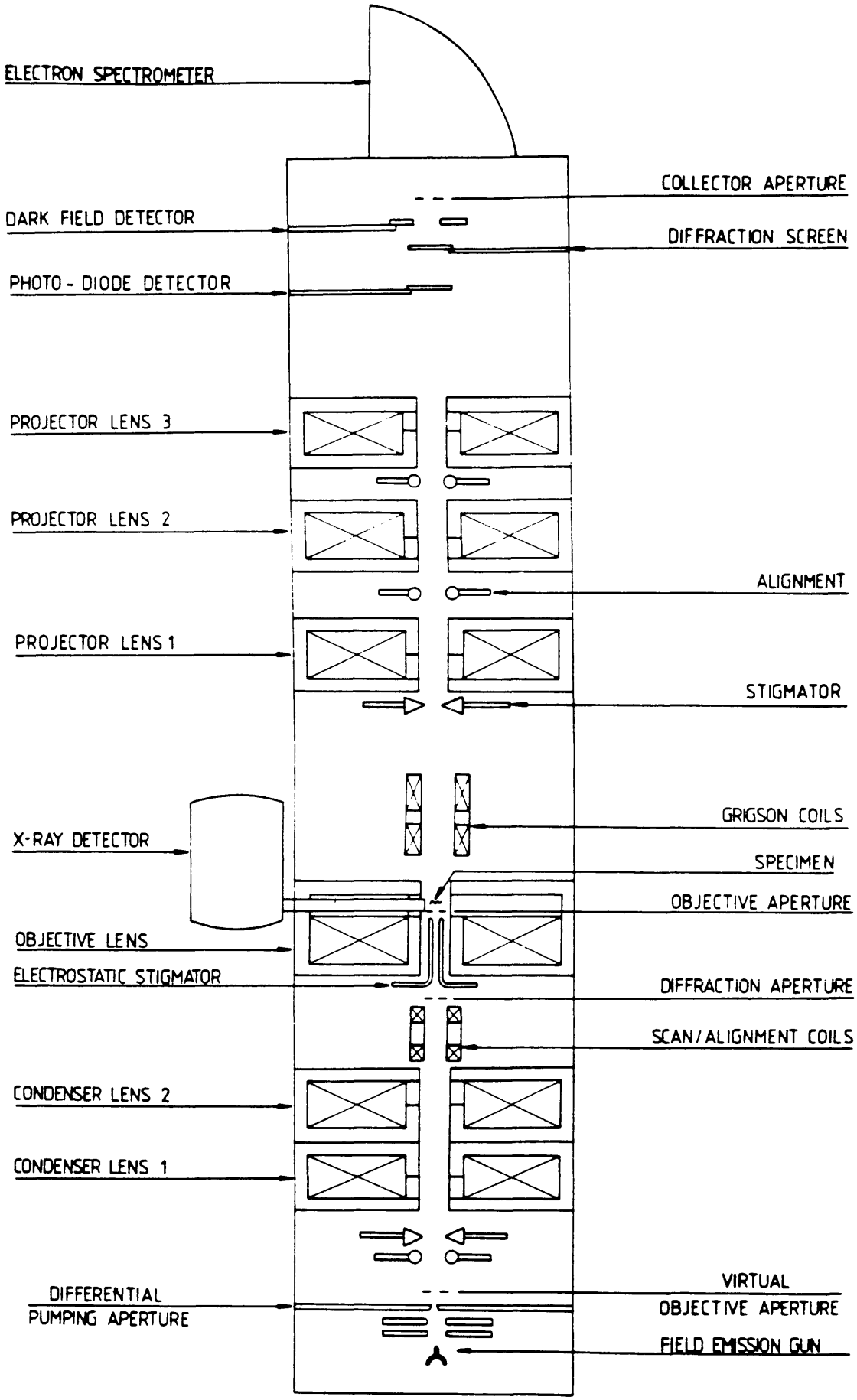

Fig 2.4 Schematic diagram showing various components of VG HB5 scanning transmission electron microscope.

Illumination of the specimen in the STEM is normally controlled by the two condenser lenses C1 and C2 and the objective lens. With the microscope in normal mode of operation the specimen is located in a magnetic field of about 0.8T, due to the objective lens field. This eliminates the domain structure in most magnetic materials. Thus magnetic work is not possible in the normal mode of operation and there are two alternatives. The first is to raise the specimen by about 20mm above its normal position and run the objective lens at a reduced excitation. The other possibility is to switch off the objective lens and use one or both of the condensers as the probe forming lenses. The latter was the mode of operation used in this work. In this configuration the condenser lens forms a demagnified image of the electron source on the specimen with the probe angle defined by the selected area aperture. Morrison (1981) has calculated probe sizes and angles for single condenser operation and in the present work C2 was used as the image forming lens. The optimum probe forming angle for a lens excitation is given by,

$$\alpha_0 = \left(\frac{4\lambda}{C_s}\right)^{\frac{1}{4}} \qquad (2.5)$$

where C_S is the third order spherical abberation coefficient of the lens.For C2 the optimum value of α_0 is 0.5mrad. This angle is achievable by using a 100μm diameter selected area aperture and can also be used to calculate the probe current which in this case works out to be 0.2nA. Another important quantity depending on the value of C_S is the coherent probe size d_C given by,

$$d_c = (C_s \lambda^3)^{\frac{1}{4}} \qquad (2.6)$$

and for C2 this is approximately equal to 10nm. The incoherent probe size, d_i, for the configuration is fixed by geometrical considerations and is equal to 6.2nm when using C2. The total probe size is calculated by adding d_i and d_c either linearly or in quadrature which for both cases gives a resolution of <20nm which is perfectly adequate for the purposes of this work, although the fact that $d_i \sim d_c$ means that the probe cannot be considered to be fully coherent.

The HB5 at Glasgow is fitted with three post specimen lenses which allow a wide range of camera lengths to be used. Such an arrangement is extremely advantageous as it means that the size of the beam at the detector may be matched to the physical dimensions of the detector. The detector used in this work was a position sensitive quadrant photodiode (Centronic model QD-100) which is a circular detector 11mm in diameter and comprises a silicon p-n junction split into 4 sections separated by inactive strips ~200μm wide. A schematic diagram showing the beam path through the microscope is given in fig 2.5. In order to give reasonable signal levels from the detector the disc of the bright field cone must be considerably bigger than the inactive regions separating the four quadrants. This also ensures that the detector will not be damaged by high current densities. For a probe forming angle of 0.5mrad a camera length of 5.4m means that the diameter of the bright field cone at the detector will be ~6-7mm. Thus for a permalloy specimen of thickness 50nm the deflection angle β_L is ~α/10. This ensures that a reasonable difference signal will be detected.

Electrons incident on the quadrant detector generate current from the photodiodes and these signals are fed into 4 matched preamplifiers where

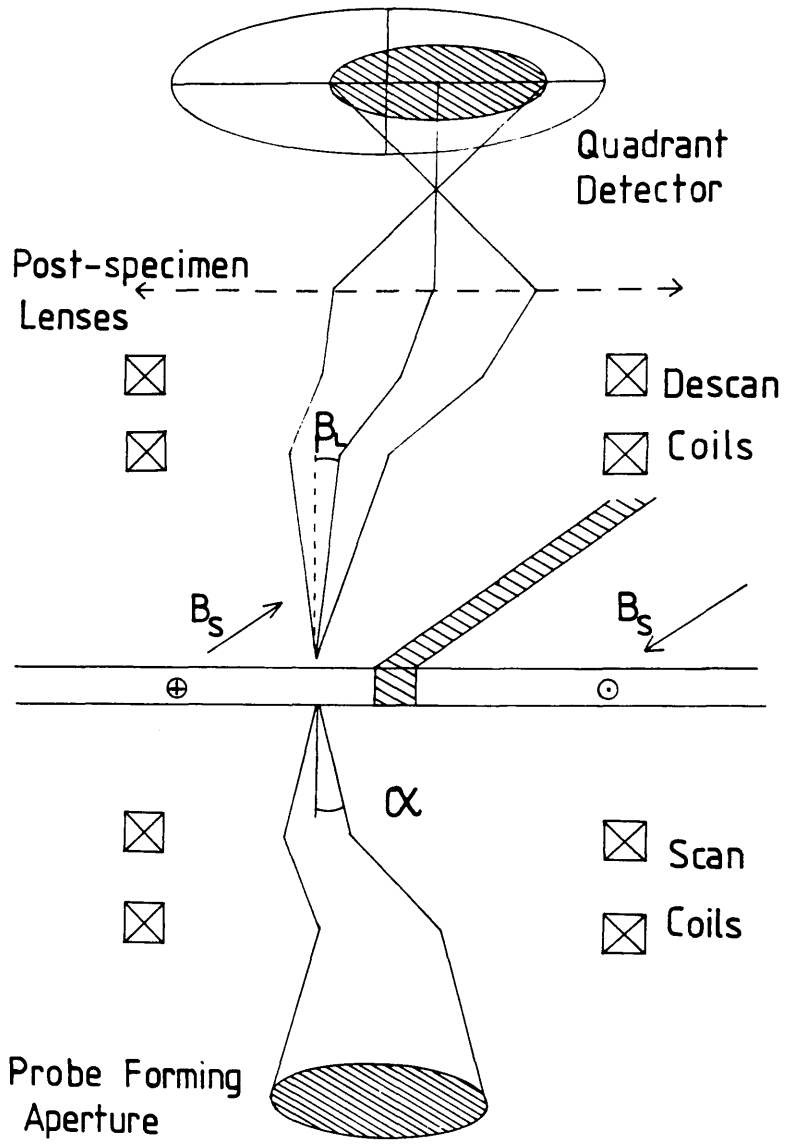

Fig 2.5 Schematic diagram showing how deflection of electron probe in STEM is measured as an imbalance current on quadrant detector.

they are converted to voltages. At this point the four signals from the detector are routed into a mixer unit where they can be combined in a number of ways before being sent to the CRT's for display. The difference signals from opposite segments of the detector provide maps of components of β as is shown in the next section. Alternatively, adding all four signals forms an incoherent bright field image. The output signals from the mixer unit can also be sent to a computer where they can be digitised and stored in a frame store. In this way image processing can be performed on images in order to extract useful quantitative information as is demonstrated in chapter 6.

2.4 Image Formation in STEM

The aim of this section is to briefly convey the ideas of image formation relevent to understanding DPC images in a STEM. Image formation in STEM has been dealt with extensively in the most general cases by many authors e.g. Cowley (1976) and Colliex and Mory (1983). In terms of the present work the HB5 was used solely for DPC imaging and only this aspect of this subject is covered here.

Image formation may simply be described in terms of the propagation of the wavefunction of the electron distribution through the various stages of the electron optical system and specimen interaction. To begin with the electron wavefunction incident on the specimen is denoted by $\psi_0(\underline{r})$ where $\underline{r}$ is the position vector in the plane of the specimen. In a scanning system with the electron probe centred on $\underline{r}_0$ the incident wavefunction is written as $\psi_0(\underline{r}-\underline{r}_0)$. The incident wavefunction is expressed as a Fourier transform of the wavefunction at the probe forming aperture $\Psi(\underline{k})$ where $\underline{k}$ is the position vector in reciprocal space. This wavefunction contains terms of the aberration function for the probe forming lens so that,

$$\Psi_o(\underline{k}) = A(\underline{k}) \exp\{ -2\pi i [-\frac{C_s \lambda^3 \underline{k}^4}{4} - \frac{\Delta z \lambda \underline{k}^2}{2}] \} \qquad (2.7)$$

$A(\underline{k})$ is the pupil function and describes the function of the probe forming aperture so that $A(\underline{k})$ is 1 inside the aperture and 0 outside it. C_S is the third order spherical aberration coefficient of the probe forming lens and Δz corresponds to the defocus of this lens with a positive value indicating a reduced lens excitation. The incident electron wavefunction can now be written as,

$$\psi_0(\underline{r}) = FT^+(\Psi_0(\underline{k})) \qquad (2.8)$$

where FT+ indicates taking a Fourier transform of the function in brackets. The interaction between the electron wave and the specimen can normally be described by a transmission function which defines how the wavefunction of the incident electron is modulated by the specimen and is given by,

$$h(\underline{r}) = \exp\{ -i \phi(\underline{r}) \} \qquad (2.9)$$

where $\phi(\underline{r})$ is the phase change of the electron wavefunction due to the specimen, this is given by equation (2.3) for a magnetic specimen, and it is assumed that there is negligible amplitude contrast. The wavefunction at the specimen exit plane is then given by,

$$\psi(\underline{r},\underline{r}_o) = h(\underline{r})\, \psi_o(\underline{r} - \underline{r}_o) \qquad (2.10)$$

Now the detectors in STEM are in the far field so that the electron wavefunction at the detector plane is given by,,

$$\Psi_d(\underline{k},\underline{r}_o) = FT^{+}(\psi(\underline{r},\underline{r}_o)) \qquad (2.11)$$

The signal intensity at the detector plane is just given by the modulus squared of equation (2.11) and this can be written as,

$$I(\underline{k},\underline{r}_o) = | \Psi_o(\underline{k},\underline{r}_o) * H(\underline{k}) |^2 \qquad (2.12)$$

where * denotes a convolution integral. In STEM the detector geometry may be easily varied so that the signal recorded actually depends on the detector response function $R(\underline{k})$ giving,

$$j(\underline{r}_o) = \int I(\underline{k},\underline{r}_o).R(\underline{k})\, d\underline{k} \qquad (2.13)$$

for the example of a split detector which is one possible configuration of the quadrant detector then $R(\underline{k})$ is given by,

$$R(\underline{k}) = 1 \quad \text{for } \underline{k} > 0$$

$$= -1 \quad \text{for } \underline{k} < 0 \qquad (2.14)$$

i.e. an antisymmetric reponse function. Detailed calculations have been performed (Cowley (1976) and Morrison (1981)) for such a detector and the results essentially reduce to the following relation,

$$j(\underline{r}_o) \propto \nabla\phi(\underline{r}_o) \qquad (2.15)$$

The Aharonov-Bohm effect discussed earlier led to an equation for the phase difference of electrons passing through a magnetic material. This equation (2.4) when viewed in conjunction with the result just stated indicates that the recorded signal in STEM using a split detector is directly proportional to a component of the local in-plane induction of the material. The above relation is certainly true with a probe size of ~10nm when investigating induction variations in soft magnetic materials where domain wall widths are well in excess of this.

2.5 Summary

In this chapter a brief outline of the available techniques for observing magnetic materials using electron microscopy was given. Advances in this field in high resolution methods include electron holography and differential phase contrast. The latter technique has been extensively developed at Glasgow and the application of it to the present work is given in chapters 6 and 7.

CHAPTER 3

REGULARLY SHAPED MAGNETIC PARTICLES AND DOMAIN WALLS IN THIN FILMS

3.1 Previous Studies

There have been many instances which show the interest in single domain ferromagnetic particles and regularly shaped magnetic thin film elements. Forty years ago, Kittel (1946) evaluated the energy associated with simple domain configurations in needles, wires and particles and compared it to that of an equivalent uniformly magnetised object. In doing this the critical dimensions at which single domain particles become favourable was calculated. His calculations predicted that uniformly magnetised structures should appear in thin films at around a thickness of 100nm whereas small particles with dimensions of 10nm would be uniformly magnetised. These figures depend on the magnitude of the magnetic parameters used in the calculations and can vary by orders of magnitude depending on the values used. Such structures will show marked differences in magnetic behaviour from bulk materials e.g.

in remanence and a high coercive force as the magnetisation changes occur only by rotation of the spins.

Much interest in regularly shaped magnetic particles with dimensions of the order of tens of microns arises from their possible use as memory elements and magnetoresistive detectors (Lo et al 1985, Tsang and Decker 1982). The work of Lo et al was involved with arrow head shaped permalloy particles which were investigated as data bit storage devices. Arrays of these particles, which had in-plane dimensions of 14 by 19μm, were made

on a network of gold sense wires which were used to measure the magnetoresistance of the individual particles. The design of these arrowhead shaped elements was such that they could sustain two binary states which corresponded to domain structures with or without a Y-shaped domain wall configuration. Non-destructive readout of 250ns was possible and the write time for each element was 50ns. The advantage of using such structures as memory devices is that they are non-volatile and radiation resistive.

Dynamic experiments on regularly shaped particles have also been performed. For example the magnetisation reversal process in narrow strips of permalloy has been studied for single and double layers (Herd et al 1979). The domain structures in squares and rectangles whose in plane dimensions are in the range 10-100μm have been observed using different techniques (Huijer and Watson 1979, Ozimek and Paul 1984 and Herman et al 1987) along with their behaviour in an external field. Domain formation and motion under an external field in small permalloy elements allows the nature of Barkhausen noise in the response of magnetoresistive elements to be investigated.

The work presented in this thesis aims to be a micromagnetic study of small particles. Although no attempt is made to follow any of the work described above the results will nevertheless be of some significance in these fields of research.

3.2 Magnetic Domain Walls In Thin Films

Domain walls occur in thin films in order to reduce the magnetostatic energy associated with the material. The nature of the domain walls varies markedly with film thickness and a discussion of the different types and the

models used to describe the variation of magnetisation within them is given below.

3.2.1 One Dimensional Models

Many models of the domain wall begin with a consideration of two anti-parallel domains as shown in fig 3.1 in which the magnetisation lies along the y-axis and the plane of the film is coincident with the x-y plane. Early models of walls were simple one dimensional variations of the magnetisation about a fixed axis. Bloch (1931) was the first to investigate the transition regions between two domains in a bulk material. The model he proposed involves magnetisation rotation about an axis perpendicular to the wall and in the plane of the film (x-axis) as shown in fig 3.1(a). The energy of such a wall in a bulk material comprises the anisotropy and exchange energy contributions only as the magnetostatic energy from the free poles, shown in fig 3.2(a), at the top and bottom surfaces of the material is negligible due to the large separation of these surfaces compared to the wall thickness in bulk materials. Also the structure of such a wall is divergence free so that there is no volume charge associated with this type of wall which is known as a Bloch wall.

As the thickness of the film decreases the magnetostatic energy from the poles at the surfaces increases and in thin films can be comparable to the other energy contributions. Neel (1955) demonstrated that in thin films another type of wall was possible in which no surface magnetic poles are generated. The rotation of magnetisation occurs in the plane of the film about an axis in the plane of the wall, the z-axis as shown in fig 3.1(b). Clearly $\nabla.\underline{M}\neq 0$ for this model and a simplified diagram showing the formation magnetic charges is shown in fig 3.2(b). The energy of such a

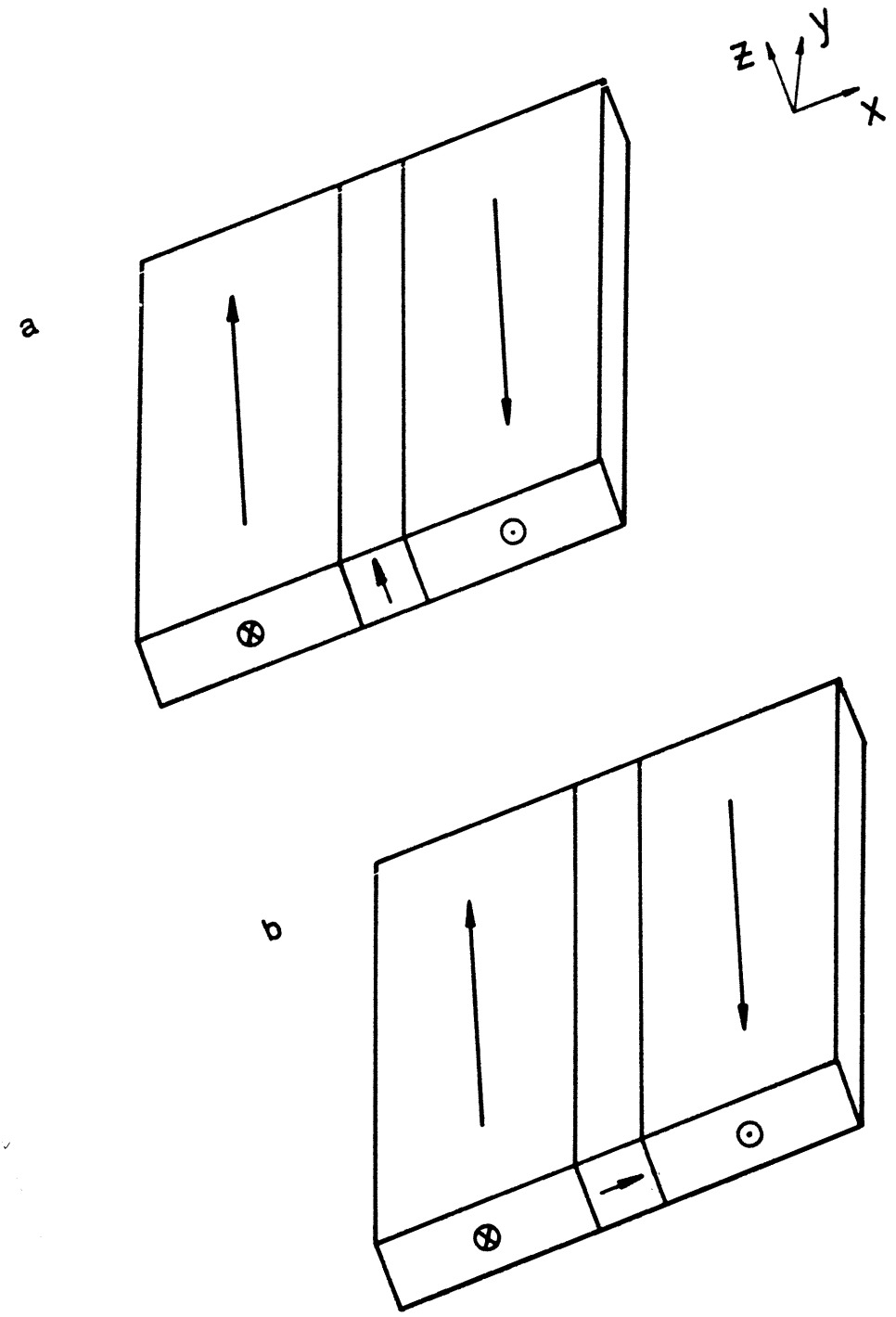

Fig 3.1 Simplified diagram showing wall rotation between antiparallel domains for a (a)Bloch and (b) Neel wall.

a

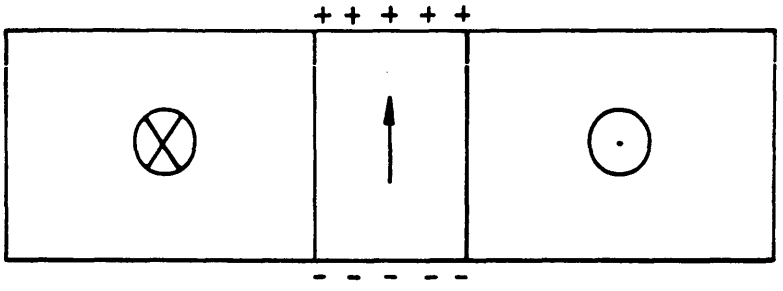

b

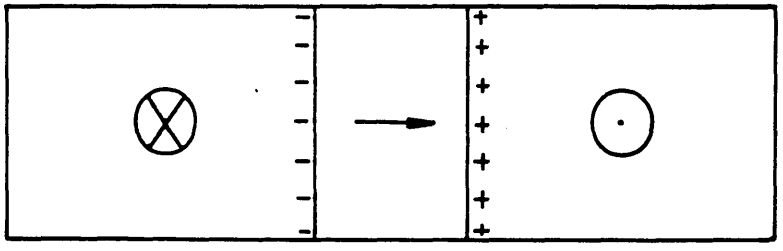

Fig 3.2 Free poles generated from simple considerations of (a) Bloch and (b) Neel wall.

configuration decreases with increasing wall thickness and as a result the thickness of Neel walls tend to be greater than the thickness of the film.

Theoretical models describing these one dimensional structures are now considered. In these models the centre of the wall coincides with the y-z plane and the rotation of the magnetisation is characterised by variation of the angle ϕ. In a Bloch wall this is the angle between $\underline{M}$ and the z-axis whereas in the Neel wall it is the angle between $\underline{M}$ and the x-axis. The models given here are good approximations for both Bloch and Neel walls which show a one dimensional variation. Landau and Lifshitz (1935) first calculated a function which describes the rotation of $\underline{M}$ in a domain wall in bulk uniaxial material and is given by,

$$\cos\phi = \operatorname{sech}\left(\frac{x}{\delta}\right) \qquad \text{where} \quad \delta = \sqrt{\frac{A}{K}} \qquad (3.1)$$

here δ is related to the domain wall width and the variation of $\underline{M}$ can therefore be given as,

$$M_y(x) = M_s \tanh\left(\frac{x}{\delta}\right) \qquad (3.2)$$

Neel's (1955) model for a 180^o wall assumes a linear rotation of spins over a distance a such that,

$$\begin{aligned} \phi &= \frac{\pi}{2} && \text{for } x \geq \frac{a}{2} \\ &= \frac{\pi x}{a} && \text{for } \frac{a}{2} < x < \frac{a}{2} \\ &= -\frac{\pi}{2} && \text{for } x \leq \frac{a}{2} \end{aligned} \qquad (3.3)$$

in this case the magnetisation rotation in the region where $\phi=\pi x/a$ is described by,

$$M_y = M_s \sin(\frac{\pi x}{a}) \qquad (3.4)$$

Calculation of the domain wall width depends on the definition used and examples are given in chapter 6 for the experimentally measured wall profiles.

Early calculations of the energy of domain walls in thin films used these formulae (Middelhoek 1963). In these calculations the exchange, anisotropy and magnetostatic energy contributions were added together and minimised with respect to the domain wall width. This value for the wall width was then substituted back into the energy expression which was then evaluated for various thicknesses of film. The results of Middelhoek's calculations which used equation (3.3) for the magnetisation variation within the wall are shown graphically on fig 3.3 for a material with magnetic constants $A=10^{-11}J.m^{-1}$, $M_S=5x10^5A.m^{-1}$ and $K=10^2J.m^{-3}$. The values shown on this graph are over-estimates of the wall energy due to the simplicity of the models used; a micromagnetic treatment of this problem gives far better results.

More detailed calculations of the structure of symmetric Neel walls were performed once that it had been discovered by Feldtkeller (1963) that the walls were much wider than previous calculations had indicated. It has since been shown by micromagnetic calculations, e.g. Collette (1964) and Riedel and Seeger (1971), that Neel walls consist of a central core region in which the bulk of the rotation of the spins occur and extended 'tails' either side of this where the spins slowly approach the direction of spin within each domain. These calculations indicate that the magnetisation variation within

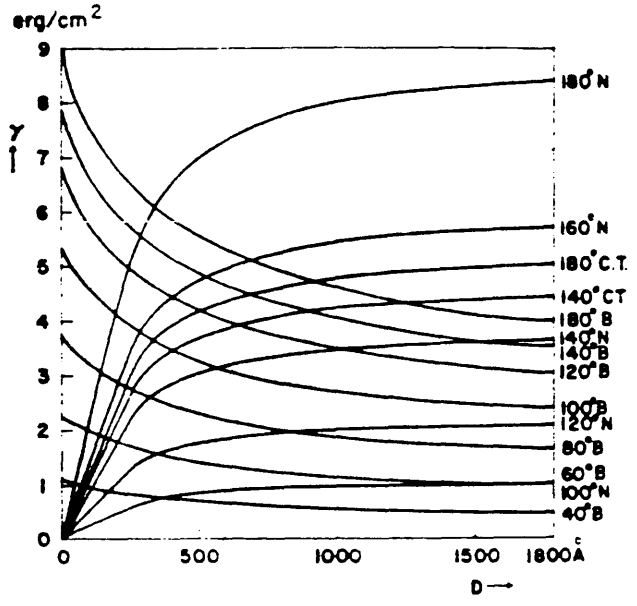

Fig 3.3 Surface domain wall energies (γ) following calculations by Middelhoek (1963) where the symbols for the walls are B-Bloch, N-Neel and CT-cross-tie.

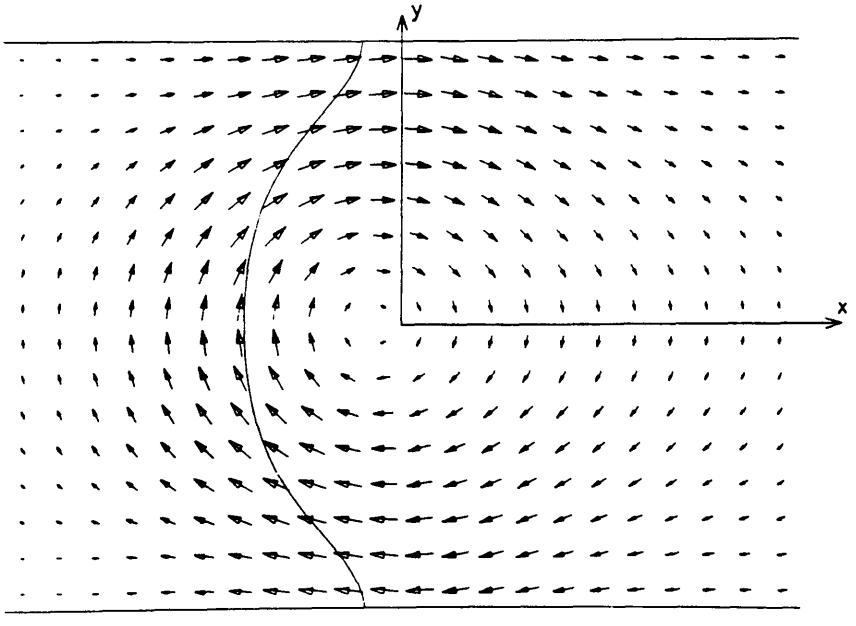

Fig 3.4 Vortex structure of 180^{o} two dimensional domain wall following Jakubovics (1974). The direction of magnetisation in the domains is along $\pm$ z.

Neel walls in very thin films films show a one dimensional nature to a good approximation as the energies of these structures are almost identical to two dimensional calculations (Holz and Hubert 1969) for very thin films.

3.2.2 Two Dimensional Wall Models

The first rigorous two dimensional treatment of domain wall structures in soft magnetic thin films was performed by LaBonte (1969). This model deals with a film of infinite extent in the plane of the film but of finite thickness. The region between two antiparallel domains is split up into an array of discrete prisms each of which is assumed to be uniformly magnetised. Each energy contribution from the individual prisms are calculated in terms of the direction of magnetisation within the prisms. The calculation process is iterative and lengthy mainly due to the magnetostatic contribution which is particularly cumbersome as the interaction energy between prisms must be calculated along with each prism's own self energy. The calculation terminates once an equilibrium distribution has been reached and takes many hours to be completed even on a large computer The resulting structure is shown in fig 3.4 (following Jakubovics 1974) with the magnetic parameters used the same as Middelhoek's for a film of thickness 100nm.

Clearly the wall structure shows an asymmetry about the y-axis.

Also the centre of the wall, where the magnetisation lies in the hard direction, does not lie in a plane but is a curved surface as indicated by the dashed line in the diagram. This distribution has an energy which is about half of that for the one dimensional models at this thickness of film. One point of note is that the wall displays marked flux closure which is characterised by very low surface pole densities. Also it can be seen that the wall is neither a simple Neel or Bloch structure but incorporates features of both these types

of walls. From the figure it is evident that in the centre of the film the wall structure resembles that of a Bloch wall whereas at the film surfaces the structure is similar to a Neel wall with opposite polarities at the two surfaces.

Very similar structures to these were calculated by Hubert (1969) who assumed that the structures were stray field free magnetisation configurations. The solutions he obtains relate to two dimensional asymmetric Bloch and Neel walls. The fact that his Bloch structures relate remarkably closely to those from LaBonte's calculation where the magnetostatic energy was low indicates that these structures closely resemble the true wall distributions in this thickness of film.

Jakubovics (1974) attempted to represent LaBonte's structure by analytic functions so that the parameters of the material could easily be changed without having to recalculate the whole distribution iteratively each time. These approximate functions matched LaBonte's structures very well although the wall energy values he calculated were slightly higher than those of LaBonte. Chapman et al (1985) used this model to compare their experimental results obtained with the DPC imaging technique and obtained excellent agreement for the domain structure and energy with the model for films of thickness 100 to 200nm.

Returning to the simple Neel and Bloch walls discussed earlier it can be seen from Middelhoek's calculations that the a transition from Neel to Bloch type walls should occur at a film thickness of around 35nm. Experimental observations of magnetic thin films indicate that, in many soft magnetic materials, a lower energy form of wall exists in the region from about t=20 to 80nm. This type of wall is known as a cross-tie wall and was first observed in the TEM by Huber et al (1958). Essentially the wall consists of sections of Neel walls of opposite polarity separated by Bloch lines shown schematically in fig 3.5. The magnetisation around the Bloch lines can either

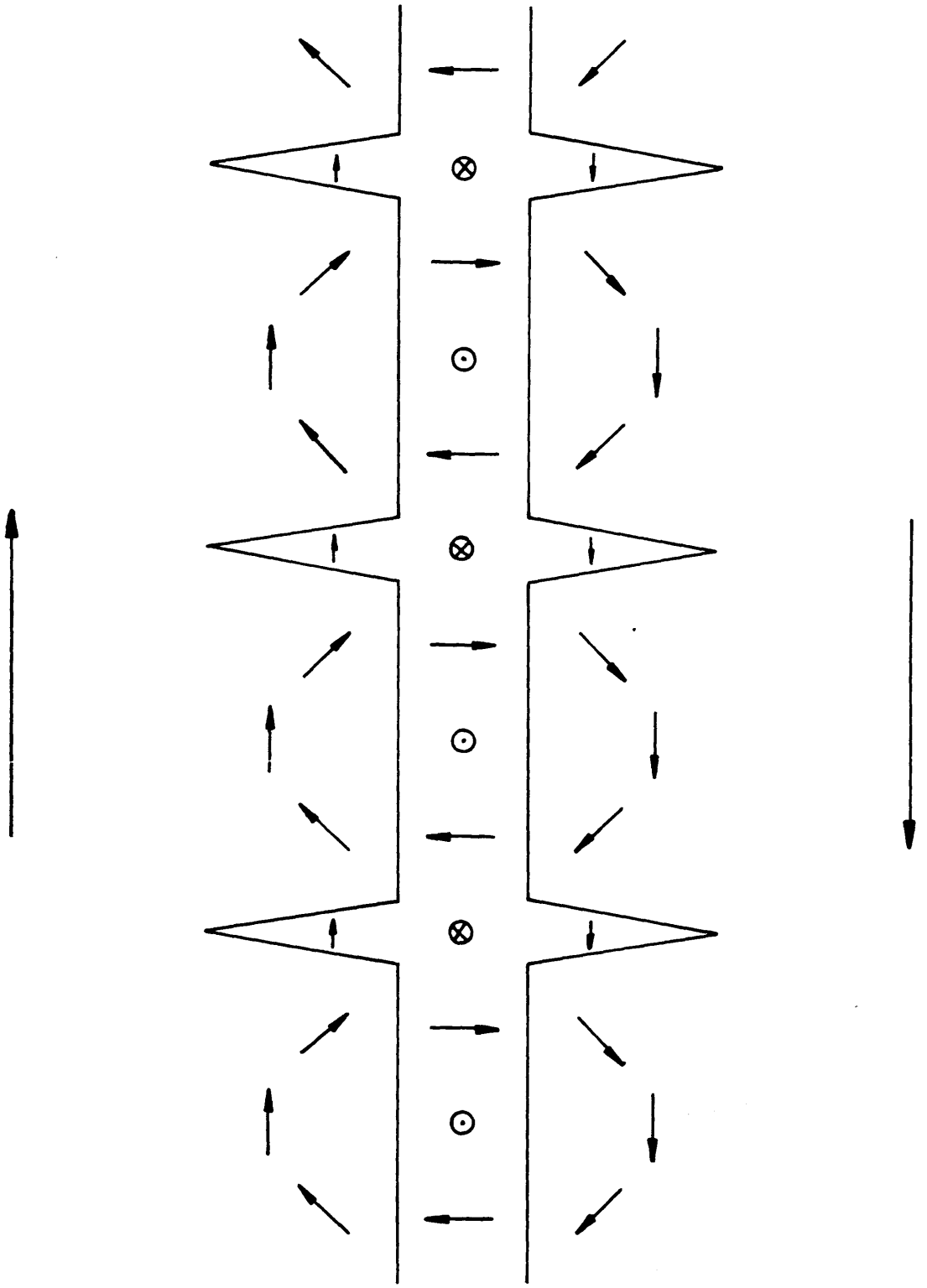

Fig 3.5 Schematic representation of magnetisation distribution in a cross-tie wall.

be convergent or circularly rotating. In the case of the convergent magnetisation there exists a low angle domain wall perpendicular to the main wall section which is known as a cross-tie. At the other point we have a circular Bloch line. Calculations (Middelhoek 1963) which have been performed on cross-tie walls have been less rigorous than those on two dimensional walls. The model proposed by Kosinski (1977) gives results which are in very good agreement with experimental observations. In his calculations he splits up the wall and surrounding region into sections and works out the total energy of each in terms of a number of parameters. Depending on which models are used for the energy of the Neel and Bloch walls it is expected that cross-ties will be present in the range of film thickness from about 20 to 60nm for a material with the parameters as used in Middelhoek's calculations if one considers the lowest energy Bloch and Neel wall models available.

3.3 Material and Shapes Used in This Work

Most of the work described in the literature uses the material permalloy which is a nickel iron alloy of low intrinsic magnetocrystalline anisotropy and low magnetostriction also. The exact composition varies but is usually around $Ni_{80}Fe_{20}$. The magnetic behaviour and properties are well documented and the composition used in this study was $Ni_{82.5}Fe_{17.5}$. The principal reason for using such a material is that as the magnetocrystalline anisotropy of this compound is low the domain structures observed in regularly shaped particles will be primarily determined by the shape and size of the particles.

In the present work it was initially proposed to study the domain structures in square and rectangular shapes of varying aspect ratio and in-plane dimensions in order to gain an insight into the transition from single to

multi-domain structures. Also as such particles tend to accommodate regular domain structures they are ideal for the detailed study of the different types of domain walls expected to appear in the particles. Previous studies of regularly shaped particles described earlier in this section involved particles with in-plane dimensions ranging from 10 to 100μm. Initially it was decided to investigate square and rectangular particles with in-plane dimensions in the micron and sub-micron scale with the thickness being restricted to less than 100nm in order to make the samples suitable for study using transmission electron microscopy.

In-plane dimensions in the range 0.25-4.0μm were chosen in the first instance. The spacing of the particles can easily be controlled, as discussed in the next chapter, and as the particles are designed to be non-interacting the possible extent of any stray flux from the particles had to be quantified. This required performing some magnetostatic calculations which are detailed below.

Consider a uniformly magnetised block, in the y direction, with dimensions $2L_1$ by $2L_2$ by $2L_3$ as shown in fig 3.6 where the notation and various quantities of interest are defined. The magnetic scalar potential of such a uniformly magnetised block is given by (Rhodes and Rowlands 1954),

$$\phi(x,y,z) = \frac{1}{4\pi} \int_s \frac{\underline{M}.\underline{n}}{/\underline{R}/} ds \qquad (3.5)$$

where $\underline{M}=(0,M_S,0)$ with M_S the saturation magnetisation of the material and $\underline{n}$ the outward pointing unit normal vector to each face of the block. It is assumed that $\nabla.\underline{M}=0$ in the calculations. By considering the top and bottom surfaces of the block in fig 3.6, where $\underline{M}.\underline{n}\neq 0$, as sheets of positive and

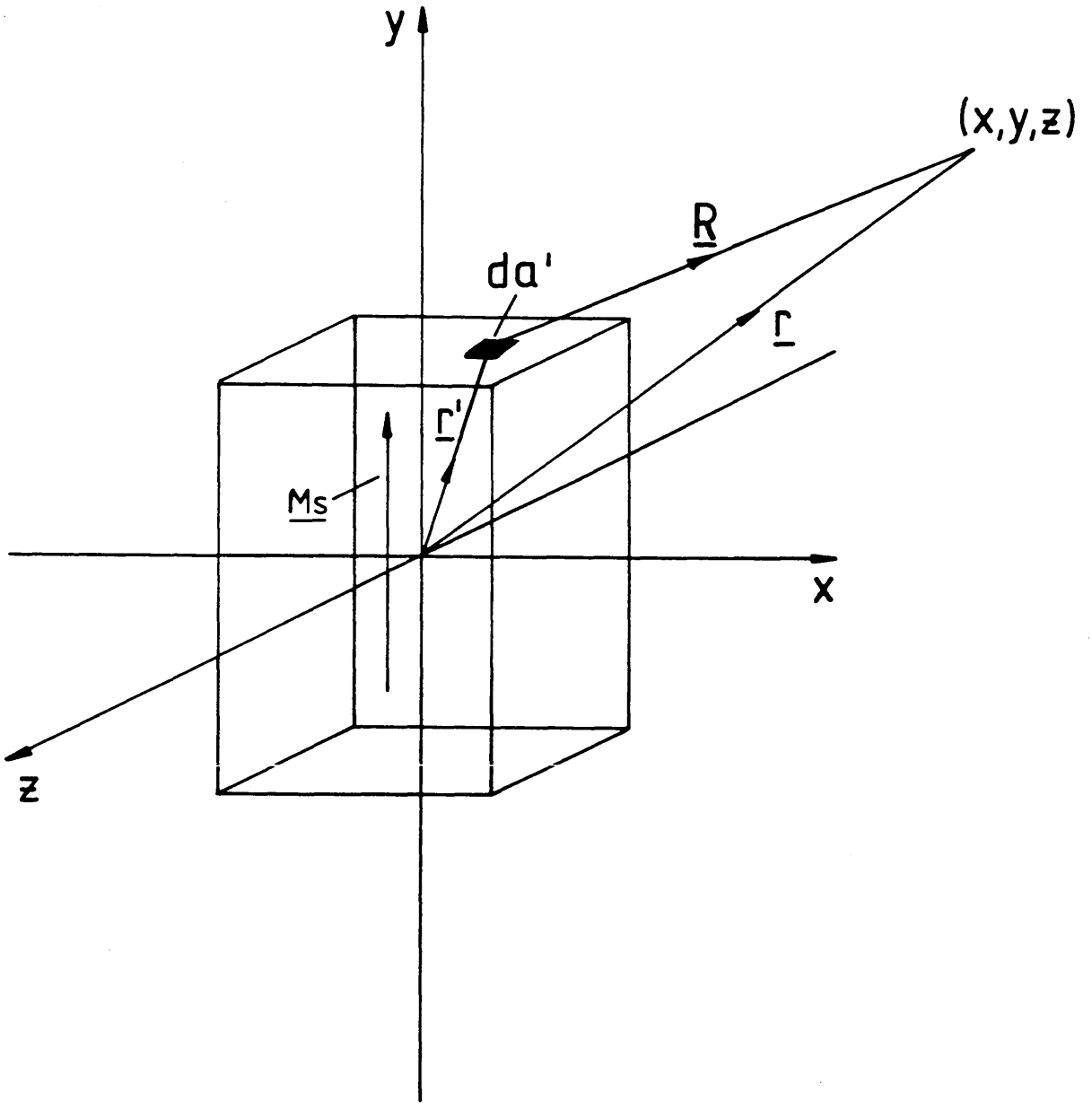

Fig 3.6 Coordinate system used for calculating magnetic field intensity at field point (x,y,z) from uniformly magnetised block of dimensions $2L_1$ by $2L_2$ by $2L_3$.

negative charge of density M_S equation (3.5) becomes,

$$\Phi(x,y,z) = \frac{M_s}{4\pi} \int_{-L_1}^{L_1} \int_{-L_3}^{L_3} \frac{dx'\, dz'}{[\,(x-x')^2 + (y-L_2)^2 + (z-z')^2\,]^{\frac{1}{2}}}$$

$$- \frac{M_s}{4\pi} \int_{-L_1}^{L_1} \int_{-L_3}^{L_3} \frac{dx'\, dz'}{[\,(x-x')^2 + (y+L_2)^2 + (z-z')^2\,]^{\frac{1}{2}}} \qquad (3.6)$$

Now the calculation of the Maxwell field is given by

$$\underline{H}(x,y,z) = -\nabla\Phi(x,y,z) \qquad (3.7)$$

which allows us to calculate the components of $\underline{H}$ by,

$$H_x = -\frac{\partial\Phi(x,y,z)}{\partial x}\,,\; H_y = -\frac{\partial\Phi(x,y,z)}{\partial y}\,,\; H_z = -\frac{\partial\Phi(x,y,z)}{\partial z} \qquad (3.8)$$

Now the integral is performed over dx' and dz' which are independent of the differentiation which is performed over (x,y,z) so that the differential may be taken inside the integral. The resulting calculations for the magnetic field give long expressions for each coordinate and these are given at the end of the thesis in the appendix. Further application of these equations to a periodic domain structure (McFadyen 1986) was also calculated.

If particles in the sample which is to be produced are single domain then

the extent and strength of the stray field must be determined in order to decide upon their spacing. Consider a block of permalloy with saturation magnetisation $M_S=8x10^5 A.m^{-1}$ and dimensions $2L_1=1.0\mu m$, $2L_2=4.0\mu m$ and $2L_3=60nm$, the magnitude of the magnetic field intensity at various points on the principal in-plane axes of the particle are given in table 3.1.

It is readily seen that the magnitude of the magnetic field falls off fairly rapidly with distance from the particle. The spacing of the particles for this pattern was chosen to be 2.0μm edge to edge and even though it is unlikely that the size of particle considered will be single domain there may be some stray flux associated with the domain structure and any interaction with neighbouring particles may affect their domain configuration. Even though the fields given in the table appear to be non-negligible at a distance of 2μm from the edge it must be remembered that we are considering a most extreme case in this particle being uniformly magnetised.

The pattern of squares and rectangles devised for study, which shall now be referred to as PAT1, is outlined in fig 3.7. The pattern is symmetrical about the line Y=X and the dimensions of the particles in the X direction in the 9 by 9 array are as follows (in μm) 4.0, 3.0, 2.0, 1.5, 1.0, 0.75, 0.5, 0.375, and 0.25. Thus particles with widely varying aspect ratios of the in-plane dimensions are to be investigated.

Although this work is mainly concerned with the square and rectangular shaped particles other shapes were also fabricated as a further study of the effect of varying the particle shape on its domain structure. Figures 3.8(a) and (b) show the two shapes considered, called PAT2 and PAT3 respectively, and the parameters which were varied. In each case the values chosen were L_1 = 1.25, 2.5, and 5.0μm with Θ = 10, 20, 30, 40, and 45°. The spacing of these particles was not calculated from magnetostatic considerations but was of approximately the same value chosen for the square and rectangular particles although this was not true for some of the

Table 3.1 Values of the magnitude of magnetic field intensity from a uniformly magnetised (along y-axis) block of dimensions $2L_1$=1μm, $2L_2$=4μm and $2L_3$=60nm. The field is given at points on the x and y axis with z=0 in all cases.

Distance in μm from x-axis	Distance in μm from y-axis	$\|H_y\|$ (A.m^{-1})
2		1433
4		187
6		66
8		29
10		15
	2.1	14.4×10^4
	4	1750
	6	190
	8	73
	10	35

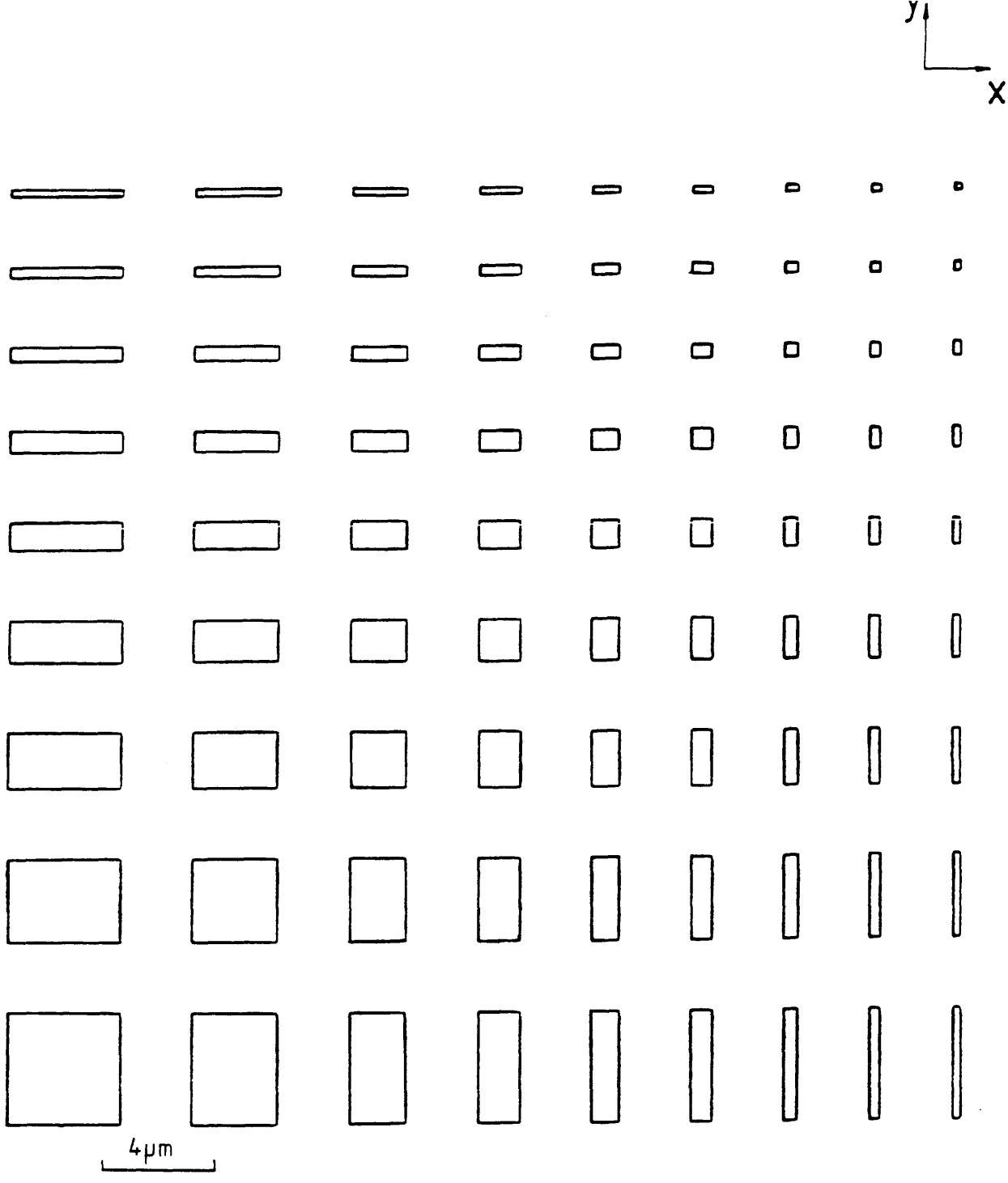

Fig 3.7 Outline of pattern of square and rectangular shapes making up PAT1.

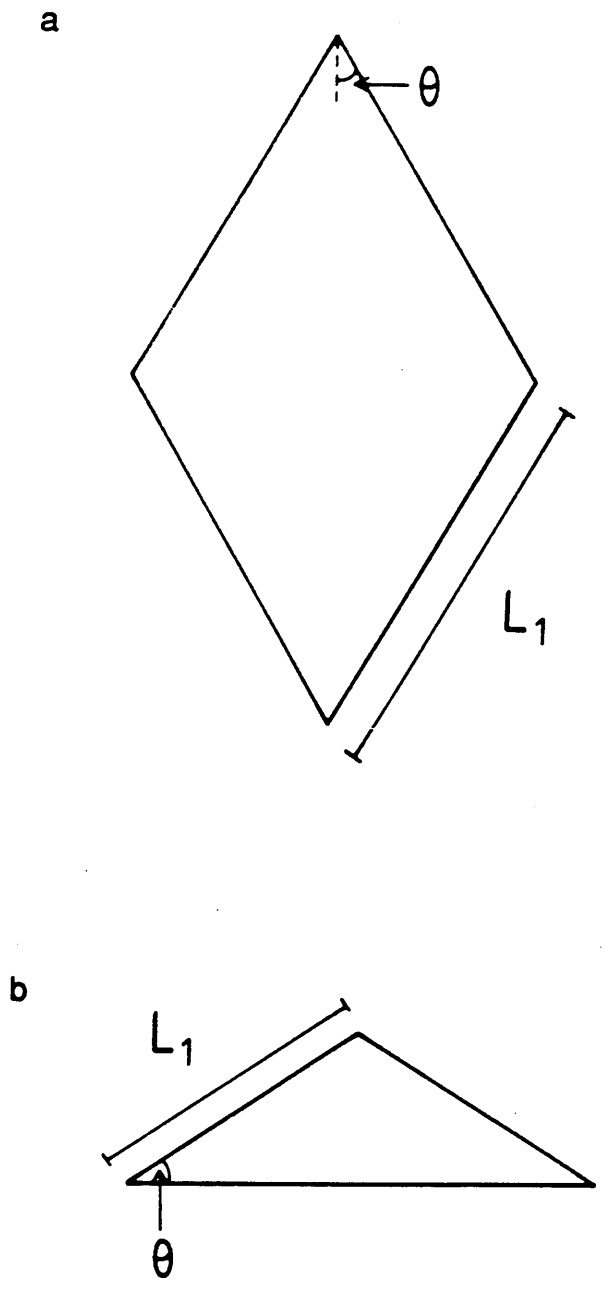

Fig 3.8 Diagram of parameters varied for (a) PAT2 and (b) PAT3.

PAT3 particles which led to some interesting results as is described in chapter 7.

CHAPTER 4

SPECIMEN PREPARATION

4.1 Introduction

In chapter 3 previous studies of regularly shaped magnetic thin films were briefly discussed. The techniques used in fabricating these shapes are varied. The most common procedure is that of standard photolithography (Glang and Gregor 1970). Two techniques of defining regular structures are then available using this process, sputter etching and lift-off. Both of these techniques have been widely used and differences between the two in terms of the magnetic behaviour of magnetic shapes produced in this way have also been studied (Van der Voort and Van den Berg 1987). The photolithography techniques are limited by a fundamental resolution limit due to the wavelength of the light used in the exposure process of about 1μm and almost all of the studies referenced in the last chapter used dimensions well in excess of this. In this chapter the technique of electron-beam lithography is described where a resolution approaching 10nm is available.

4.2 Electron Beam Lithography

The main use of electron beam lithography is in the fabrication of electronic devices on silicon wafers with sub-micron features (see chapter 1 "Electron-Beam Technology in Microelectronic Fabrication" ed. G Brewer 1980). In this section a brief description is given of the process of electron beam lithography. The individual steps involved in this process, as used in

this work, are accounted in greater detail in section 4.5.

A summary of the lithographic process is shown in fig 4.1. The first step involves deposition of resist onto the substrate which is to support the patterned material. A resist is normally a material whose molecular structure is changed when exposed with an energetic beam of radiation, electrons in this case. The required pattern is then defined by scanning a focussed electron probe across the resist. Subsequently the exposed areas dissolve out when the sample is immersed in a solution of developer in the case of a positive resist which is used here. The resist is now in the form of a negative of the pattern and the next step involves deposition of the material intended for study. Once this has been performed the excess metal and resist are removed in a process called lift-off. This is so named as the excess material lifts off the substrate when the latter is soaked in a strong solvent of the resist under conditions of moderate agitation. The remaining metal on the substrate now forms the pattern originally scanned out in the resist by the electron beam.

Optimisation of the development of an exposed pattern is dependent on many variables such as beam accelerating voltage, substrate material, resist thickness, molecular weight of resist used, and developer (composition, temperature and time). In order to perform this process in the most effective manner a number of factors had to be taken into account. A suitable substrate which would allow the patterns to be observed using TEM had to be decided upon along with the most appropriate electron resist for the production of the desired shapes. Much of the work developing the procedure used in this project follows from that of Mackie (1984).

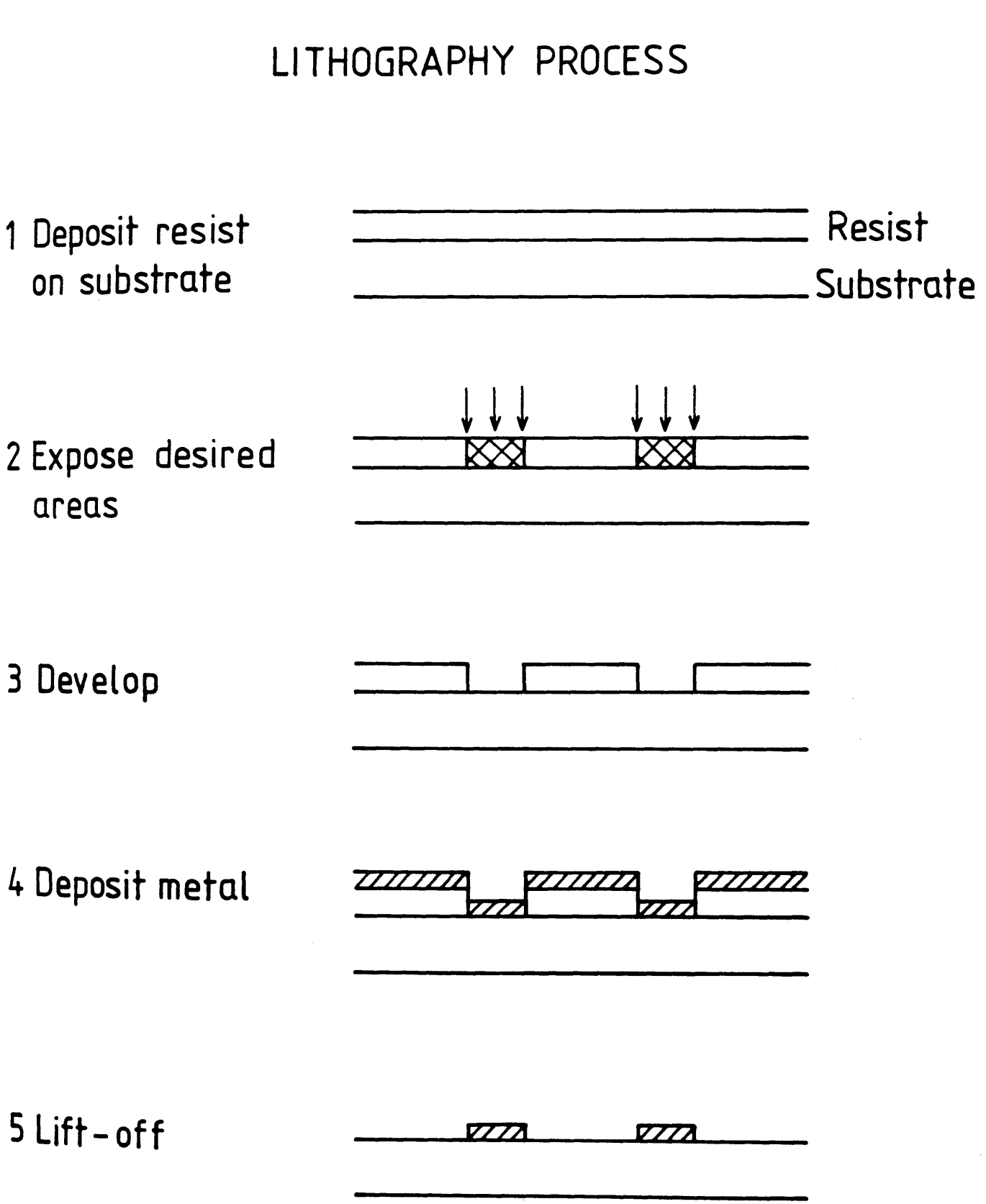

Fig 4.1 Schematic representation of lithographic process as a series of steps.

4.3 Support Material For Patterns

The most important constraint on the support material for this work is that it should be thin enough for the specimens to be imaged in TEM using 100keV electrons. Silicon nitride (Si_3N_4) membranes were considered to be suitable in this sense although a drawback is that their manufacture is fairly time consuming.

Fig 4.2 shows a diagram of a cross-section view of one such membrane. The membranes are made on a silicon wafer of thickness 335μm on which a layer of Si_3N_4 is deposited by chemical vapour deposition to a thickness of 50-70nm. Fabrication of the membranes involved a series of photolithographic and etching steps which resulted in the structure of fig 4.2. Many membranes were produced on a single silicon wafer and single membranes were scribed in the centre of a 2mm square before being broken up. This meant that they could easily fit into most TEM and STEM specimen holders.

4.4 Electron Resists

Resists are usually long chain organic polymers. In the present case only positive resists are considered in which the exposure mechanism is dominated by chain scission of the long molecules. Polymethyl methacrylate (PMMA) is a positive resist which has been used with Si_3N_4 substrates for resolution tests in electron beam lithography (Mackie 1984).

When PMMA is irradiated with an energetic beam of electrons a number of interactions occur. Electrons suffer both elastic and inelastic collisions which scatter them from the original beam. Fig 4.3 shows the typical excitation volume for a 50keV electron probe incident on PMMA of thickness

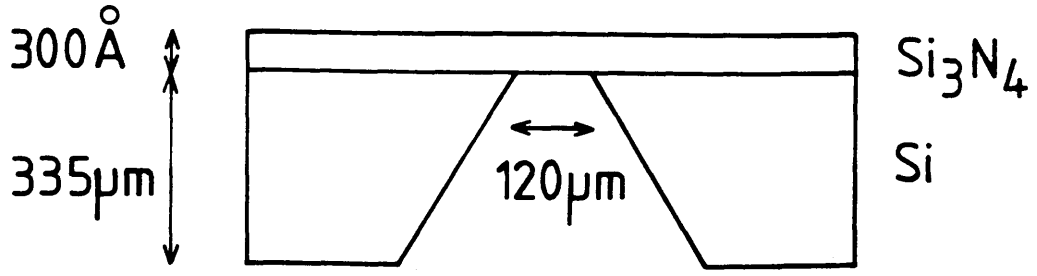

Fig 4.2 Cross-section view of Si_3N_4 membrane.

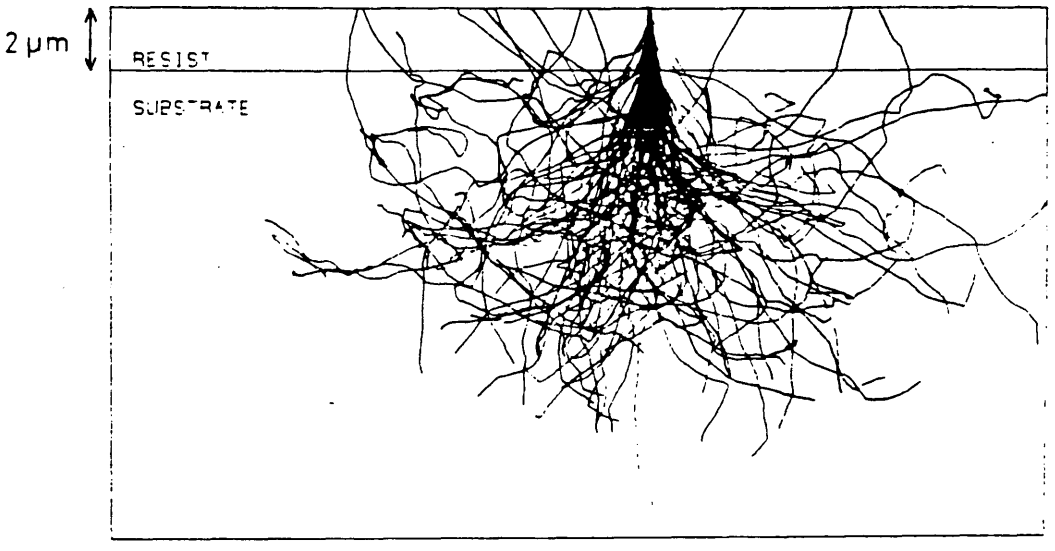

Fig 4.3 Monte Carlo simulation of 100 50keV electrons in PMMA resist and silicon substrate (after Mackie 1984, calculation performed by Dr. S. P. Beaumont).

2μm on a silicon substrate. Each electron will typically suffer several scattering events in the resist and the beam spreads out before most of its energy is deposited in the substrate. Secondary electrons are responsible for the exposure processes in the resist (Hatzakis 1975) with the total exposure being due to the sum of many local exposure events.

The fact that the beam spreads out in the resist due to scattering leads to an undercut profile when the sample is developed as shown in fig 4.4. This is useful in that when the sample is metallised there is less likely to be contact between the metal on the substrate and the excess metal on top of the resist. Clean lift-off is then assured. This aspect will be considered in greater detail in section 4.5.

Another factor affecting the exposure in a resist is the substrate used. Thin substrates are preferred as the contribution to the exposure from backscattered electrons is reduced. In this work the resist (section 4.5.1) and substrates used were thin enough that the resolution is then limited mainly by the actual exposure processes in the resist i.e. secondary electron emission from inelastic scattering points and molecular size effects (Rishton 1984).

4.5 Lithographic Procedure Used In This Work

In this section the details of the lithographic procedure actually carried out in this project are described.

4.5.1 Resist Deposition

Membranes were broken up by scribing into groups of 16, 4 by 4 square arrays, for resist deposition. They had previously been covered with a protective layer of resist in order to keep the surfaces free from dirt and this

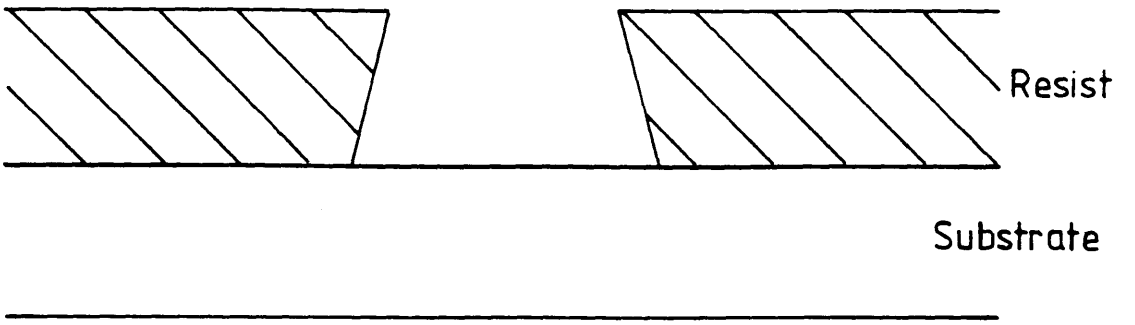

Fig 4.4 Exaggerated profile showing undercutting of single layer resist after exposure and development.

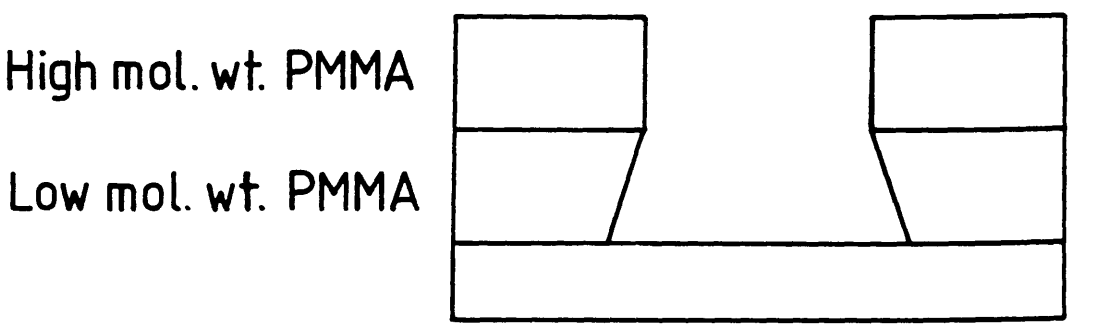

Fig 4.5 Diagram of two layer resist system used to achieve undercut profile.

was removed by placing the samples in a solution of sulphuric peroxide which is a 7:1 mixture of concentrated sulphuric acid and hydrogen peroxide. After 5 minutes with occasional agitation each sample was taken out and rinsed in deionised water before being blown dry. This procedure was performed in a clean cabinet with a fume extractor. The samples were then ready for resist deposition.

Electron resists were discussed in section 4.4 and it was stated that an undercut profile in the developed resist is desirable. This is achieved in a single layer resist when the layer is fairly thick (>0.5μm). Another method which can be used is that of a two layer resist (Mackie and Beaumont 1985). In the case considered here the top layer is a high molecular weight PMMA (mol. wt. 450,000) with the bottom layer a low molecular weight PMMA (mol. wt. 180,000) as used by Mackie (1984). An undercut profile results as the bottom layer is more sensitive to the scattered electrons and less chain scissions are required to break each molecule into sections small enough to be dissolved by the developer. Fig 4.5 shows the resist profile of such a system.

Conventional spinning was the method used to evenly deposit the PMMA onto the samples. In this method samples are usually held onto the spinner chuck by a vacuum seal. This would be enough to break silicon nitride membranes so the samples were stuck to glass coverslips using double sided tape before spinning. Two layers of resist were spun on the sample. The first, a solution of 4% BDH in xylene (low mol. wt. PMMA), was spun to a thickness of 80nm and baked at 180C for one hour. The second layer of 2.5% elvacite in xylene (high mol. wt. PMMA) was then spun on top, again to a thickness of 80nm, and baked overnight. BDH and ELV are the commercial names given to the PMMA of different molecular weight.

Each sample was then broken up into 2mm square chips containing a

single membrane at the centre. A diamond scriber was used to mark out the chips which then broken over glass slides. A few membranes usually broke during this procedure but the overall success rate was high.

4.5.2 Pattern Generation and Exposure

A pattern is exposed in an electron resist using a scanning electron microscope which has been modified for lithographic use, the machine used in this project being a Philips PSEM 500. The scan in this instrument is controlled by a KIM microprocessor which stores information on the pattern to be exposed.

Patterns are created using the interactive pattern editor DESIGN, developed by Mackie (1984), on a GEC 4700 computer. Pattern files store information on coordinate and exposure data. When creating or editing a pattern a square window is drawn on the terminal screen corresponding to the 4096 by 4096 picture frame. A cross-hair cursor which is controlled by a joystick is used to define individual pixel points. Two methods are available for inputting coordinate data for rectangular shapes. The first uses the R and S commands in DESIGN. The R command makes the current cursor position one corner of a rectangle and the S command completes the rectangle at the next position the cursor is moved to. Thus a line of data is stored as two diagonally opposite corners of a rectangle e.g. as 'X1 Y1 X2 Y2'. Alternatively the I command allows the coordinates of diagonally opposite corners of a rectangle to be typed in from the terminal, this is necessary when the exact pixel coordinates are required. Also needed for each rectangle or group of rectangles is a line of exposure data of the form '0 Z 1 0' which means that all rectangles after this line in the file will receive an exposure equivalent to Z (integer) $\mu C.cm^{-2}$ until another line of exposure data is encountered. A line containing '0 0 0 0' signifies the end of the data

file. Many other commands are available to the user using the DESIGN editor but only those required in the present work are described in this section.

There are two possible ways by which a pattern can be exposed in an SEM. In commercial machines the entire picture frame is scanned by the beam with unblanking occurring only at exposure points. The advantages of this system are that the hysteresis effects of the scan coils are not a major problem and that large jumps of the beam position are avoided. The fact that the beam blanker requires data on every pixel point means that the throughput of information is very high. Vector scanning is the other method used to control the scan. As the beam only scans the areas which require exposure the amount of data needed is greatly reduced. This was the process used by the SEM in this work and the difficulties arising from hysteresis and large distance beam stepping were minimised in the following manner.

When inputting a pattern using DESIGN, certain steps were taken to minimise the hysteresis associated with the scan coils and also the effect of the finite settling time of the beam after blanking. These two effects mean that the beam spot does not reach the correct starting point when the scan generator commences stepping after unblanking the beam. The spot approaches its correct position asymptotically with a time constant of about 500μs which can result in skewing of the beam as shown in fig 4.6(a). By ensuring that the beam always jumps upwards to start exposing a rectangle means that the skewing will occur inside the rectangle and will thus be hidden. Also a sacrificial rectangle, drawn inside the first rectangle to be exposed, will avoid any distortion.

The pattern of squares and rectangles (PAT1) chosen in chapter 3 was input using the I commands in DESIGN. Table 4.1 gives the frame and pixel

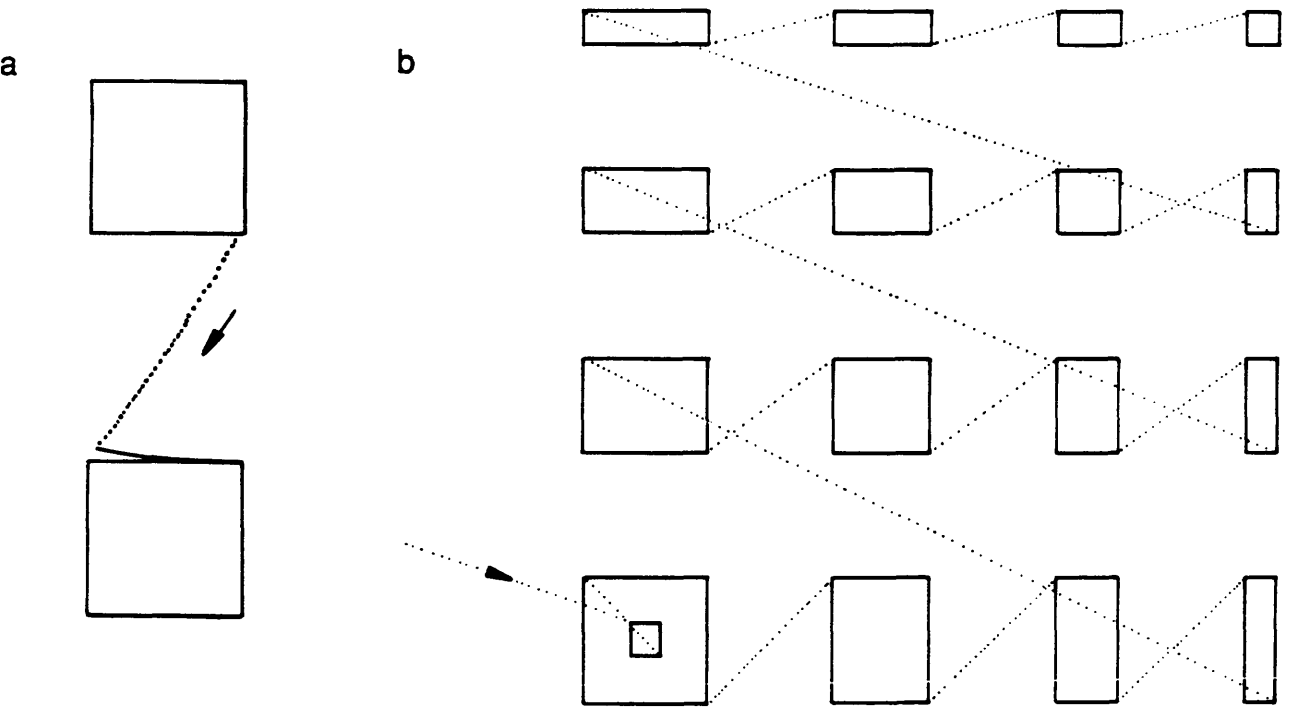

Fig 4.6 (a) Beam skewing due to finite settling time of scan coils.

(b) Example of correct scanning order for PAT1.

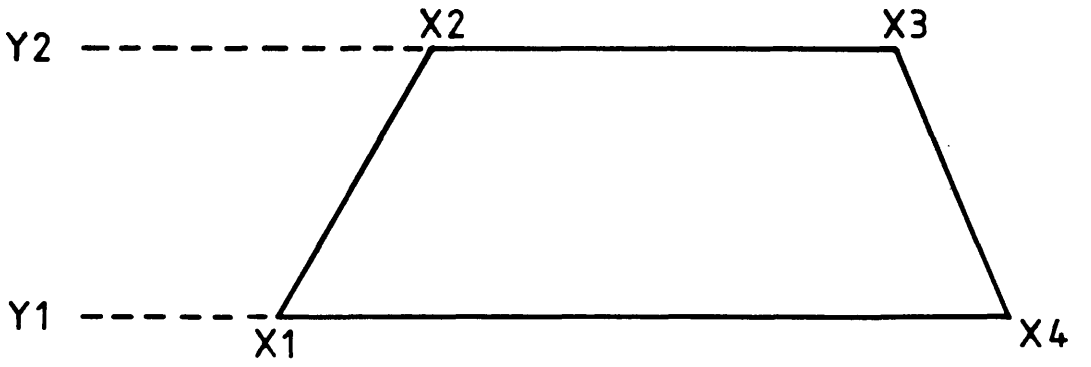

Fig 4.7 Coordinates used for inputting rhombus shapes to DESIGN.

Table 4.1 Some of the pixel and frame sizes available in the SEM.

Magnification	pixel size X	pixel size Y	frame size X	frame size Y
80k	0.38	0.29	1.56	1.19
40k	0.76	0.58	3.11	2.38
20k	1.52	1.15	6.23	4.71
10k	3.05	2.32	12.5	9.5
5k	6.1	4.64	25	19
2.5k	12.2	9.27	50	38
1250	24.4	18.5	100	76

pixel sizes in nm : frame sizes in µm

sizes of the 4096 by 4096 array at some of the magnifications available on the SEM. The size of the pattern was such that a magnification of 2500X provided the dimensions required. The pattern was exposed in the order shown in fig 4.6(b) thus eliminating almost completely any hysteresis effects in the scan coils.

Rhombus (PAT2) and triangular (PAT3) shaped elements can be generated from many small rectangles. A program is available in which a rhombus shape, as in fig 4.7, can be filled up with rectangles with $X1 \leq X2 \leq X3 \leq X4$. Triangles are formed by making say X2 equal to X3 and a diamond shape from two triangles. The greater the number of rectangles used to fill up the space increases the resolution of the shape but the rectangles must be at least two pixels wide. The shapes were drawn such that at 2500X magnification $L_1 = 5\mu m$ in the pattern of five diamonds or triangles with $\Theta = 10$, 20, 30, 40, and 45^{o}. Variation in L_1 was then made possible by changing the magnification.

. Pattern files were then be transferred from the GEC 4070 to the RAM of the KIM microprocessor which controls the scan generator in the SEM. The images were stored on floppy disc for future use.

The operating conditions of the SEM when used for this work were with an 8nm beam spot and an accelerating voltage of 50kV. A special brass holder was available for the samples which allowed transmitted electrons to be collected by the transmission detector. Also a hole in the holder meant that the beam current could be measured with a Faraday cup, this was normally about 20pA so that the dwell time for each pixel was in the range 5-50μs.

As a number of patterns were to be exposed on a single membrane the positioning of the stage was important. The stage can be moved to an accuracy of ±1μm in the X-Y plane by a stepper motor goniometer. When a

sample is placed in the microscope there is normally a misalignment of the goniometer, sample and frame axes as shown in fig 4.8. Goniometer rotation allows the sample and frame axes to be aligned with each other but the goniometer and sample axes are fixed with respect to each other once the sample is inside the SEM. The positions of the patterns are taken from the bottom left corner of the membranes but must be transformed into coordinates relative to the goniometer axes. This problem can be overcome by finding the angle Ω between the sample and goniometer axes. The coordinates of the top and bottom left hand corners of the membrane in goniometer coordinates, say ($\xi 2,\eta 2$) and ($\xi 1,\eta 1$) respectively, can be used to calculate the angle ,

$$\Omega = TAN^{-1}\left[\frac{(\eta 2 - \eta 1)}{(\xi 2 - \xi 1)}\right] \qquad (4.1)$$

Thus the pattern positions in goniometer coordinates (ξ,η) can be worked out from the sample coordinates (X,Y) by the transformation,

$$\xi = \xi_o - X.COS(\Omega) + Y.SIN(\Omega)$$

$$\eta = \eta_o - X.SIN(\Omega) - Y.COS(\Omega) \qquad (4.2)$$

(ξ_o,η_o) is the sample origin in goniometer coordinates. Each exposure position, in the frame coordinates, is stored in a file and the goniometer coordinates are then calculated for each pattern. The whole of this procedure is performed in the EBSS (Electron Beam Scanning System) program.

The process for pattern exposure starts by measuring the beam current,

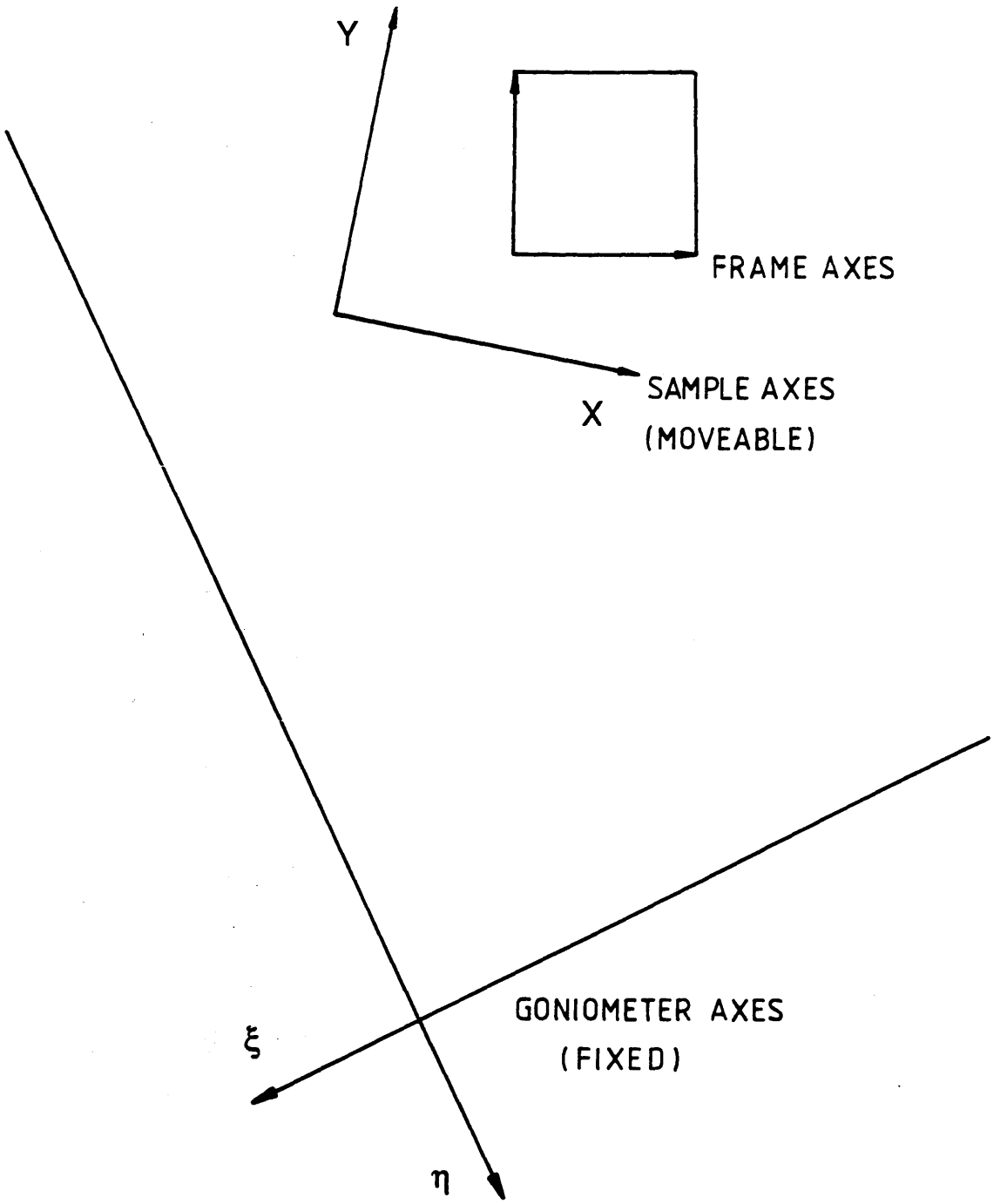

Fig 4.8 Goniometer and sample axis orientation in SEM.

from which the pixel dwell time is calculated from the lines of exposure data. Once the coordinate transformation has been found the stage is moved to each position in turn and patterns are called up and exposed. The sample is then removed from the SEM in order to be developed.

4.5.3 Development of Resist

Exposed samples were developed by immersing them in 32ml of a 3:1 solution of iso-propyl alcohol (IPA) and methyl iso-butyl ketone (MIBK). The solution was at a temperature of 23C with the samples being developed for 30s. Once removed from the solution the samples were rinsed with clean IPA before being blown dry. The mixture of developer used was known to give good results for electron device fabrication (Mackie 1984). Samples were viewed with an optical microscope to ensure that the shapes had developed cleanly.

4.5.4 Permalloy Deposition

Permalloy was deposited onto the developed substrates by means of resistive heating in a vacuum chamber at a pressure of 10^{-5}Torr. A dual evaporator was used so that a layer of chromium, of thickness approximately 10nm, could be deposited onto the substrate first. This helped the adhesion of the particles to the substrate as compared to those evaporated without this layer. The metal was heated in a tungsten-alumina boat and the samples were held in place on a microscope slide by double sided tape. Each sample was oriented perpendicular to the direction of the evaporated beam so that the possibility of contact between metal on the resist and substrate was reduced. Samples were also placed far enough from the boats to prevent heat generated which could cause the PMMA to melt and result in

poor lift-off. This also ensured that the there was no appreciable film thickness gradient at the sample.

A quartz crystal was used to monitor the thickness of the deposited film. It had previously been calibrated for changes in crystal resonant frequency as a function of evaporated film thickness with the thickness being measured on a Varian Å-scope interferometer. A slow rate of evaporation, not greater than $0.3nm.s^{-1}$, was used in order to reduce the stress on the metal as it had been noted to peel off when high rates of deposition were used.

4.5.5 Lift-off

Two methods can be used to lift-off the excess metal from the sample. The first is that of 'shooting' (Beaumont et al 1981). In this case the sample is held with a pair of tweezers in a beaker of methanol in which PMMA is insoluble. Chlorobenzene, a solvent for PMMA, is then fired through a hypodermic syringe onto the surface of the sample. Sufficient agitation is provided by this procedure that the excess metal lifts off very cleanly. The samples were rinsed in clean methanol before being blown dry. In the present case some of the particles were also found to be removed when this procedure was performed.

The other method involves placing the sample in acetone, a solvent for PMMA. It is then observed in a low power optical microscope where the excess metal is seen to slowly float off the sample. Once removed the sample is rinsed in acetone and blown dry. A higher power optical microscope was then used to check that the lift-off had been successful. This second method was used as it was considered easier to implement for the samples used here.

Before a specimen could be examined in TEM or STEM it had to be

covered with a conducting layer of carbon to prevent the Si_3N_4 from charging in the microscope. Charging not only can cause the image to jump a great deal but can result in breaking of the membrane soon after insertion into the microscope. Each specimen was coated with a layer of approximately 20nm of carbon prior to examination in TEM.

CHAPTER 5

CTEM OBSERVATIONS OF PAT1 PARTICLES

5.1 Introduction

In this chapter observations of the square and rectangular particles of PAT1 using the Fresnel mode of Lorentz microscopy are described. A JEOL 1200-EX electron microscope was used for all observations in this mode and the imaging conditions are described in section 5.2.

Samples were produced at different thicknesses in the range 20-60nm. The thickness of the particles was a major factor in this study as it determined the nature of the domain walls in the film as was discussed in section 3.2. Also, as the energy of the walls changes with specimen thickness their effect on the domain structure was noted. As the shape of each particle was critical in defining its domain structure a classification of the structures was introduced to allow the results to be presented more clearly. The scheme of classification is outlined in section 5.3.

The physical microstructure of the particles was important as domain structures can be affected by the presence of defects. Section 5.4 details a study of the particles in the normal mode of operation of the microscope. Initial observations of the samples in their as deposited state was made using the Fresnel mode described in section 5.5. As no in-situ magnetising stage was available during the course of this work the particles could only be observed in a remanent state and the domain structures obtained following the application of various external fields is reported in section 5.6. Magnetic anisotropy was induced in the samples by evaporating the permalloy onto the Si_3N_4 membranes in the presence of a magnetic field

and the effect of this on the domain structure supported by the particles is described in section 5.7.

5.2 Microscope Imaging Conditions

In chapter 2 the various modes of Lorentz microscopy in the CTEM were discussed. The predominant limitation of these modes are that they must be performed with the objective lens of the microscope switched off and so the maximum magnification achievable in most instruments is fairly low. For example the highest standard setting in LOW MAG mode on the JEOL 100C is only 750X which would make examination of the PAT1 particles limited to those with both in-plane dimensions greater than about 1μm.

The standard LOW MAG settings on the JEOL 1200-EX extend up to 1000X which is still modest considering the smallest in-plane dimensions of the particles in question was 0.25μm. A useful feature of this microscope is that it has a free lens controller (FLC); this allows the lens currents to be altered manually to suit the user's operating conditions. In LOW MAG mode focussing the image is controlled by the objective mini lens and there are three intermediate (I) lenses and a projector lens below this. By increasing the lens current in I2 to maximum strength and reducing I1 and I3 to zero strength a magnification of 5000X is obtained (McFadyen 1986). This meant that even the smallest particles in PAT1 could be imaged in the Fresnel mode although the contrast associated with the edges of the particle due to the defocus prevented details of any domain structure being revealed although it was generally possible to determine whether or not the particle supported more than one domain.

Illumination of the specimen is controlled by two condenser lenses and for Fresnel imaging a plane wave electron illumination is desirable (section

2.2.1). This was achieved by exciting both condenser lenses strongly so that the effective source was small and distant from the specimen plane. These conditions resulted in low current densities in the image plane so that exposure times of over 60 seconds per image were needed if ordinary Kodak 4489 film was used. X-ray film being much faster was found to be more suitable. The type of film used in this project was CEA Reflex-15 which required an exposure time of less than 5 seconds under the same imaging conditions.

A video system was recently acquired for use with the 1200-EX. This comprised a camera with an RCA silicon intensifier target tube (SIT) viewing a single crystal YAG screen which was located underneath the camera chamber. Images are acquired using an Arlunya image processor TF 6000 along with an Agar camera control display unit T1570. Noise reduction and image enhancement, either statically or dynamically, can be performed to improve image quality and the images can be stored on video tape. This allows a quick and efficient means of storing data on any interesting features observed.

5.3 Domain and Shape Classification

The square and rectangular particles of PAT1 can be classified in terms of shape, size and domain structure. Domain structures were divided into two main categories; category I structures were those in which flux closure was essentially complete within the particle whereas category II particles displayed incomplete flux closure within the particles. Further subdivision of the categories was required to give a complete description of the results observed in these samples. Different sub-divisions were required for the different thicknesses of samples but the following classification is made to

allow a clearer review of the results to be given. Firstly, the dimensions of the particles are denoted by L1, L2 and L3, as in fig.5.1, where L1 is the larger in-plane dimension and L3 is the particle thickness.

Fig 5.2 shows a variety of possible simple flux closure structures for particles with different values of L1 and L2. Category Ia structures are defined as those with the domain configurations like fig 5.2(a). It is noted that this structure reflects the fact that the ratio of L1 to L2 is integral so that domains can be separated entirely by 90^{o} walls. Fig 5.2(b) is an example of category Ib structure where the basic domain structure is the same as category Ia but the aspect ratio is not integral and a 180^{o} domain wall is introduced to accommodate the structure formed by the straight 90^{o} walls. An example of a category Ic structure is shown in fig 5.2(c) and here the aspect ratio of the particles can take any value greater than 2. Finally fig 5.2(d) defines the structure of category Id domain geometry.

The category I domain structures drawn in fig 5.2 imply that more than one structure may be possible for a particle with a given aspect ratio. Domain wall energies are important in determining which structure will be favoured for a certain particle. Also as the domain wall energy is a function of specimen thickness it is clear that the size and shape of the particles are major factors in the type of domain formation observed.

Sub-division of the category II particles was also needed. As the structures were quite dissimilar at different thicknesses of sample they shall be discussed along with actual observed structures later on in this chapter.

5.4 Physical Microstructure Of The Deposited Film

Specimens were observed in CTEM in the normal mode of operation with the objective lens on in order to check the edge acuity and crystalline structure of the particles. An in-focus image covering a large area of a 60nm

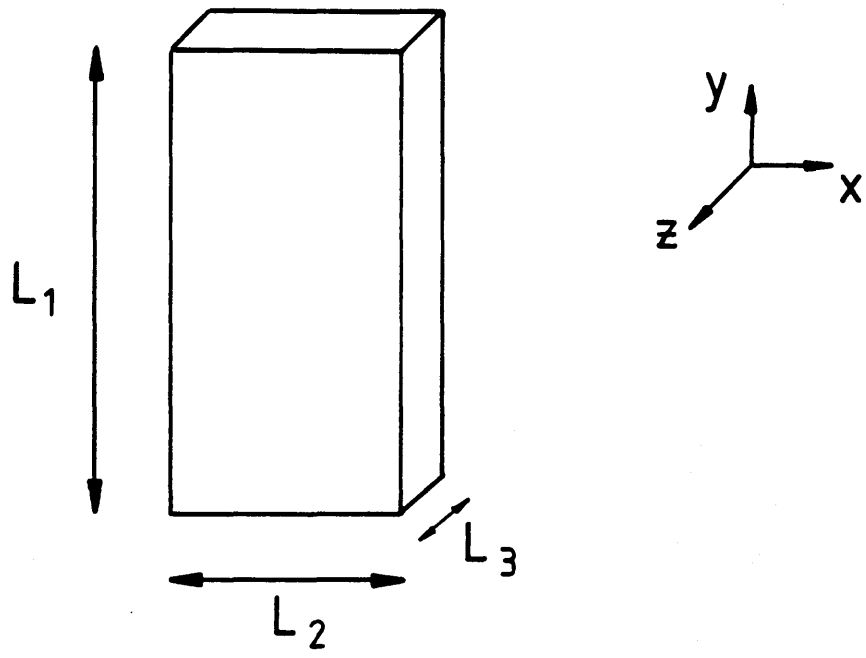

Fig 5.1 Definition of particle dimensions. L_1 is larger in-plane dimension and L_3 the thickness.

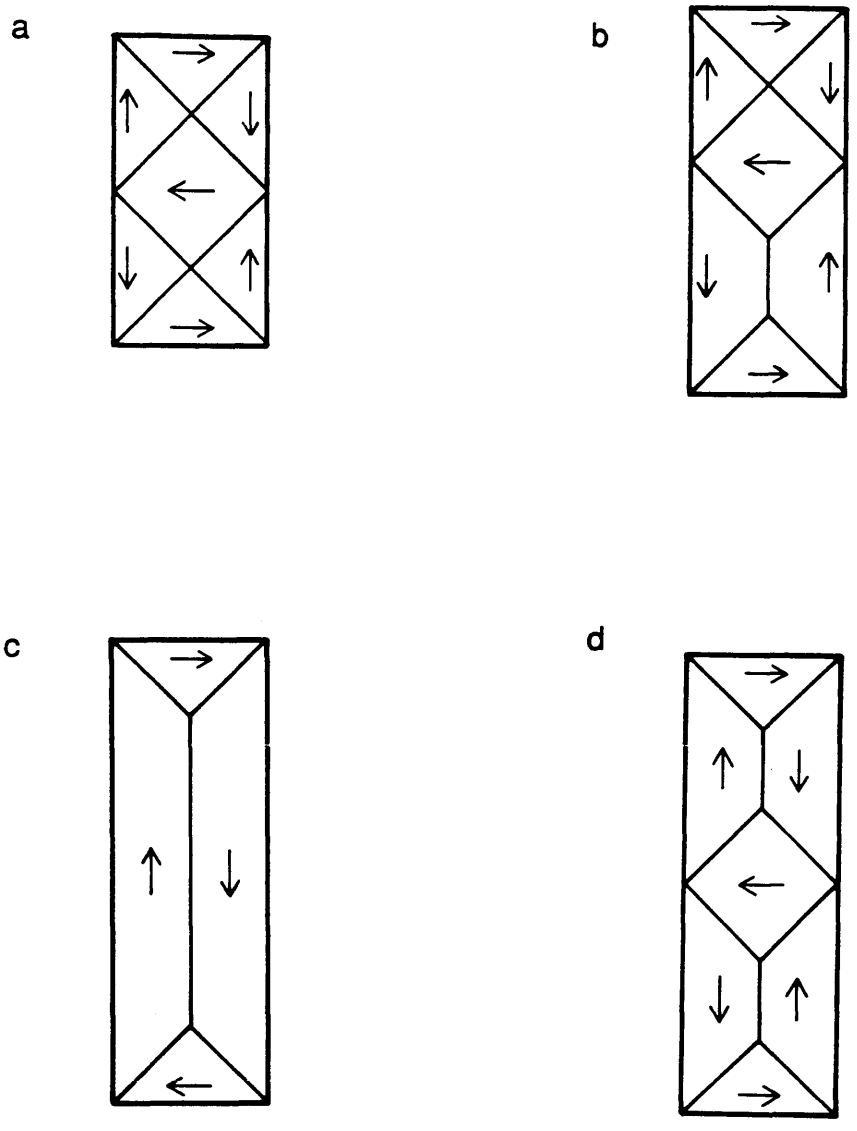

Fig 5.2 Examples of domain structure classification, (a) Ia, (b) Ib, (c) Ic and (d) Id.

thick PAT1 sample is shown in fig 5.3. Clearly the shapes of the particles are very regular and this is confirmed in fig 5.4 which was taken at a higher magnification. This image reveals the micropolycrystalline nature of the sample and also the edge sharpness achieved by the electron beam lithography fabrication process. The magnitude of the edge definition was measured as the spatial extent of the variations along the edge and was of the order of <10nm. An estimate of the grain size of the sample was made from fig 5.4 and appeared to be in the range 5-10nm. This was to be expected in a thin metal film evaporated at normal incidence and with the substrate at room temperature (Chopra 1969). The diffraction pattern taken from an area such as that in fig 5.4 is shown in fig 5.5. There is little intensity variation in each ring in the pattern indicating that the crystallites were essentially randomly oriented. From the spacing of the rings the crystalline structure and lattice constant of the material was deduced (Edington 1973). In this case the structure was found to be face centered cubic (FCC) with a lattice constant of 0.37nm.

5.5 Fresnel Observations of PAT1

Magnetic contrast generated by the Fresnel mode of Lorentz microscopy allowed the magnetisation distribution within simple domain structures to be easily deduced. Those particles possessing complicated structures in which flux closure appeared to be incomplete were more difficult to analyse. This was due to the fact that stray fields were not revealed by this mode and the magnetisation direction within domains was not always obvious. Confirmation of the results given in this chapter are described in chapter 6 from investigations using the DPC mode. The initial study in the 1200-EX allowed a quick identification of the domain geometries possessed by the

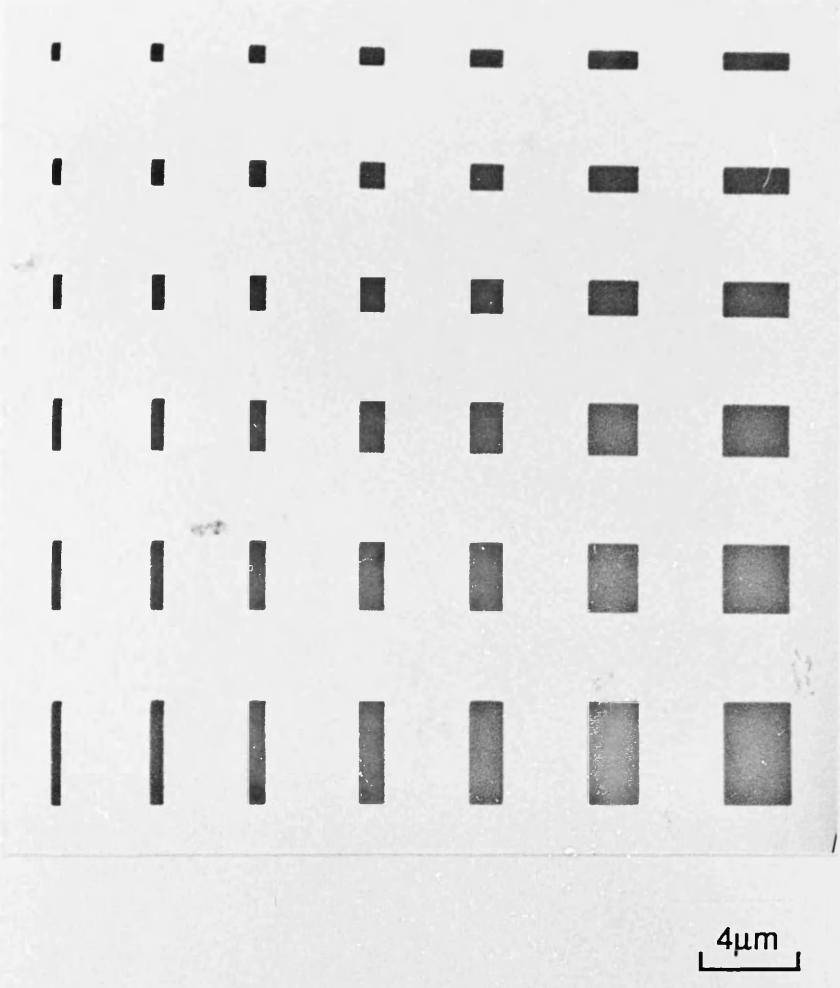

Fig 5.3 In-focus image of area of PAT1 sample of thickness 60nm.

Fig 5.4 High magnification image of corner of a PAT1 particle of thickness 60nm showing micropolycrystalline structure and high edge acuity available using e-beam lithography.

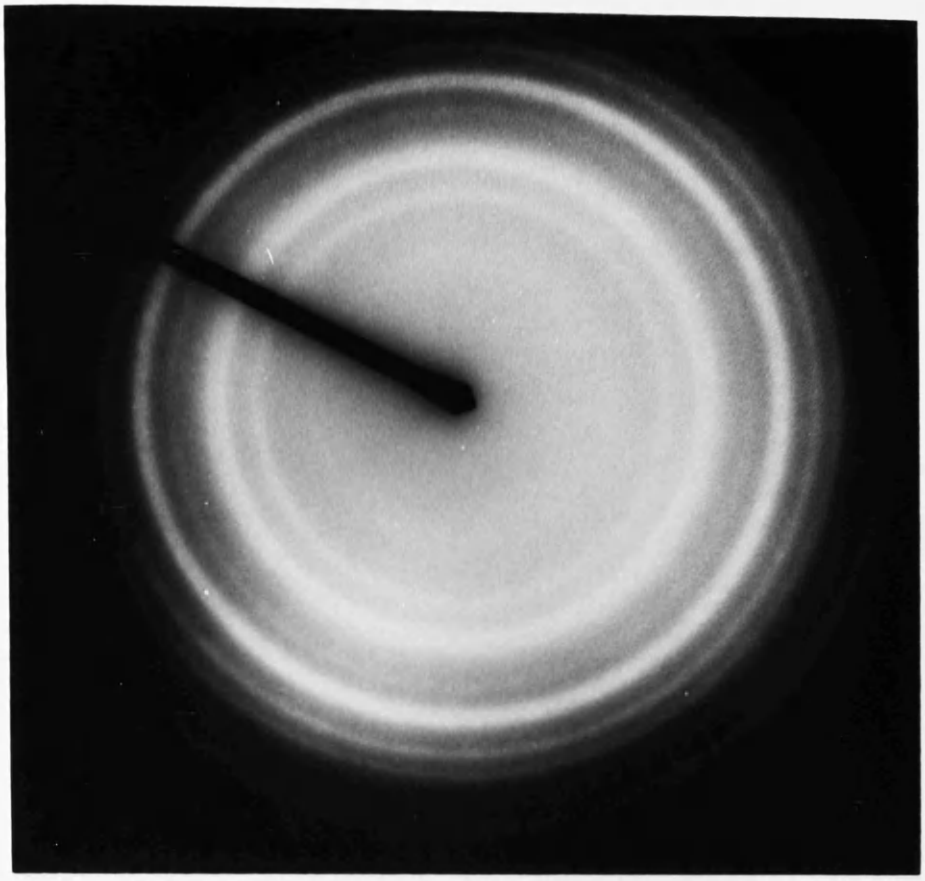

Fig 5.5 Diffraction pattern from selected area of fig 5.4 from which crystalline structure was determined to be face centered cubic.

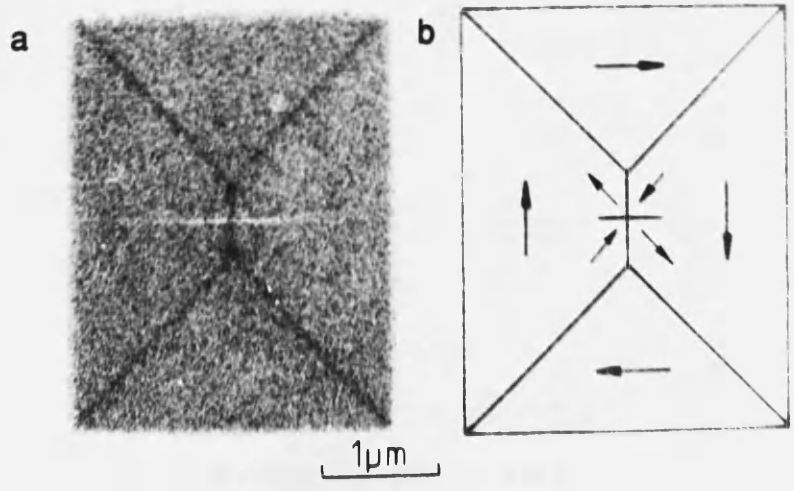

Fig 5.6 (a) Fresnel image of a 4 by 3 μm particle from 70nm thick sample. The schematic magnetisation distribution deduced from this image is shown in (b).

particles and as time on the VG HB5 was limited this preliminary study was essential.

5.5.1 60nm Thick Sample

In sections 1.3 and 3.1 the magnetisation distribution within soft magnetic thin film elements of low anisotropy was discussed. The most notable aspect of many previous experimental results, which forms a basis of the recent theoretical treatment (Van den Berg 1984), is that solenoidal configurations occur in the elements at zero applied external field provided the planar dimensions of the element exceeds $(A/K_d)^{-0.5}$ (where $K_d=\mu_o M_s^2/2$). This gives a value of about 5nm for the critical dimension for permalloy with magnetisation constants $A=10^{-11}J.m^{-1}$ and $M_s=8x10^5A.m^{-1}$). This condition was satisfied for all of the particles reported here.

Domain walls show up as bright and dark lines as in fig 5.6(a) This is a typical example of the type of image obtained using the Fresnel mode. The magnetisation distribution deduced from this micrograph is drawn in fig 5.6(b). Further structures frequently observed in samples of this kind are shown in figs 5.7 and 5.8. These images illustrate the dependence of domain structure on the shape of the particle. Classification of the domain configurations into those which displayed a flux closure formation (category I) and those with a domain geometry suggesting incomplete flux closure within the particle (category II) shall now be discussed in detail.

Division between the two categories occurred at an aspect ratio of n=L1/L2 having a value of about 4 such that those particles with $n\leq4$ possessed category I structures. This is evident from figs 5.7 and 5.8. Category Ia structures were seen to be present in particles with an integral value of n as is shown by examples in figs 5.7(b), (c) and (f) and figs 5.8(a)-

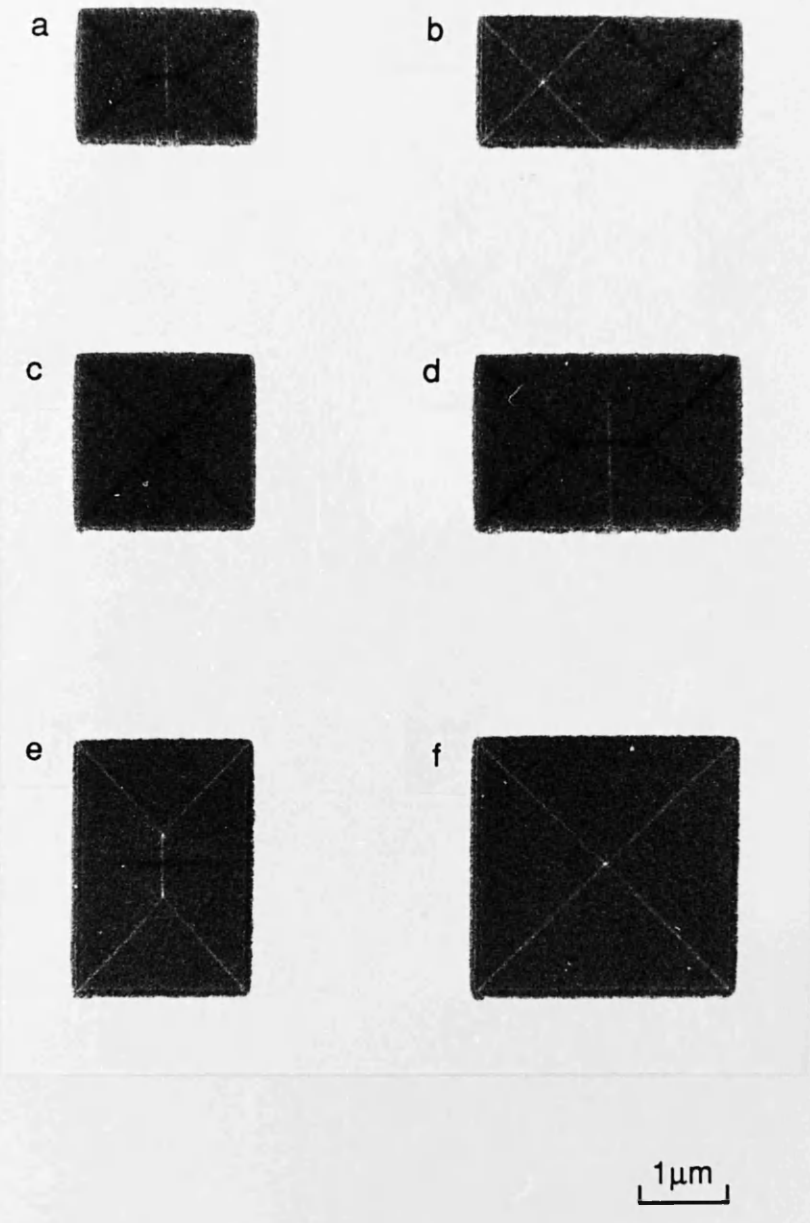

Fig 5.7 Typical Fresnel image obtained from 60nm thick sample.

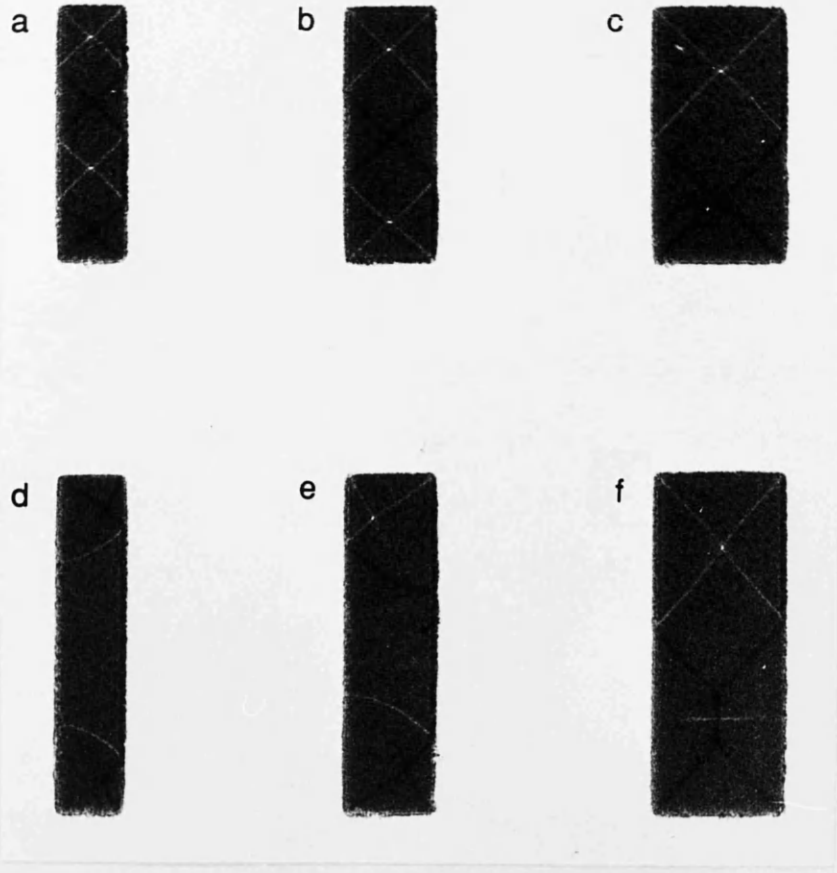

Fig 5.8 As fig 5.7.

(c). These structures, as defined in fig 5.2, consisted of domains separated entirely by straight 90° walls. Even the smallest particles in this sample appeared to have this solenoidal magnetisation distribution although with the edge wave introduced by the Fresnel mode this was hard to determine conclusively.

The category Ib structure of fig 5.2(b) were also present in this sample. Figs 5.7(a), (d) and (e) and fig 5.8(f) demonstrate that this structure occurred for particles with non-integral values of n. Essentially the magnetisation configuration was the same as the category Ia structure, with the magnetisation parallel to the edges of the particle and the domains separated by straight walls. The difference in this case was that although the straight 90° walls were still present, sections of 180° wall were introduced to compensate for the non-integral aspect ratio of the particle. Also of importance was the appearance of cross-ties in the 180° wall sections which is to be expected in permalloy films of thickness 60nm.

The solenoidal magnetisation distributions observed in particles with category I structures were restricted almost exclusively to the Ia and Ib type in samples of 60nm thickness. In particular 180° walls appeared to be fairly uncommon and of minimal length when present. This indicates that 90° walls were energetically more favourable than cross-tie walls at this thickness in these particles. A fuller analysis of this point is presented in section 8.1

In section 5.3 category II domain structures were defined as those in which a closed flux path does not exist within the particle itself. Particles possessing these structures were those with $n \geq 4$ and two examples are shown in figs 5.8(d) and (e). It was evident that the domain structures present in these particles were not as simple as the category I geometries and the magnetic contrast could be interpreted as giving rise to incomplete flux closure within the particle. The curved walls were in marked contrast to

the walls in the category I structures. Similar domain configurations have been observed in previous studies of rectangular permalloy bars with in-plane dimensions of the order of tens of microns (Huijer and Watson 1979, Van den Berg 1984). It must be noted that in the studies referenced such structures were present in bars which were being subjected to an external field and the domain configurations of the unmagnetised bars were of the Ic and Id type. The particles in the sample under investigation here, however, had not been subjected to any fields. As in the previous studies two different types of structure were observed as shown in fig 5.8 (d) and (e). Category IIa structures were defined as those in which the rotation of magnetisation at both ends of the particle was in the same sense i.e. like the structure present in fig 5.8(d). By comparison in the IIb structure the magnetisation rotation at the ends was in an opposite sense as in fig 5.8(e). Schematic representations of the two distributions, interpreted from these images, are given in fig 5.9. The two structures appeared in this sample with about equal frequency with no apparent association between the structure and the aspect ratio of the particle. In the case of the previous studies referenced the structure depended on the demagnetised state of the permalloy bar (either Ic or Id type).

The main conclusion to be drawn from the category II structures was that the particles appeared uniformly magnetised at their centre with a large amount of magnetisation rotation occurring at the ends. This can be thought of as a shape anisotropy. Magnetisation rotation at the ends of the particle occurs to reduce the magnetostatic energy of the particle compared with that of a uniformly magnetised particle. More information on these structures was extracted using the DPC mode of Lorentz microscopy and this is described in section 6.3.

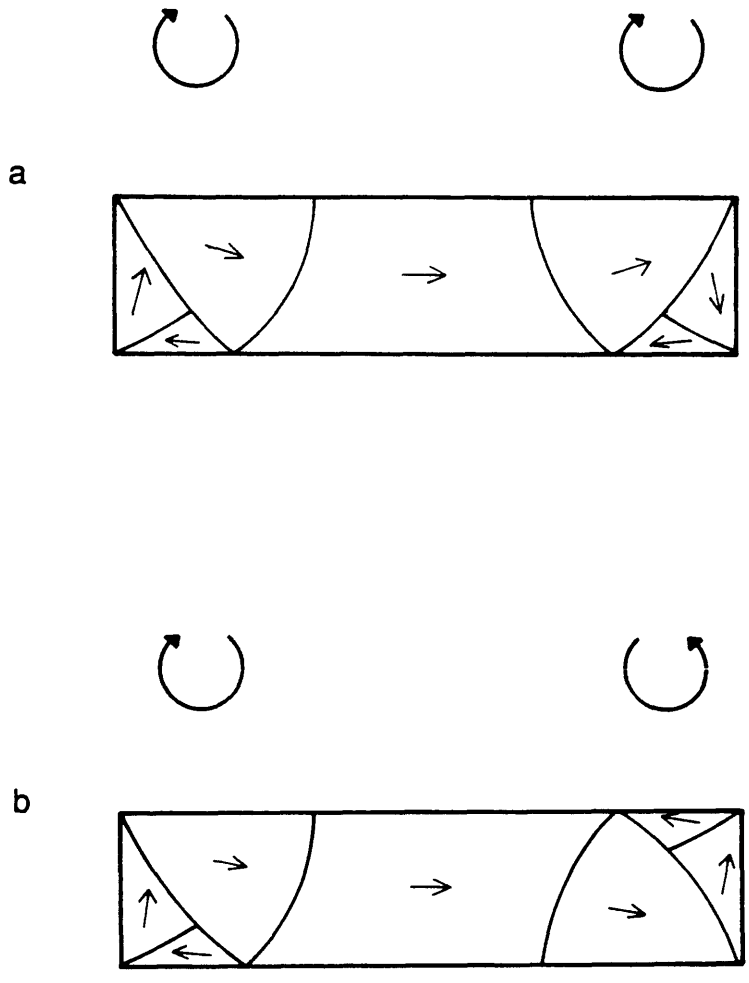

Fig 5.9 Schematic drawing of possible domain structure of particle with (a) a category IIa and (b) category IIb structure.

5.5.2. 20nm Thick Sample

The classification of particle domain structure at this sample thickness was similar to that in the 60nm thick sample although very significant differences between particles with similar in-plane dimensions were observed in the two cases. The two major categories still existed but the division between them was not as distinct. The transition from category I to II again occurred around n=4.

Category I structures observed in this sample bore a resemblance to those seen in the 60nm thick sample. Typical examples are shown in figs 5.10 and 5.11. From these images it is evident that the domain walls, unlike those in the 60nm thick sample, were not very straight. Wall curving, seen in figs 5.10 and 5.11, occurred in the 90^{o} walls although the 180^{o} walls were quite straight. Furthermore, no cross-ties were present in these 180^{o} wall sections which was to be expected from the wall models discussed in section 3.2 (Kosinski 1977).

Classification of the category I structures was not as simple as in the 60nm thick sample. Examples of the category Ia structures defined in section 5.3 appear to be present in figs 5.10(a), (c) and (f) although only the particle in (a) had an aspect ratio of n=2. In the other cases the walls curved to accommodate this type of structure rather than adopt the category Ib structure seen in particles of the same dimensions in the 60nm thick sample. Thus although such particles appeared to possess a flux closure structure there will be magnetostatic energy associated with magnetisation variation along such walls in addition to that normally possessed by these walls.

Just as the category Ia structure was possible in particles with non-integral values of n it should also be noted that the Ia structure was not always observed in particles with integral n ($n \leq 4$). Fig 5.10(d) is that of an

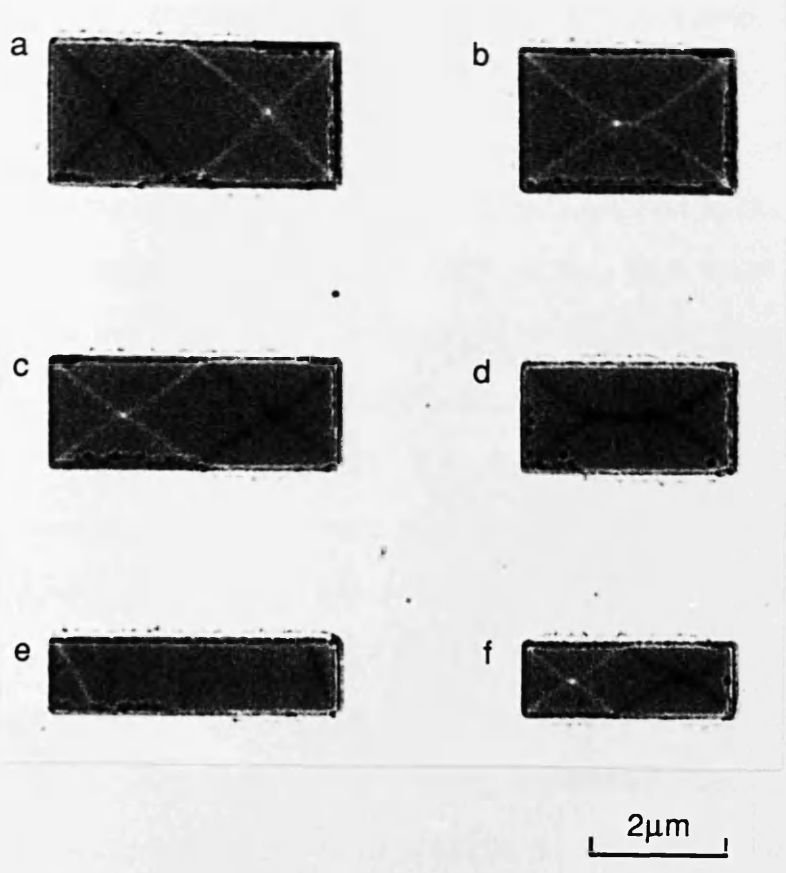

Fig 5.10 Typical Fresnel image from a 20nm thick sample.

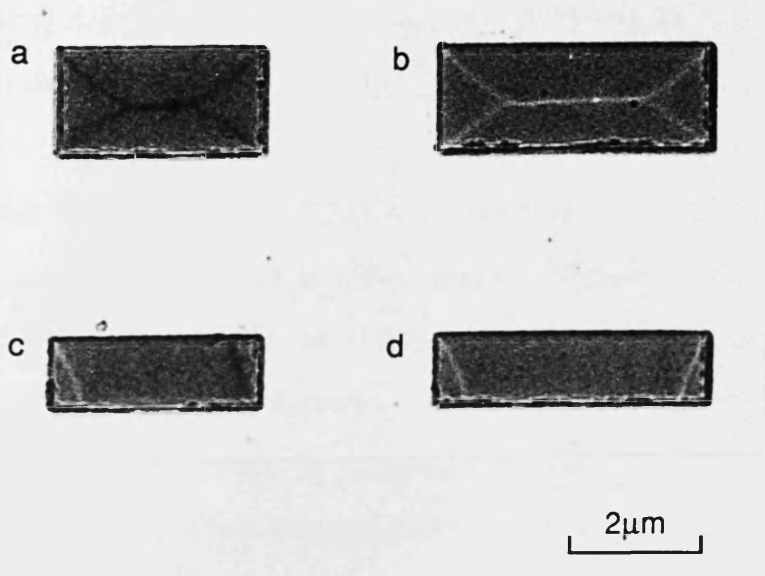

Fig 5.11 As fig 5.10.

n=2 particle which accommodated a Ic domain configuration. This structure was also present in figs 5.11(a) and (b). Essentially the same structure was present in fig 5.10(b) although this was truly a Ib structure (as n<2). All of these Ib and Ic structures contained 4 domains parallel to the edges of the particles separated by 90^{o} and 180^{o} walls. The 180^{o} walls were presumably of the Neel type with a single Bloch line appearing at some point along the wall where the polarity of the Neel wall changed sign as shown schematically in fig 5.12. The non-uniqueness of the domain structures associated with particles of a specific shape was evident in this sample, and contrasts strongly with the results from the 60nm thick sample.

Particles with larger aspect ratios (n≥4) again displayed contrast suggesting that the magnetisation distribution was not solenoidal. These category II' structures are shown in fig 5.10(e) and 5.11(c) and (d). It was obvious that the structures in these particles were much simpler than those found in the 60nm thick sample and two different configurations were again possible. From these images schematic representations of the two sub-structures were deduced and are are given in fig 5.13(a) and (b). We define them as the IIa' and IIb' structures at this thickness. Confirmation of these interpretations are given later in section 6.2 from the DPC study of these samples. It was also noted that occasionally category II' structures appeared in particles with n<4 and although this was fairly uncommon it had not been observed in the 60nm thick sample at all. Both the IIa' and IIb' configurations appeared in about equal numbers suggesting that the energy of the two distributions was about the same. These structures were very close to being single domain in that the particle appeared to be uniformly magnetised along its longitudinal axis for most of its length. Considerable rotation of the magnetisation occurred at the ends in order to reduce the area over which the free poles were distributed and hence cut

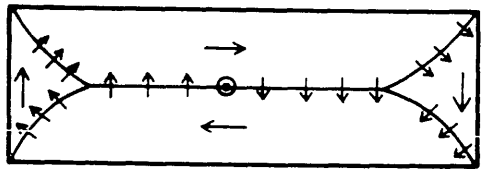

Fig 5.12 Schematic magnetisation distribution in a 20nm thick particle containing a section of 180^{o} wall.

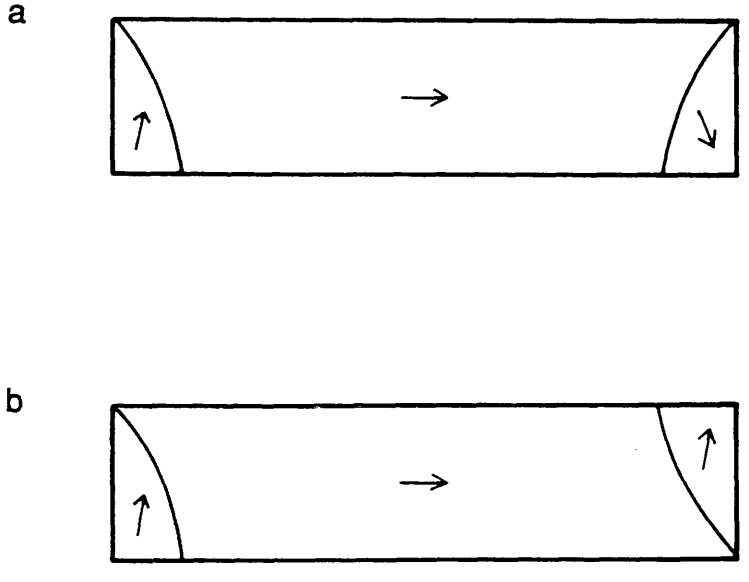

Fig 5.13 Possible representations of (a) IIa' and (b) IIb' structures in 20nm thick particles.

down the magnetostatic energy associated with the structure. Presumably this configuration represents a balance between wall energy and magnetostatic energy, both of which vary with thickness, and therefore account for the simplicity of the structure at this thickness. The DPC mode is ideal for investigating the detailed magnetic structure in these particles and is described in section 6.3.

5.5.3 Samples of Intermediate Thickness (25 and 40nm)

In addition to the samples discussed in the previous sections specimens of thickness 25 and 40nm were also produced. These two samples displayed very similar domain characteristics. As with the thicker and thinner samples the domain structure in the particles allowed a classification into those particles possessing complete flux closure (category I) and those in which flux closure is incomplete (category II). The aspect ratio at which the transition between the two categories occurred was again noted to be n=4.

Typical category I structures are shown in fig 5.14 for a sample of thickness 25nm, and in fig 5.15 for a sample of thickness 40nm. The category Ia domain structures such as those shown schematically in fig 5.2 were not particularly common occurring usually in some n=1 and 2 particles and infrequently in those with n=3. Wall curving also meant that the Ia structures were also observed in some particles with non-integral n as was exhibited by 20nm thick particles (section 5.5.2). This is shown in fig 5.15 (b). Equally possible for other category I particles were Ib, Ic and Id structures as shown in the figures. Also the position of the middle domain in the Id structures seemingly occurred at a fairly random position along the particle as displayed in figs 5.14(c) and (d). One particular point of note was these samples contained cross-tie walls indicating that the transition for 180^{o} walls from Neel to cross-tie takes place at a film thickness between 20 and 25nm

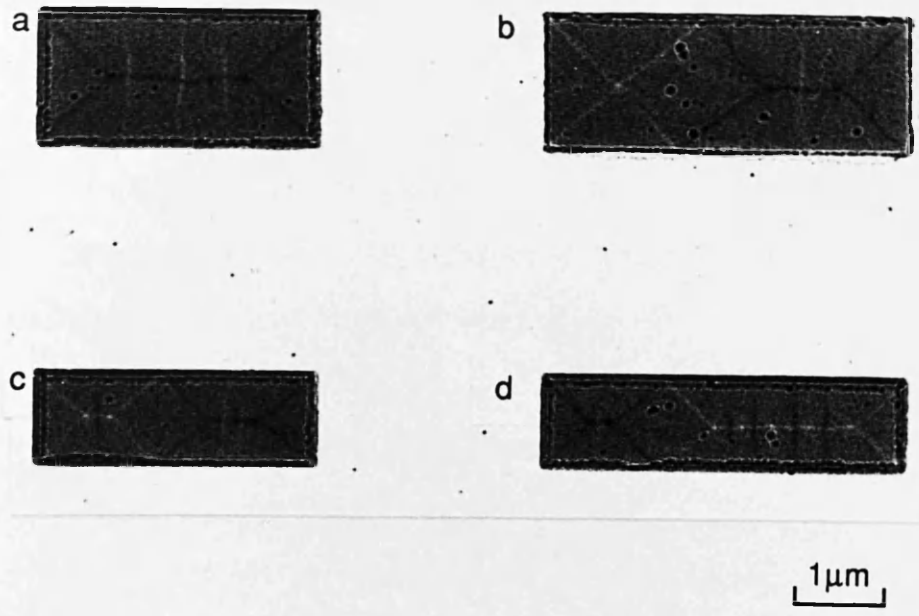

Fig 5.14 Typical Fresnel image of a 25nm thick sample

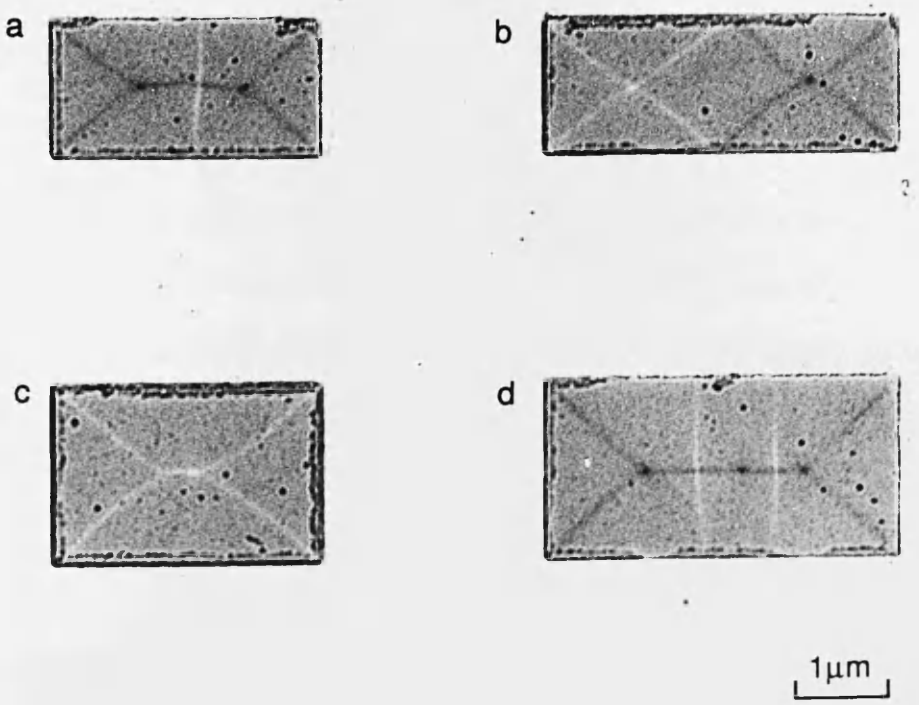

Fig 5.15 Typical Fresnel image of a 40nm thick sample.

for a magnetic material with the characteristics of permalloy. This is in excellent agreement with the theoretical models of Kosinski (1977) and Feldtkeller and Fuchs (1964), even though these models were based on films of infinite extent in the film plane. In comparison to the 60nm and 20nm thick samples the particles with category I structures in the samples of intermediate thickness seemed to bear more similarities to the thinner samples with regard to non-uniqueness of structures but the observation of cross-ties meant that similarities with the thicker sample were also present.

The category II domain structures present in these samples were identical to those seen in the 60nm thick sample. The two structures of fig 5.9 were both observed in these samples with approximate equal frequency.

5.5.4 Summary of PAT1 Domain Structures

In order to clarify the domain structures associated with particles of certain aspect ratios and thicknesses the results described in the previous three sections have been tabulated for quick reference. Table 5.1 gives a summary of the domain structures of particles in PAT1 at the three thicknesses considered. The results show some interesting features in that the domain structure associated with a certain aspect ratio of particle was not uniquely determined although the 60nm thick particles with category I structures were an exception to this. The implications of these results to the study of domain wall energies in thin films is discussed in greater detail in section 8.1.

5.6 Application of External Fields

In-situ experiments involving the application of controllable magnetic

Table 5.1 Summary of the domain structures observed in the as-grown state for the various thickness of particles in PAT1, n is the aspect ratio of the particle.

n	60nm	20nm	25 and 40nm
1	Ia	Ia	Ia
1.33	Ib	Ib	Ib
1.5	Ib	Ib	Ib
2	Ia	Ia Ic	Ia Ic
2.66	Ib	Ia Ic	Ia Ic
3	Ia	Ia Ic II	Ia Ic Id II
4	Ia II	Ia Ic II	Ia Ic Id II
>4	II	II	II

fields was not possible as no magnetising stage had been built for the 1200-EX. Thus to observe any effects of magnetic fields the samples were subjected to large fields and subsequently examined in the microscope in their remanent state. This allows the domain structures formed from possibly saturated particles in the presence of a collapsing field to be investigated. Three orthogonal fields were applied to the specimens and the magnetic structure of the particles were viewed after application of each field. Results are presented from the 20 and 60nm thick samples with emphasis on the category I structures.

5.6.1 Out of Plane Fields

Particles were subjected to a field perpendicular to the plane of the sample when they were still in the microscope by switching on the objective lens current to maximum strength and then switching it off. This produced a field of ~$6x10^5 A.m^{-1}$ orthogonal to the specimen plane. Such a field was regarded as an (out of plane) hard axis field because of the large magnetostatic energy associated with the free poles on the top and bottom surfaces of the film as shown in fig 5.16 when the magnetisation lies perpendicular to the plane of the particle.

Following application of this hard axis field, examination of the particles by the Fresnel mode revealed that in many cases the domain structures of the particles had become complicated and irregular. This was true for both the 20 and 60nm thick samples. An example of the typical effect of this field is shown in fig 5.17 for a 60nm thick sample. Whilst particles which previously showed flux closure still do so the irregularity is such that no attempt at a detailed classification of the category I particles was undertaken. Category II domain structures of the type seen in the

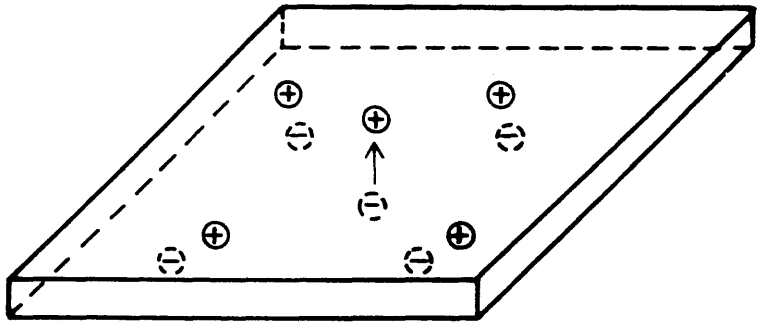

Fig 5.16 Particle magnetised by out of plane field.

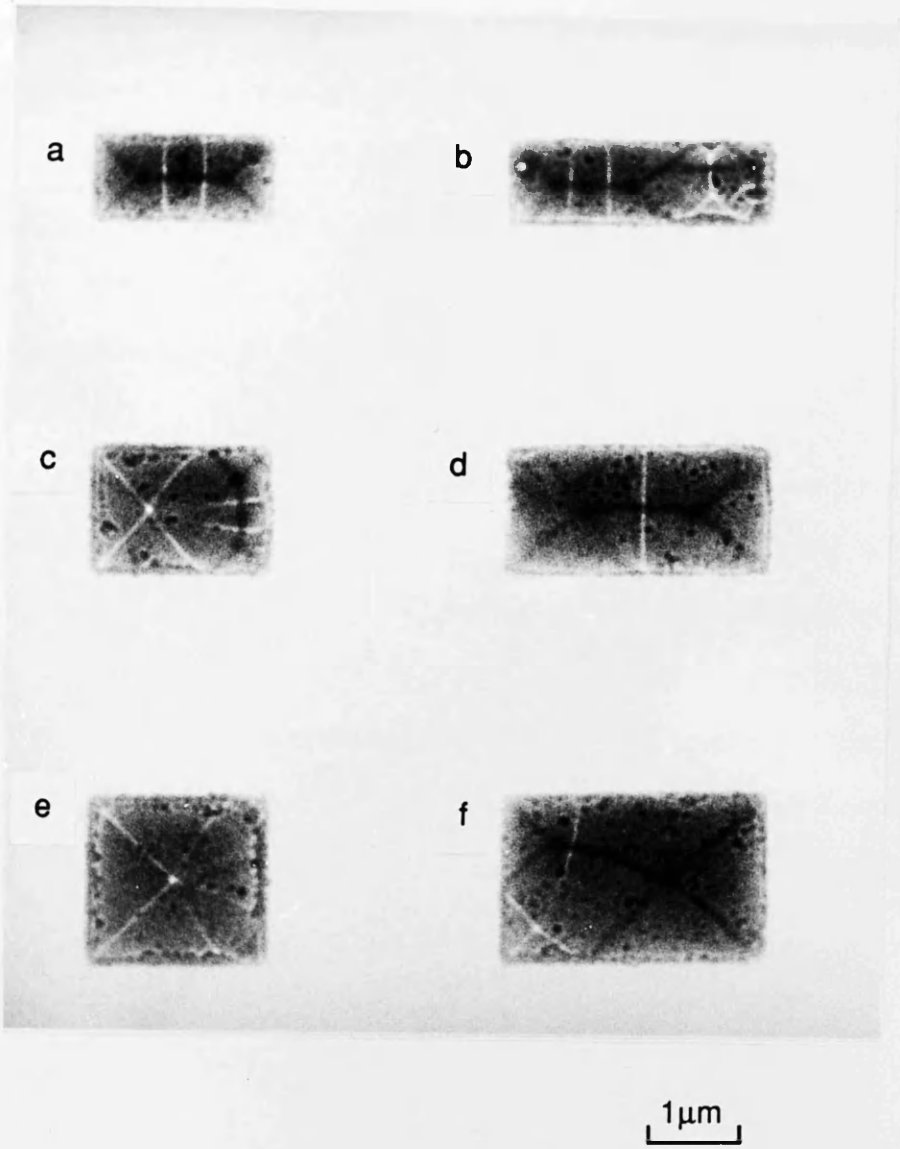

Fig 5.17 Remanent state of 60nm thick particles after being magnetised with a field perpendicular to the plane of the sample.

unmagnetised state were again present in particles with n≥4. Also both the IIa and IIb structures were observed in about equal numbers.

One possible explanation for the occurrence of the irregular domain structures after the application of the out of plane field may have been that the particles did not saturate in this direction in the external field. The value of the objective lens field $6x10^5 A.m^{-1}$ compares with the equivalent magnetisation $8x10^5 A.m^{-1}$.

5.6.2 Application of In-plane Fields

The in-plane fields were applied to the specimens after they had been subjected to the out of plane field. A large electromagnet was used to provide a field of $12x10^5 A.m^{-1}$ at the specimen plane. Fields were directed along either the X or Y axis of PAT1 as defined in section 3.3. Domain structures were observed immediately after each field was applied. Due to the symmetric nature of PAT1 about the line Y=X only one field need have been applied; the second field allowed a check on the results obtained from the first.

5.6.2.1 60nm Thick Sample

These experiments provided some very interesting results. Domain classification was again made for structures showing open and closed flux paths within the particles taking into consideration the direction of the applied field. For non square particles the direction of the field could be defined as being along an easy or hard direction based on magnetostatic energy considerations. The hard direction was that which was parallel to the axis of the shorter in-plane dimension of the particle. Fig 5.18 defines the easy and hard axis for a rectangular particle. The orientation of the particle

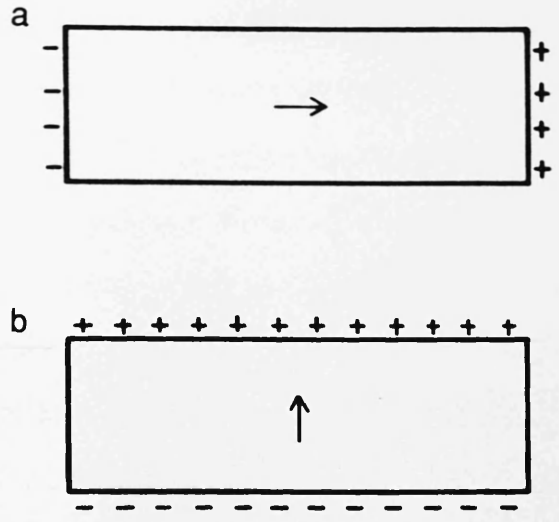

Fig 5.18 Uniformly magnetised states of a rectangular particle.

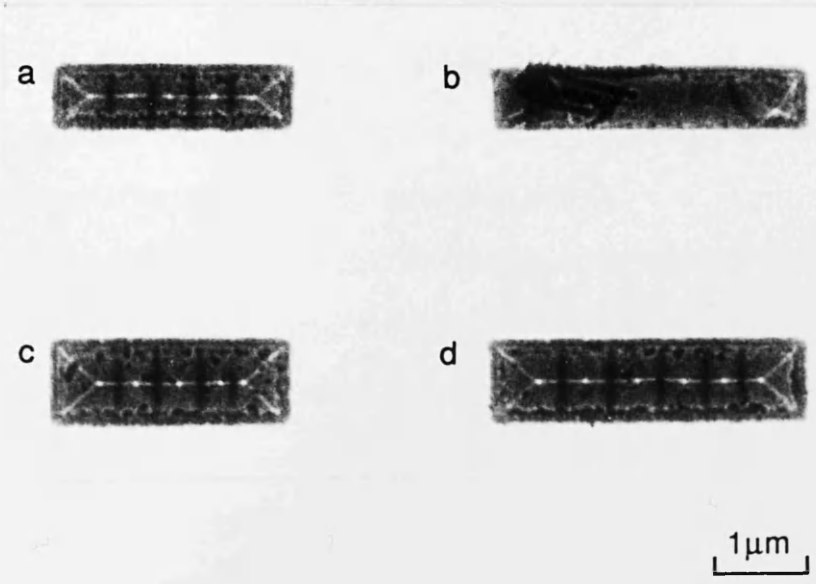

Fig 5.19 Resulting domain structure of 60nm thick particles after application of a field in the ↑ direction.

to the direction of the external field proved to be critical in determining the domain structure supported by the particle.

As in the case of the unmagnetised sample the division between the category I and II particles occurred at an aspect ratio of n=4. Firstly the structure of particles subjected to an in-plane hard axis field are considered. Typical examples of the category I structures induced by such a field are given in fig 5.19. This type of structure is the category Ic structure defined in section 5.3. Essentially this was similar to the Ib structure observed in the unmagnetised sample in particles such as those in fig 5.7 (a) and (c). In the magnetised sample the particles contained relatively long sections of 180^{o} walls depending on the aspect ratio of the particles. The Ib structures seen in the unmagnetised state contained sections of cross-tie wall with normally only one cross-tie being present in the wall. By comparison in fig 5.19 many cross-ties were observed in the 180^{o} wall sections. The length of the ties appeared to be determined by the proximity of the particle's two long edges as did the cross-tie spacing. This is in agreement with the observations of Herman et al (1987) who proposed that the wall energy of a cross-tie close to an edge will have additional magnetostatic energy terms and thus be different from that calculated for an infinite sheet.

Particles magnetised along their easy axes displayed completely different flux closure structures. Typical configurations adopted by the particles are shown in fig 5.20. The most notable characteristic following this field application was that the domain structures of particles with integral aspect ratios (≤ 4) was that of the category Ia structure. This is clearly illustrated in fig 5.20(a), (b) and (c) for particles with n=3, 2 and 2 respectively. Domain geometries such as these did not contain 180^{o} walls. Particles with a non-integral aspect ratio tended to have the category Ib structure they possessed in their unmagnetised state as in fig 5.20(d). Exceptions to this

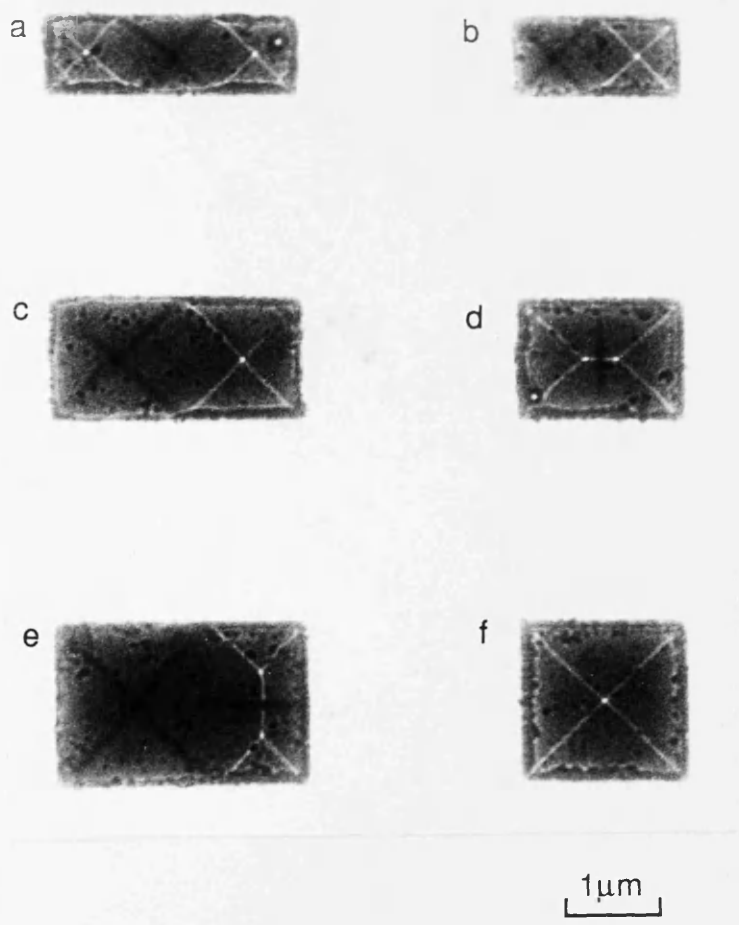

Fig 5.20 As fig 5.19 for field in the → direction.

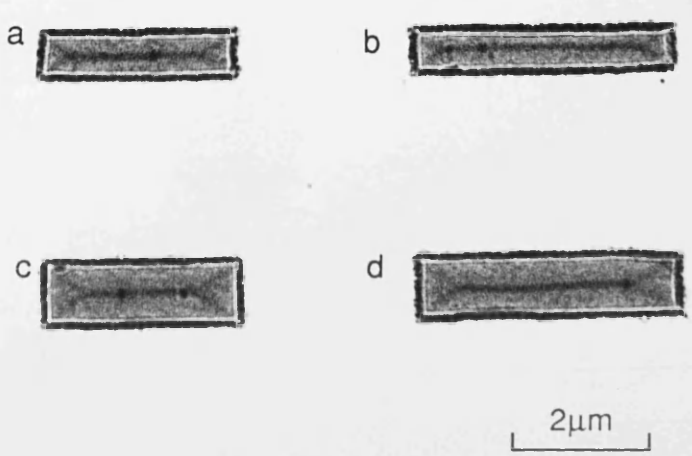

Fig 5.21 Particles in 20nm thick sample after external field applied in ↑ direction.

case were also observed as in fig 5.20(e) which shows a fairly simple structure not observed in the unmagnetised state.

5.6.2.2. 20nm Thick Sample

The experiments of the previous section were also performed on 20nm thick samples and the resulting domain structures were remarkably similar to those displayed by the 60nm thick sample. Again the domain structure of particles with category I structures was dependent on the direction of applied field. Particles which were subjected to a hard axis in-plane field are shown in fig 5.21. These images show the particles to have Ic structures with long sections of 180^{o} walls. The 180^{o} walls did not contain cross-ties only a single Bloch line in each case where the polarity of the Neel wall changed sign. By comparison when the particles were magnetised in the easy direction a mixture of Ia and Ib structures was noted. The Ia structures were seen in particles with integral values of n although, as in the unmagnetised state, this structure also accommodated particles with non-integral n.

5.6.3. Summary of In-plane Field Application For Category I Structures

Category I structures, in this case those with $n \leq 4$, present in these samples showed different domain characteristics depending on the orientation of the applied external field. In both cases it has been shown that for particles with integral n (≤ 4) there exists two simple and stable domain configurations that can occur depending on the magnetic history of the sample.

5.7. Samples Deposited in an Aligning Field

A sample of thickness 40nm was made in which a magnetic anisotropy was induced. This was achieved by depositing the permalloy onto the substrate in the presence of an aligning field. Two Co-Sm permanent magnets were used to produce the field whose magnitude was determined by the separation of the magnets. A field of $3x10^4 A.m^{-1}$ was used with the sample being placed between the north and south poles of the magnets. The sample was observed in the as grown state and after the application of fields in three orthogonal directions in order to check any differences in behaviour from the isotropic sample.

5.7.1. As Deposited State

Examination of the particles in the as grown state was performed once the sample had been removed from the aligning field. A factor which may have affected the resulting structures was the removal of the sample from the field. This was performed as carefully as possible to avoid the particles experiencing any large component of field other than that along the predetermined easy axis.

The easy axis was chosen to coincide with one of the major frame axes of PAT1 i.e. either the X or Y axis of fig 3.7. In the present case this shall be regarded as the Y axis.

Results from this sample in the as deposited state almost duplicated the structures observed in the isotropic sample after the application of in-plane fields as described in section 5.6.2. The most notable aspect of the observed structures was that the division between the category I and II domain

structures occurred at n=8. This meant that the particles possessing incomplete flux closure were restricted to a small number of long thin particles. All the remaining particles, with category I structures, displayed magnetic contrast suggesting that they had solenoidal magnetisation distributions with very few being irregular in structure.

Classification of the category I structures was similar to that in section 5.6 and was dependent onthe orientation of the particle to the aligning field. With the easy axis being the Y axis of PAT1 (fig 3.7) the domain structures can be thought of as being in two groups, those below the line Y=X and those above it. The particles below this line could be thought of as lying along the easy axis whereas the particles above the line were regarded as being unfavourably aligned as their longer in-plane dimension was perpendicular to the easy axis.

Domain structures of particles in the as deposited state are shown in figs 5.22 and 5.23. Fig 5.22 indicates the structure seen in every particle above the dividing line Y=X for n≤8. All of these structures are recognised as belong to category Ic and the similarities between this and fig 5.19 is obvious. The only difference is that the configuration was adopted for particles of higher aspect ratio in this case. As in section 5.6.2.1 the density of cross-ties increased with a decrease of the smaller in-plane dimension as the tie length inevitably decreased. Theory for cross-tie walls (Kosinski 1977) predicts that for a magnetic material with $A=10^{-11}J.m^{-1}$, $M_S=8x10^5A.m^{-1}$, $K=10^2J.m^{-3}$ and thickness 60nm the tie spacing should be ~2μm. Although the structures of figs 5.19 and 5.22 were from samples deposited under different conditions it was clear that the cross-tie length and separation were determined by the dimensions of the particles.

Particles whose long axis was parallel to the aligning field also displayed similarities to the isotropic particles which had been subjected to an external field in the same direction as is shown in fig 5.23. Category Ia domain

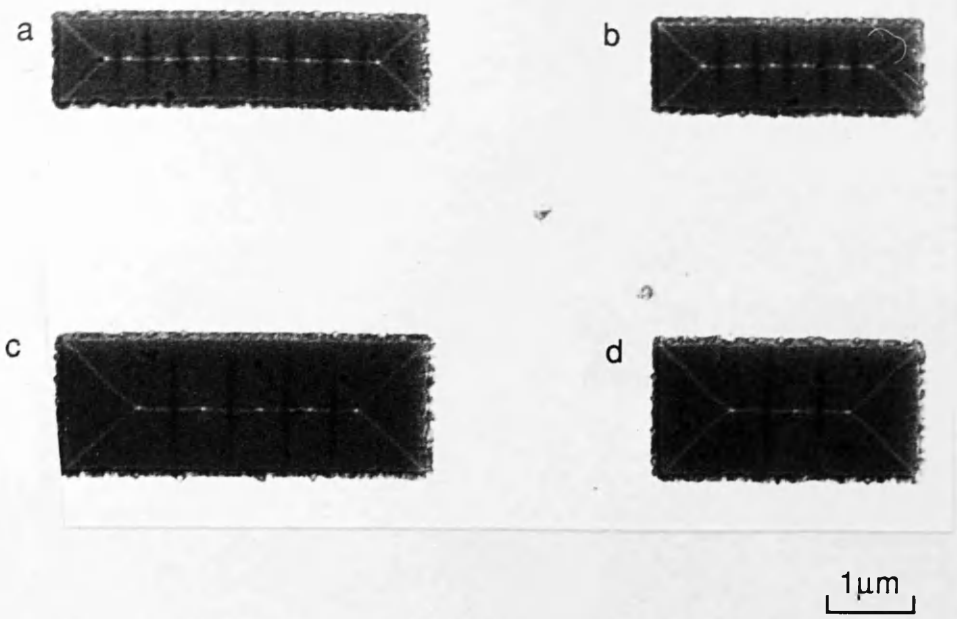

Fig 5.22 Image from 40nm thick sample deposited in an aligning field of 32kA.m^{-1} in the ↑ direction.

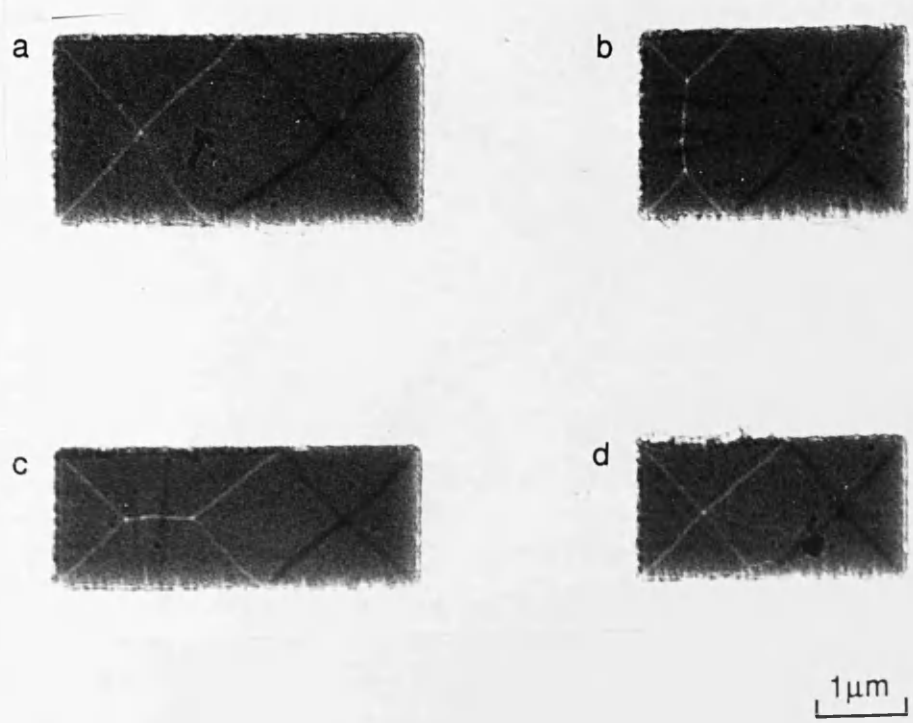

Fig 5.23 As fig 5.22 with field in the → direction.

structures were present in almost all of the particles with integral aspect ratio as seen in fig 5.23 (a) and (d). A few anomalies occurred in this sample e.g. some particles with n=6 displayed the Ia structure expected for a particle with n=5 i.e five criss-crosses of 90^{o} walls. The particles with non-integral aspect ratios displayed a mixture of Ib and Id structures along with a few flux closure structures such as those shown in fig 5.23(b).

As mentioned earlier category II domain structures were present in particles with $n \geq 8$. The Fresnel mode was not suitable for observing magnetic contrast in these thin particles and although both of the structures shown in fig 5.9, appeared to be accommodated in the particles the limitations of this mode allows little comment to be made on them.

5.7.2. Application of External Fields

This sample was subjected to three orthogonal external fields in the same manner as the isotropic samples discussed in section 5.6.2. Again the objective lens of the JEOL 1200-EX was used for the out of plane hard axis field. The most noteworthy effect of this field was to introduce many more category II domain structures than in the as deposited state. This meant that the transition from category I to II structures occurred at n=4. The category I configurations which were present in this sample did not allow easy classification. In addition, irregular domain structures such as those in fig 5.17 were observed. For particles oriented perpendicular to the easy axis (i.e. above the line Y=X) many category Ic structures still remained although some Ia structures appeared in particles with integral values of n. Particles oriented lengthwise to the easy axis displayed Ia, Ib and Ic structures. Thus the main effect of this field was to disturb the uniformity of the domain structures seen in the as grown state.

Two in-plane external fields were also separately applied to the sample. The direction of these fields were parallel and perpendicular to the easy axis. Like the application of the hard axis (out of plane) field the effect of these in-plane fields was to introduce a number of irregular category I structures with no particular order among the regular structures. The results were in contrast to the same experiments on the isotropic samples given in section 5.6.2. One point of interest was that after the application of the in-plane fields the transition between category I and II structures was different for particles oriented along and perpendicular to the easy axis. In both cases the particles with the longer dimension aligned to the easy axis showed the transition to occur at n~6 whereas the particles perpendicular to these displayed the transition at n~3.

5.8 Summary

The main results of this chapter are summarised in table 5.1. An overall impression from the observations emphasises the important factors in determining the domain structure of a particle as being its shape, thickness and magnetic history. There is certainly no unique structure for every shape of particle although certain structures were found to occur more frequently than others under specific conditions. The implications of the results in this chapter form the basis of the calculations and discussion given in chapter 8.

CHAPTER 6

DIFFERENTIAL PHASE CONTRAST IMAGING OF PAT1 PARTICLES

6.1 Introduction

The DPC mode of Lorentz microscopy as practiced on a VG HB5 STEM was described in detail in chapter 2. In this chapter the results are presented from a study of the samples of thickness 20 and 60nm in the as-deposited state. Confirmation of the flux closure structures deduced using the Fresnel mode and reported in the previous chapter are given in section 6.2 along with an investigation of the magnetic structure present in the smallest particles produced so far. As the DPC mode is sensitive to the presence of stray fields it is ideal for the examination of domain configurations which give rise to incomplete flux closure. In section 6.3 the category II structures of PAT1 are considered.

The high resolution available using the STEM allows quantitative information on the micromagnetic structure in the particles to be extracted. In particular the different types of domain wall encountered can be studied in detail. The techniques used to recover domain wall profiles from digitally acquired images are described in section 6.4 together with values of domain wall width obtained using these procedures on DPC images of PAT1 particles.

6.2 Flux Closure Structures (Category I)

Fresnel studies of the particles given in chapter 5 suggested that, for

many of the particles, a flux closure domain structure was energetically favourable. This resulted in very regular domain configurations which were presumed to have the magnetisation distributions categorised in section 5.3. Images mapping the integrated components of induction within these particles, as generated using the DPC mode, substantiate the results of the previous chapter. The type of images obtained are shown by example in fig 6.1 from a 20nm thick 4 by 2μm particle in PAT1 which has a category Ia structure. The direction of induction which the detector is sensitive to is indicated by the arrows and a schematic diagram of the magnetisation distribution within the particle is drawn in fig 6.1(c). The images are clearly consistent with this representation where the magnetisation stays parallel to the edges of the particle in order to avoid the formation of free poles at the surfaces. Also the signal level outside the particle, apart from showing structure in the Si_3N_4 substrate, corresponds to there being no stray field in this region. This is made clear by noting that the signal levels in domains orthogonal to the direction of sensitivity of the detector are the same as those outside the particle.

The differences in domain structure produced by the flux closure mechanism at the two thicknesses are highlighted in figs 6.2 and 6.3. These show the images from a 4 by 1.5μm particle of thickness 20 and 60nm respectively. Fig 6.2 reveals that the category Ia structure is present in the thinner particle and is achieved by wall curving. Again the induction maps show that the magnetisation stays parallel to the edges of the particle. A schematic diagram showing the magnetisation distribution with the curved walls is given in fig 6.2(c). It is evident that the avoidance of free poles at the edges of the particle is a major factor in the formation of the magnetisation distribution in such a particle. Although the magnetisation appears to lie parallel to the edges in the vicinity of the edge regions, inside the particle the

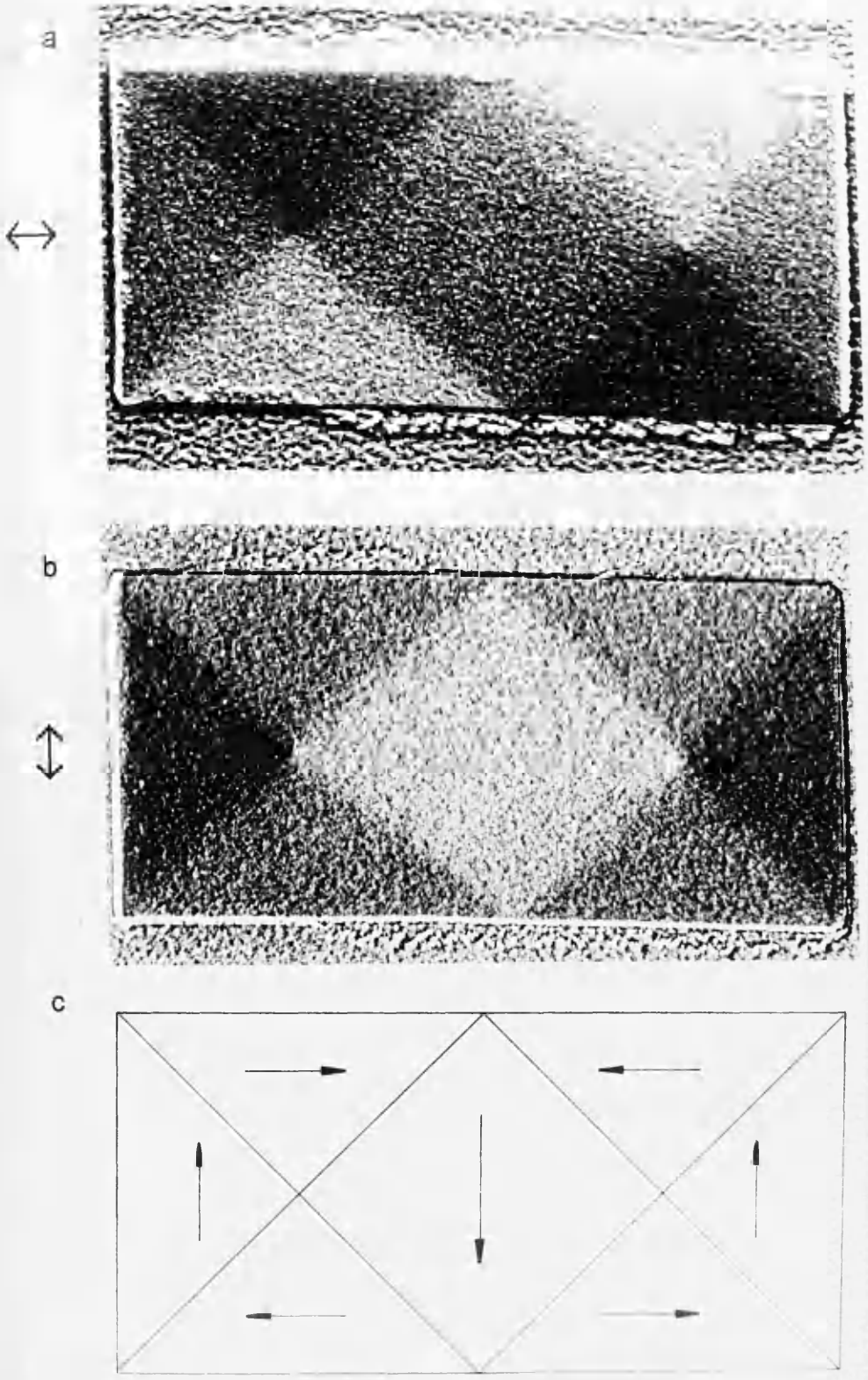

Fig 6.1 DPC images of a 4 by 2µm 20nm thick particle. The configuration of the detector is such that the components of induction mapped are shown by the arrows at the side of the figures and a schematic of the magnetisation distribution is given in (c).

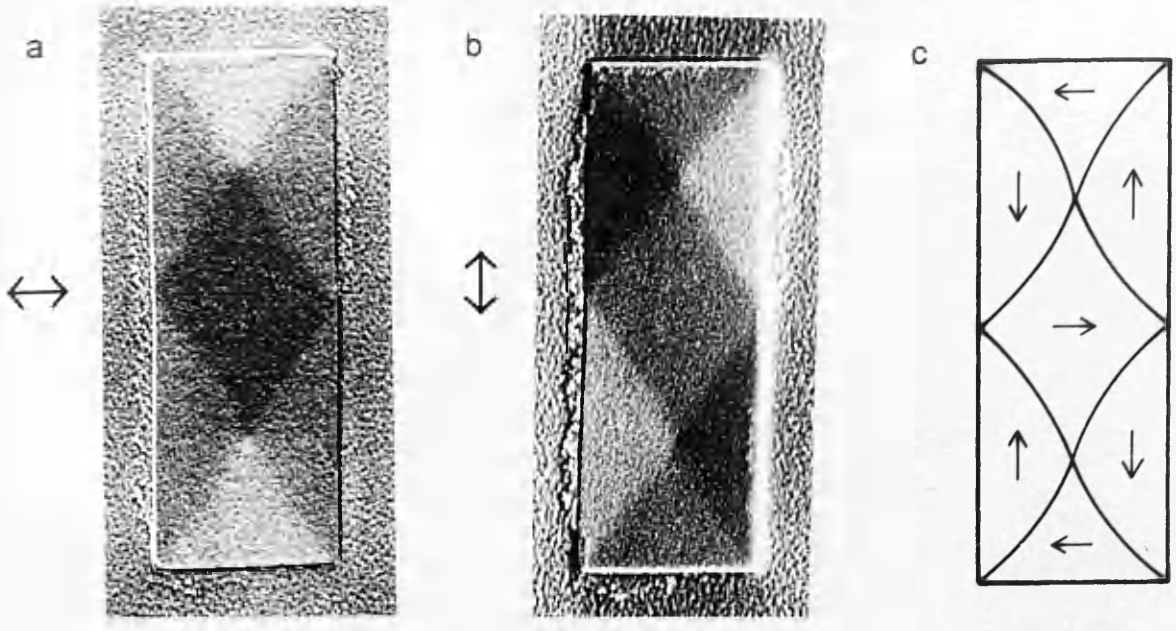

Fig 6.2 DPC images of 4 by 1.5µm particle of thickness 20nm showing category Ia domain structure.

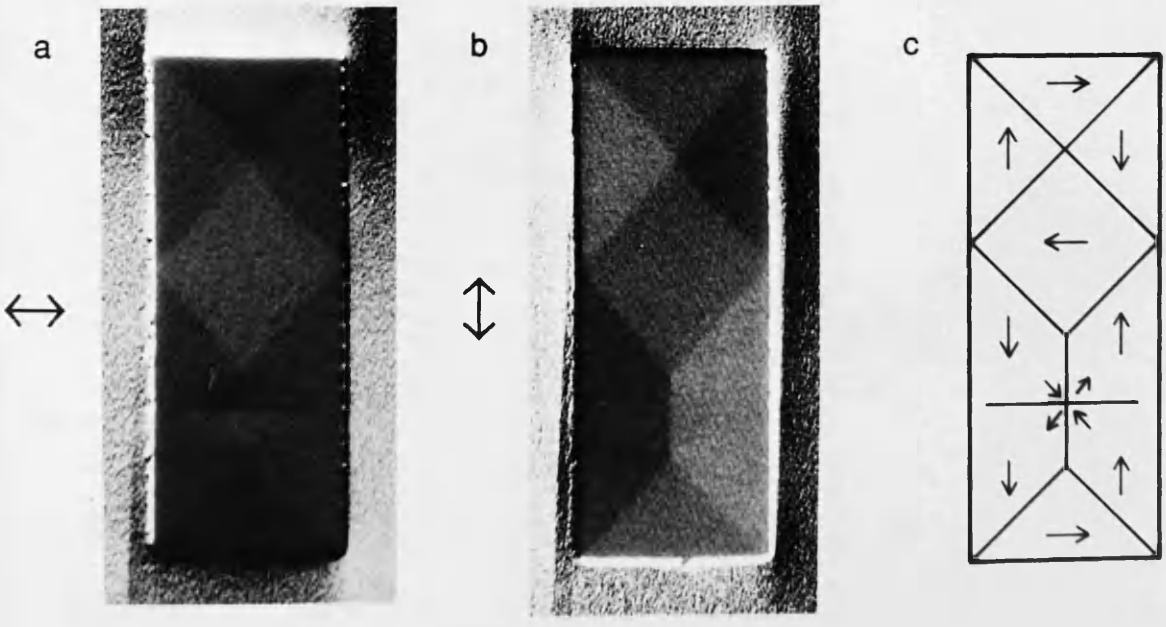

Fig 6.3 As fig 6.2 for a 60nm thick particle showing category Ib domain structure. The signal variation outside the particle is an artefact of this particular image.

walls curve and this is consistent with a variation in the angle of rotation of the magnetisation along the wall. This leads to a non zero value for $\nabla.\underline{M}$ in addition to the fact that the walls in these particles are expected to have long 'tail' regions (Hubert 1970) which are not divergence free.

The category Ib structure is demonstrated in fig 6.3 for a 60nm thick particle which comprises domains separated by straight 90^{o} walls with a section of cross-tie wall present also. The induction distribution around a cross-tie is discussed in more detail in section 6.4. These last two images emphasise the importance of the film thickness in determining the domain structure in a particle of certain in-plane dimensions as both the magnetostatic and domain wall energies are critically dependent on the film thickness.

The category Ia domain structure displayed in many of the particles with integral aspect ratio is shown in fig 6.4 for a 60nm thick particle with n=4. Clearly all the domains are separated by straight 90^{o} walls as expected from the preliminary Fresnel study. Again complete flux closure is clearly achieved within the particle.

Another interesting feature is shown in fig 6.5. This is of a 20nm thick particle which has a section of 180^{o} wall. A Bloch line is present in this wall and it is apparent from these images that, as expected from section 5.5, the magnetisation follows a circular path round this point. This is most prominent in fig 6.5(a) where the strong component of magnetisation normal to the wall is illustrated.

The Fresnel mode was unsuitable for studying the smallest particles as it is an out of focus technique and is limited to low magnification when practiced on the JEOL 1200-EX. The DPC mode was not restricted by these limitations and as such allowed the domain structures of the very small particles to be examined. Fig 6.6 shows such a particle of thickness 20nm

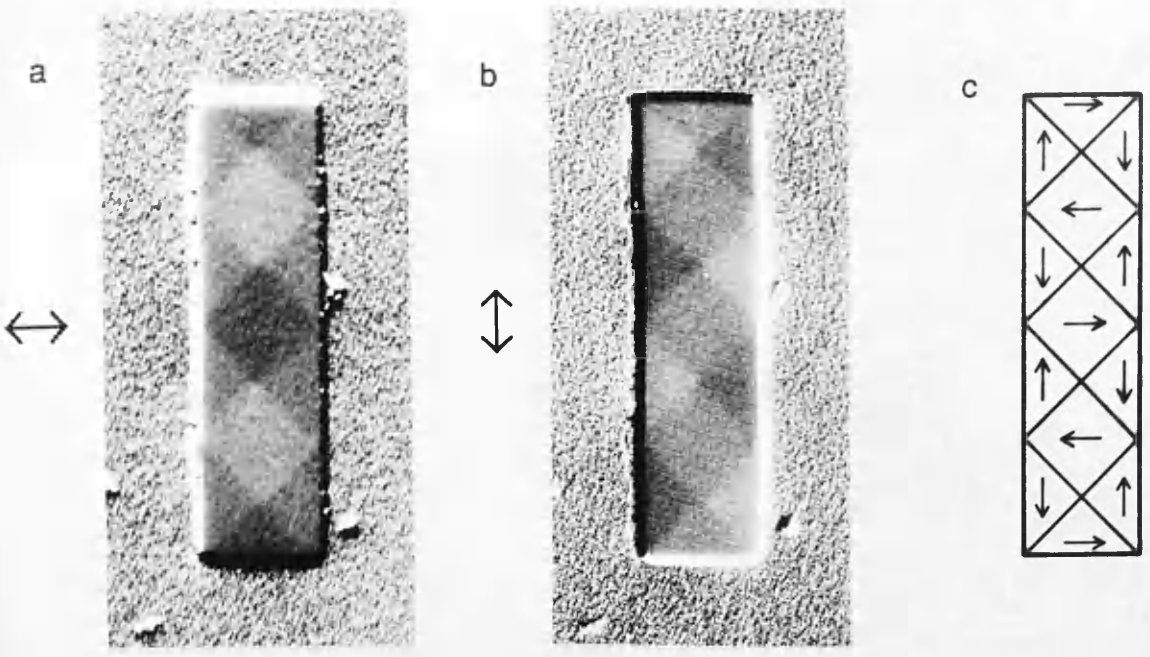

Fig 6.4 DPC images from a 3 by 0.75μm particle of thickness 60nm which possesses a category Ia domain structure.

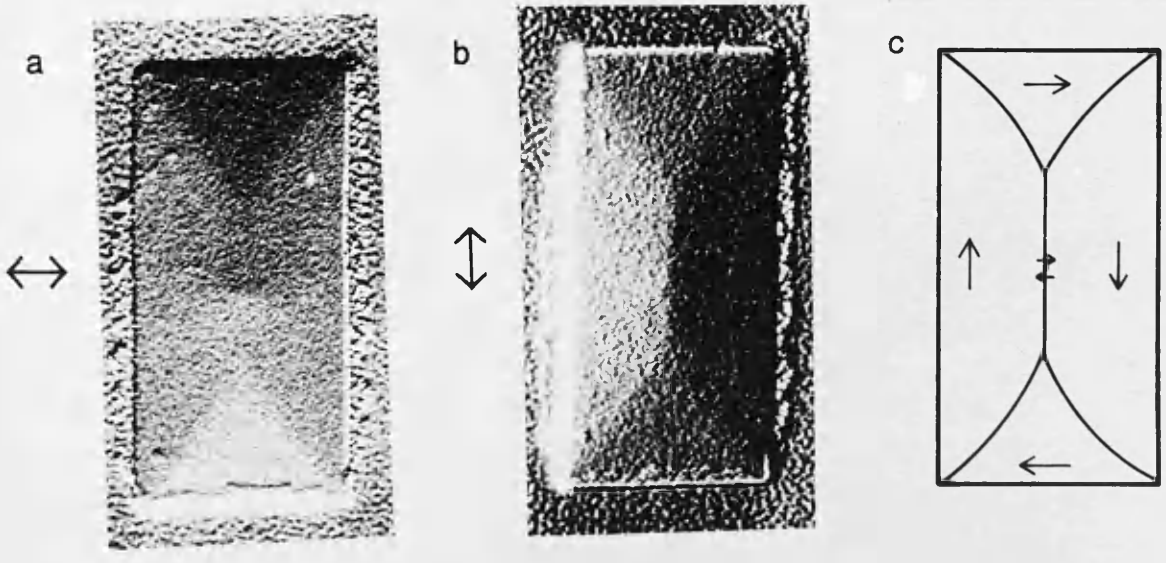

Fig 6.5 Category Ic domain structure in 20nm thick 3 by 1.5μm particle.

whose in-plane dimensions are 0.5 by 1.0μm. Although the contrast in the images is low the particle appears to possess essentially the same domain structure as the particle in fig 6.5 i.e. a category Ic structure.

6.3 Imaging Stray Fields

In this section particles which were classified as displaying category II structures are discussed. As these particles were presumed to possess incomplete flux closure the DPC mode was used to verify directly the existence of stray fields produced by these domain configurations.

6.3.1 Category II Structures

From the Fresnel examinations of PAT1, as discussed in chapter 5, it was noted that certain particles possessed complicated domain structures which indicated that flux closure appeared to be incomplete within the particle. As the domain structures appeared not to be as simple as the category I structures, especially in the thicker sample, the magnetisation distributions presented in section 5.5 for the category II structures could not be assumed to be correct without further experimental evidence.

A low magnification image of a 60nm thick particle with a category IIb domain structure is shown in fig 6.7 clearly illustrating that stray fields are detected. The stray field distribution around the particle is interesting as it bears some resemblance to that of a bar magnet although it appears somewhat asymmetric. This then suggests that the poles are situated at the ends of the particle where $\underline{M}.\underline{n}\neq 0$. The stray field distribution outside the particle is shown schematically in fig 6.7(c). Although some internal structure is visible within the particle it is not considered at the moment as these images are simply intended to show the capability of the DPC mode for

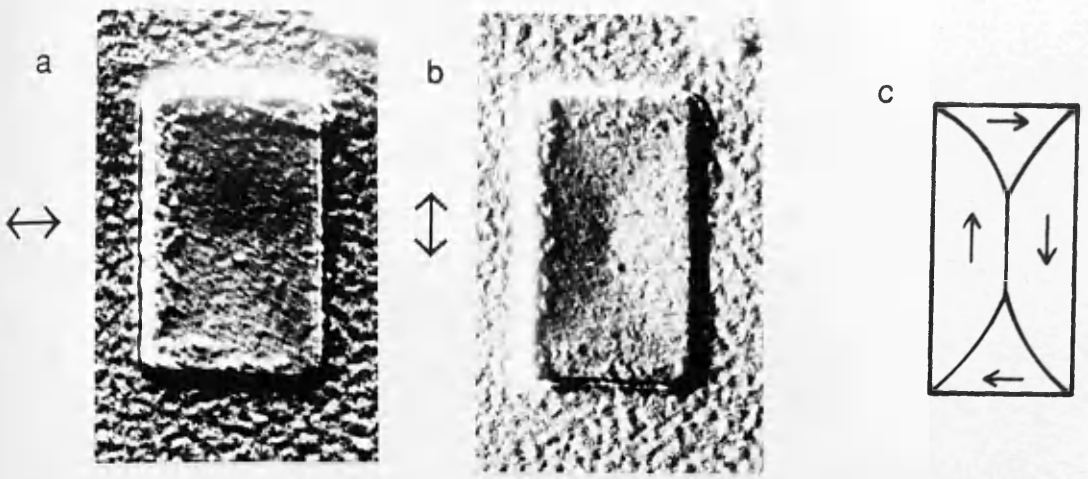

Fig 6.6 DPC images of 1 by 0.5μm 20nm thick particle.

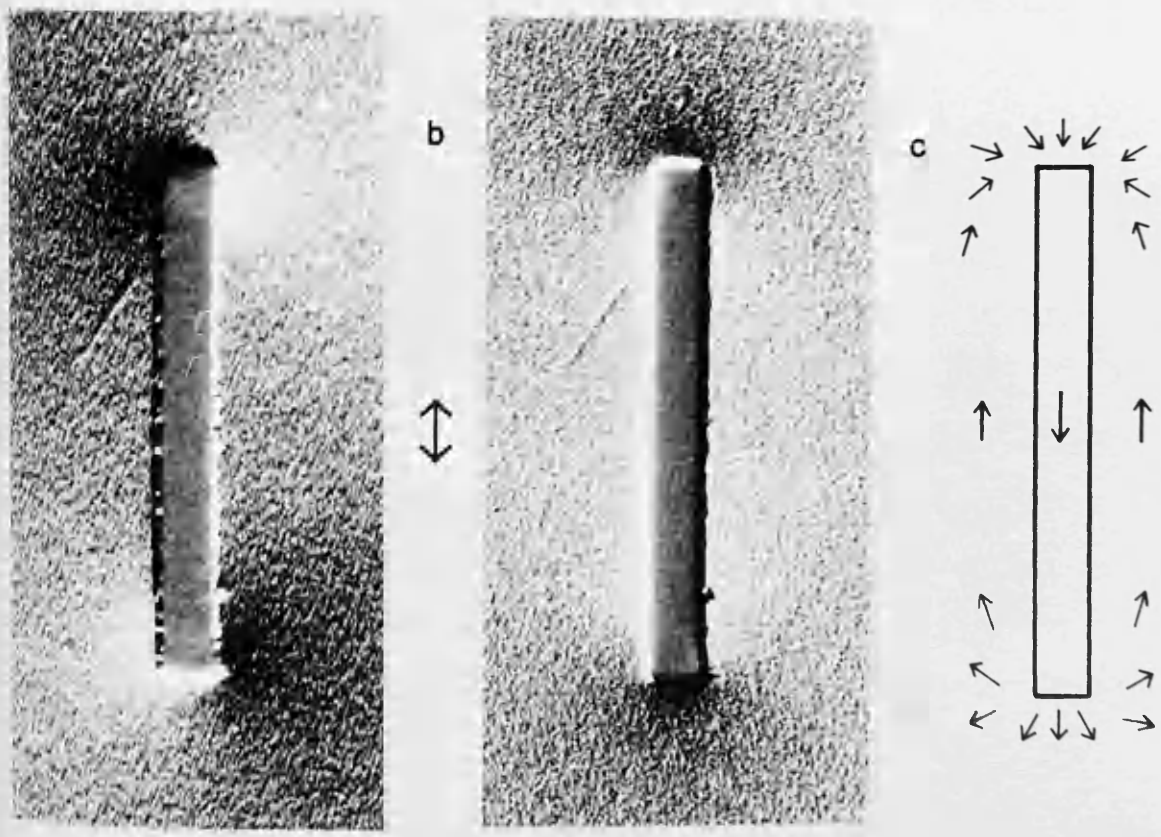

Fig 6.7 DPC images showing stray field distribution around a 3 by 0.25μm particle with incomplete flux closure. The schematic in (c) shows only the stray field distribution.

detecting stray fields. The internal magnetisation distribution of a similar particle is discussed in detail later in this section.

In the previous chapter it was noted that the category II' structures observed in the 20nm thick sample seemed to have a fairly simple magnetisation distribution. A 4 by 1μm particle is shown in fig 6.8 along with a schematic representation of the magnetisation distribution within the particle deduced from the two images. The structure observed represents a trend towards a uniformly magnetised single domain particle. In this case the particle was uniformly magnetised parallel to its length at the centre as shown in fig 6.8(c) but a pronounced curling of the magnetisation occurred at the ends to reduce the magnetostatic energy associated with the particle. This takes the form of a curved domain wall and results in flux leakage at the ends of the particle although the amount of flux leaving the ends appears to be less than that of a uniformly magnetised rectangle.

By comparison the images taken of a 4 by 1μm particle with a category IIb structure in the 60nm thick sample indicated that the variation of the magnetisation within the particle was somewhat more complex. The intensity variation, outside of the particle, is shown in fig 6.9. The schematic diagram of the magnetisation distribution within the particle corresponds to the formation of free poles at the edges required to generate such contrast. Again it is apparent that the particle is uniformly magnetised along its length in the centre although the magnetisation at the ends deviates strongly from this direction. This rotation of magnetisation at the ends of the particle appears to provide a degree of flux closure although it is evident from these images that $\underline{M}.\underline{n} \neq 0$ in these regions.

The differences between the category II structures at the two thicknesses is evident. The fact that the two structures are so dissimilar

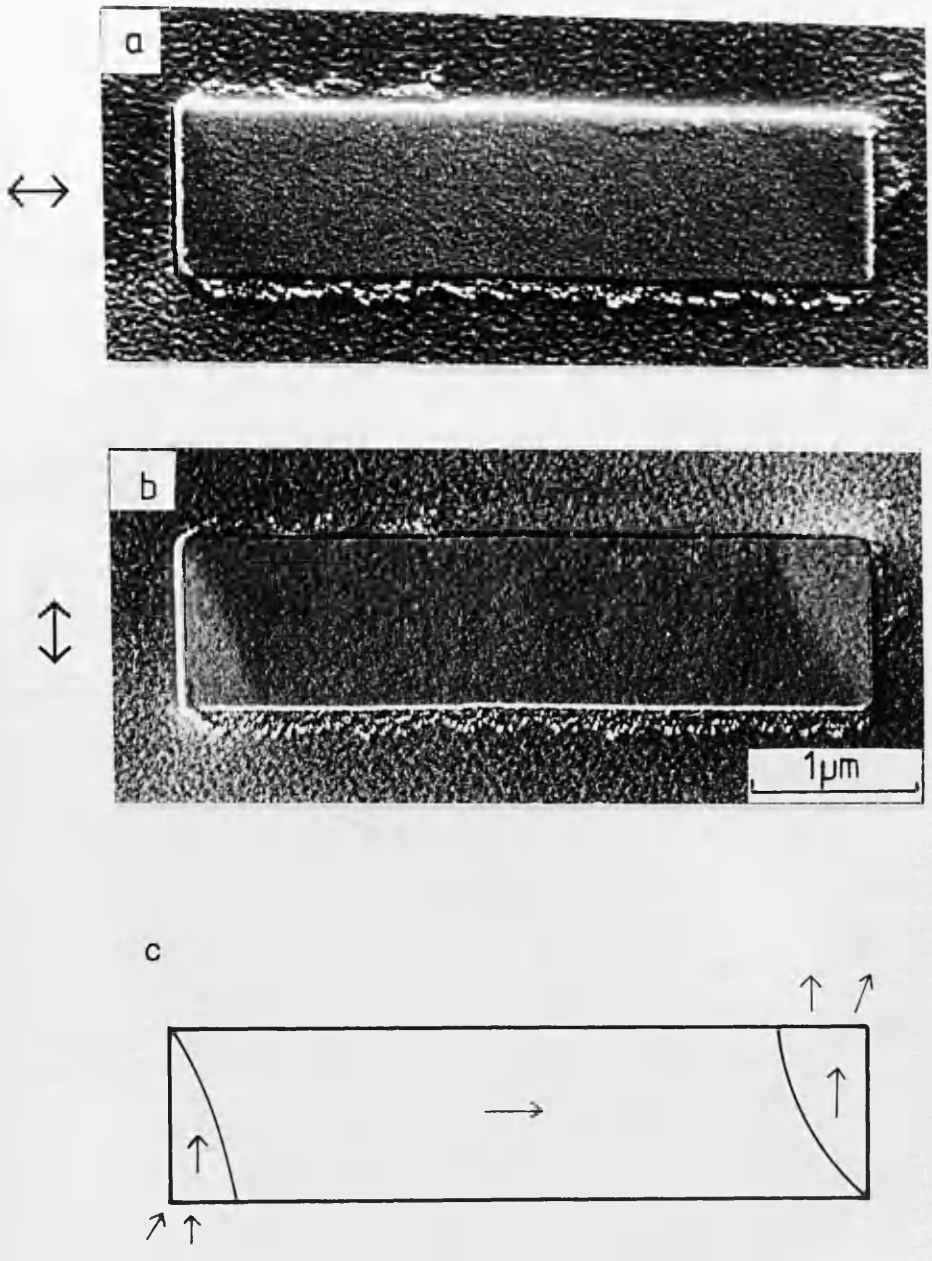

Fig 6.8 Category IIb' structure in a 20nm thick 4 by 1µm particle.

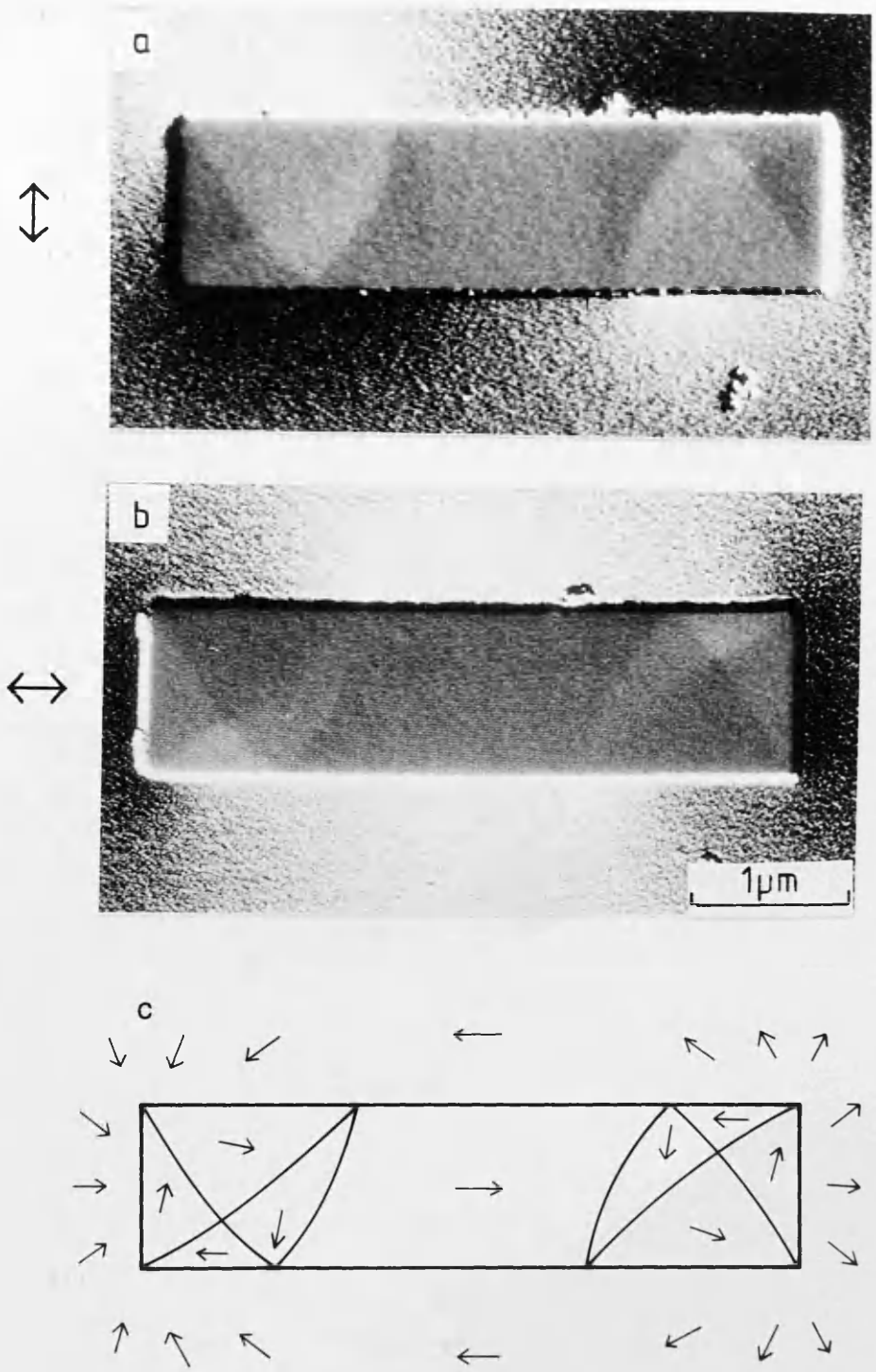

Fig 6.9 Category IIb structure in a 60nm thick 4 by 1μm particle.

reflects the differences in relative magnitudes of the magnetostatic and wall energies at the two thicknesses.

6.4 Domain Wall Structures

The signal intensities displayed from difference signals from the quadrant detector are linearly proportional to the integrated components of magnetic induction. This means that the signal variation detected across a domain wall, for example, represents the induction profile of the wall and this has been shown to give excellent results for walls with vortex like structures (section 3.2.2) by Chapman et al (1985). Signals from the quadrant detector can be digitised and stored in a frame store where subsequent image processing may be performed. The procedures for obtaining wall profiles from these images are those developed by McFadyen (1986). Information extracted from these samples allowed wall widths to be estimated and compared with those from theoretical models.

Firstly the magnetisation variation around a region of cross-tie wall is investigated.

6.4.1. Cross-tie Wall Structure

In the previous chapter it was noted that cross-tie walls existed in the permalloy films with a thickness of 25nm or greater. For films of thickness 60nm these wall sections were usually short in the as deposited state so that any wall normally had only one cross-tie in it. Also the length of the cross-tie was noted to extend across the particle making the length of the cross-tie approximately equal to the L_2 value of the particle. From theory (Kosinski 1977) the length of a cross-tie for a film of certain thickness is predicted to be

fixed for a film of infinite extent in the plane of the film. The DPC images from a section of cross-tie wall in a 60nm thick film are shown in fig 6.10 along with a schematic representation of the magnetisation distribution. The strong component of magnetisation normal to the main wall section is clearly indicated in fig 6.10(b) and the structure of the wall is seen to comprise essentially 90^{o} wall sections. This is an important point to remember when considering the wall profiles obtained in the next section.

6.4.2 Quantitative Domain Wall Structures

A single line trace of signal variation across a DPC image of a domain wall corresponds to the one dimensional induction profile of the wall (Chapman et al 1985). This is certainly true for a defect free, single crystal film of a soft magnetic material where the wall width is considerably greater than the electron probe size. However from a study of the physical microstructure of the samples in this project, in section 5.6, it was established that the particles were polycrystalline in nature with grain sizes in the range 5-10nm. The images presented so far in this chapter confirm the micropolycrystalline structure of the film and that this structure contributes significantly to the signal variation observed in these images. Thus the signal variation contains non-magnetic information. An illustration of the difficulties presented by this effect is shown in fig 6.11 of a single line trace across a 180^{o} wall in a 20nm thick particle. The signal variation caused by the individual crystallites is very large and almost conceals the underlying magnetic contrast. The crystallites are essentially randomly oriented to the domain wall and so by adding successive line traces the effect is to average out the signal variation due to the crystallites while enhancing the magnetic contrast. Unfortunately the domain wall may not necessarily be in the correct orientation to enable this process to be

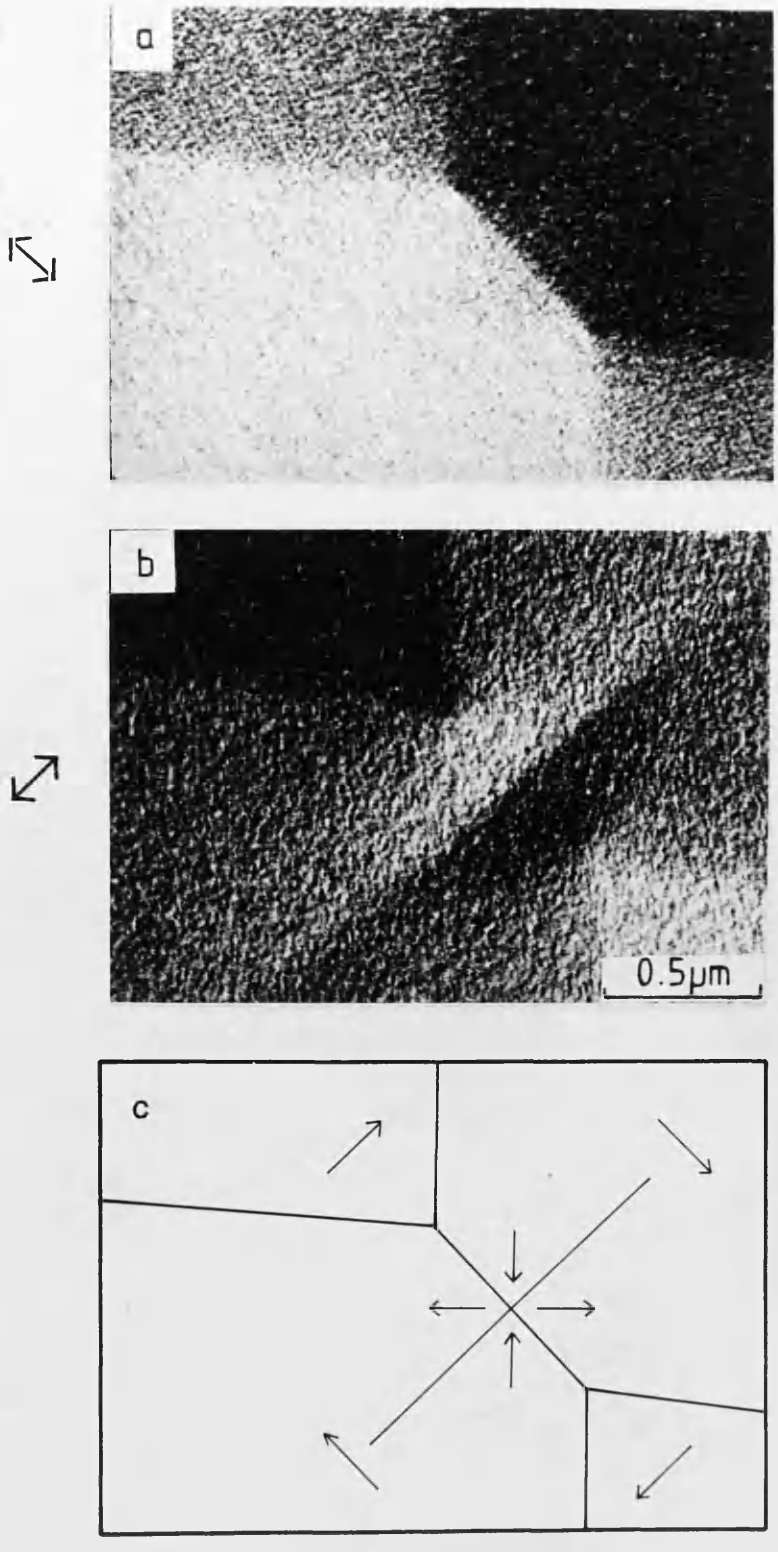

Fig 6.10 DPC images showing induction distribution around a cross-tie in a 60nm thick particle.

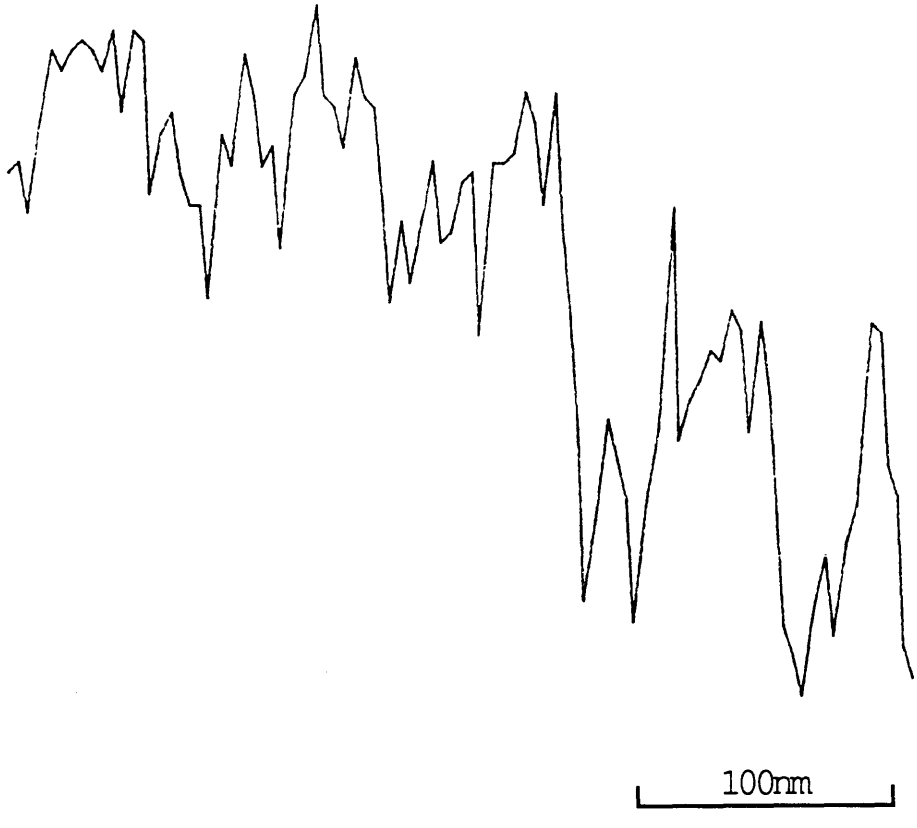

Fig 6.11 Line trace showing signal variation across a digital DPC image of a 180^{o} domain wall in a 20nm thick particle.

performed directly and may have to be aligned to be parallel to the edge of the picture frame. This can be achieved in a number of ways as described in the following sections.

6.4.2.1 Alignment of Domain Wall Images

Alignment was performed using programs written for the Toltec computer and developed by McFadyen (1986). The alignment procedure is summarised as a series of steps as follows:

1. The digitally acquired image containing the domain wall to be aligned is stored in memory and output to the display screen using the program PCTG.

2. A section of wall in the image to be aligned is defined by drawing a box on the screen with the program IGET.

3. The section of wall is aligned using the program RASP. Alignment is achieved by means of a least squares comparative routine (McFadyen 1986).

4. The rows in the aligned image can then be added together to give a single line profile which is output to the plotter.

The major problem encountered here is that the alignment routine does not work for images which contain strong crystallite contrast, such as those obtained from the samples in question, as the routine will tend to align to a non-magnetic feature. A number of methods of overcoming this problem are

possible and are outlined below.

6.4.2.2 Alignment Using a Test Pattern

A pattern with very strong contrast at a slope which matches that of the domain wall of interest can be generated using the program PCTG. Generating such an image is achieved by creating intensity ramps parallel to the picture frame axes which can be added in certain combinations to give a sharp intensity ramp at any angle to match the slope of the domain wall. This standard pattern can easily be aligned using RASP and the information on the shift of each row is stored and can then be applied to the original image. This technique works very well for straight domain wall sections and has the advantage of being easy and quick to implement.

6.4.2.3 Alignment Using Frequency Filtered Images

This method is more time consuming than that using the test pattern as it involves computing Fourier transforms of the images. The principle behind it is that the spatial frequency spectrum of the crystalline and magnetic signal are substantially different. By studying the relation between an object in real space and its corresponding frequency spectrum in Fourier space enables a possible filtering process to be decided upon.

Normally an image frame consists of 256 by 256 pixels each of which has a width dx dependent on the magnification of the image. The corresponding pixel width in Fourier space is then dk=1/(256.dx) and the image extends from -128.dk to +128.dk in both the x and y direction. If a feature in real space exhibits a periodicity every N pixels this then produces an intensity peak at 256/N pixels in Fourier space. The frequency spectrum

of a high magnification image of a domain wall consists of a high and a low frequency contribution. As the two domains usually cover the entire image they give rise to intensity peaks of very low spatial frequency which will be situated near the centre of the Fourier transformed image. On the other hand the periodicity of the crystallites in real space which is of the order of 6 or 7 pixels in an image at 100kX magnification means that peaks in intensity in the Fourier image will occur at around 40 pixels from the centre of the image. From this information it is evident that the high and low frequency signals can be separated.

Fourier transforms were performed on the Toltec using the suite of FFT(Fast Fourier Transform) programs. To obtain a frequency filtered image firstly requires that the Fourier transform of the original image be calculated and displayed. This represents the spatial frequency map of the image and it is at this point that the frequency filter must be performed. Three different filters were available; a step function, a Lorentzian and a Gaussian function. The result of these filters for the example of the Gaussian function is to replace the original data with,

$$\text{DATA} \rightarrow (\text{DATA}) \,.\, \exp\left(-\frac{k^2}{2\sigma^2}\right) \qquad (6.1)$$

Here k is the distance from the centre of the Fourier distribution and σ is the standard deviation of the Gaussian, both quantities take integral values.

The magnitude of σ is input by the user and is chosen such that the function multiplying the DATA term in equation (6.1) is small at the k value which corresponds to the intensity peak of the crystallite signal. Once the filter has been applied an inverse Fourier transform of the resulting data is calculated and displayed to give the frequency filtered image. The Gaussian

function was found to be the most suitable filter as a Gaussian is unchanged by a Fourier transform. By comparison a step function is markedly changed by a Fourier transform and leads to a distinct ringing effect in the filtered image.

Images produced by the application of the filters show very enhanced magnetic contrast as shown in fig 6.12(b) for a Gaussian filter with σ=15pixels. This is a frequency filtered image of fig 6.12(a) which is a DPC image of a 90^{o} wall in a 20nm thick particle. The section of wall which was to be aligned is the boxed area of fig 6.12(a). The same area is also boxed in the filtered image of 6.12(b) and this area, after being aligned by the RASP program, is shown in fig 6.12(d). From the shift information in the alignment routine the original wall section was then aligned as shown in fig 6.12(c).

6.4.2.4 Experimentally Determined Domain Wall Profiles

The two techniques described in the preceding sections were both tested for domain wall images obtained from the samples in this project. Fig 6.13 shows the column sums of the same area of a 180^{o} wall in a 20nm thick particle which was aligned by both methods. Although the traces are by no means identical, for the purposes of making an estimate of the domain wall width they are both equally suitable. This being the case it was decided to use the procedure based on the standard test pattern (6.4.2.2) as it required less time. (N.B. A single Fourier transform calculation took about 4 minutes to complete for each 256 by 256 image).

It was noted during the discussion of domain wall models for magnetic materials with properties comparable to those of permalloy that many of the walls expected to be present in the samples produced in this project were symmetrical one dimensional Neel walls. The models presented

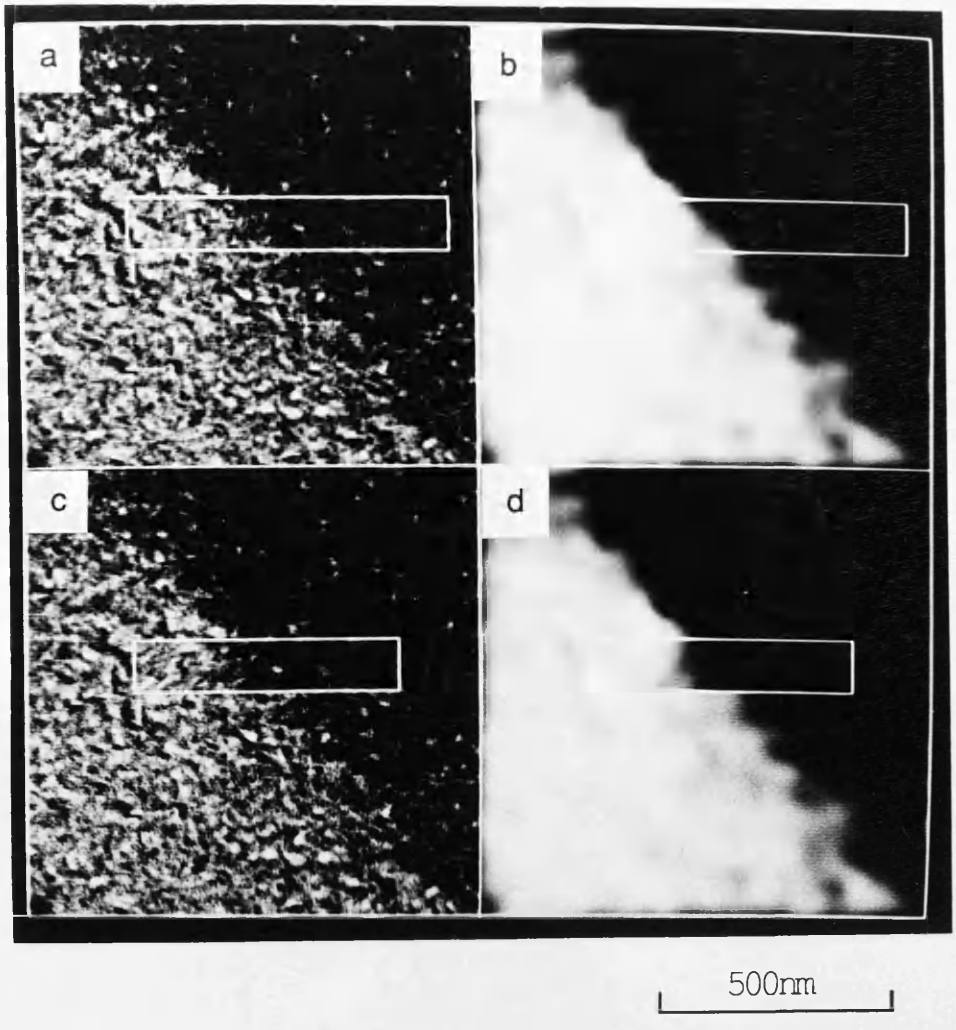

Fig 6.12 Image processing of data using filtering and alignment programs. (a) Original DPC image of 90^{o} wall in 20nm thick sample with boxed area to be aligned, component of induction mapped is shown at the side of the image. (b) frequency filtered image of (a). The area in (b) was aligned using RASP to give (d). The shift information from this process was used to align (a) and is shown in (c).

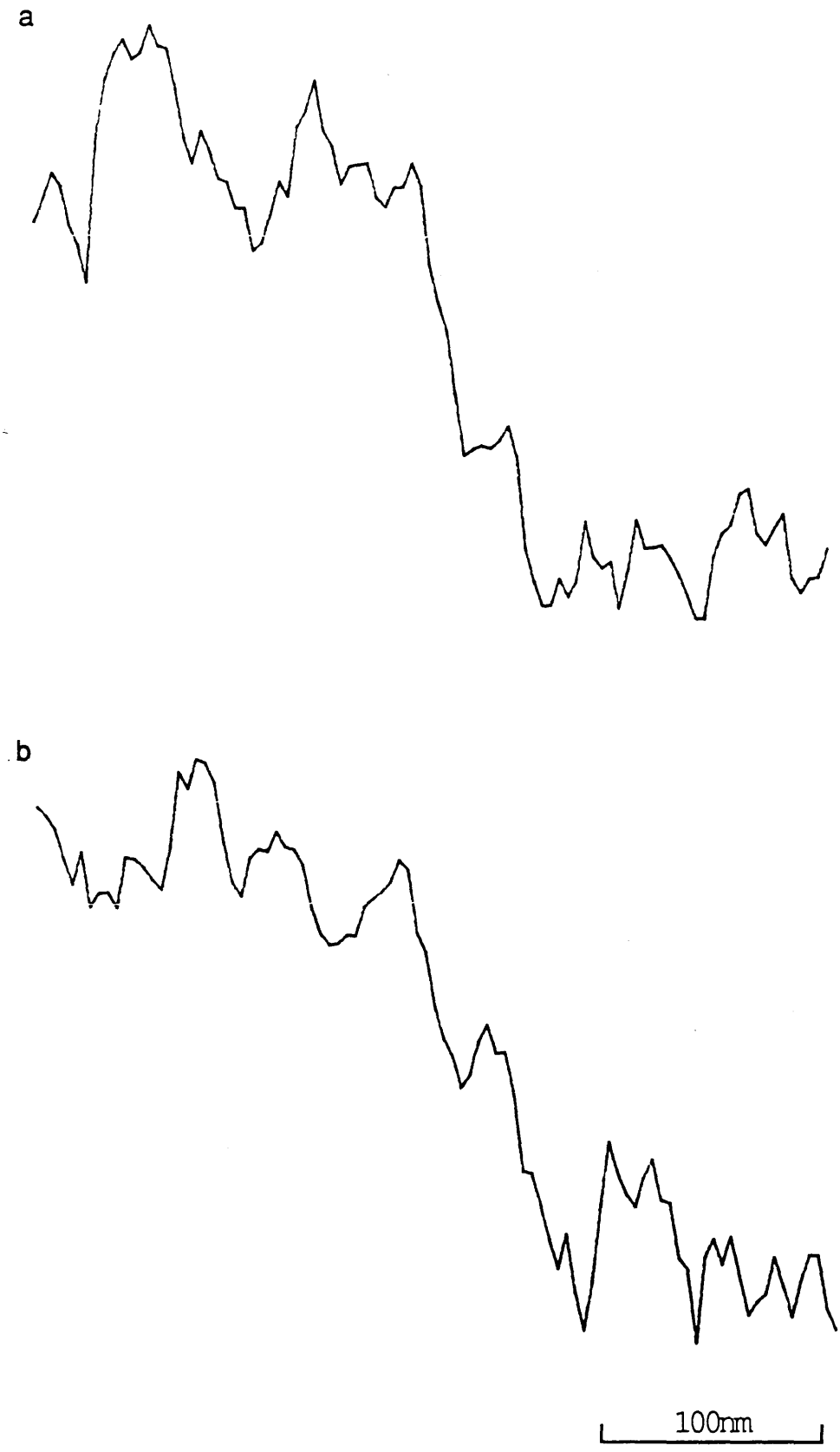

Fig 6.13 Comparison of alignment processes for a section of 180° wall in a 20nm thick particle. The process used in fig 6.12 results in the line profile in (a). (b) shows the result when the same area was aligned to a test pattern.

showed that the structure of the wall consisted of two long tails where the magnetisation slowly rotated to the direction of magnetisation within the domains and a central region in which the rotation was much faster and which had a positive magnetostatic energy associated with it. The tails of these walls in the calculations performed for a thin film (Collette 1964) with infinite in-plane dimensions extended to the order of tens of microns either side of the central region which itself had a thickness of around 100nm.

The typical domain wall profiles that are shown in fig 6.13 obviously cannot give a detailed description of the magnetisation variation within a wall as did that shown by Chapman et al (1985) for a single crystal sample which contained an asymmetric wall. Although the profiles are noisy it is still possible to extract information from the induction variation about the width of the domain walls in these particles with small in-plane dimensions. In order to do this the definition of wall width must be made clear. In chapter 3 it was noted that many definitions of wall width existed and it is proposed to use the following three in order to make comparisons with theoretical models:-

$$w_1 = \frac{2}{\left(\frac{d(B_y(x))}{dx}\right)_{x=0}} \qquad (6.2)$$

$$w_2 = x_h = \text{half width of function} \quad \left(\frac{d(B_y(x))}{dx}\right) \qquad (6.3)$$

$$w_3 = 2\int_{-\infty}^{\infty}(1 - B_y(x)^2)\,dx \qquad (6.4)$$

The symbols used in the equations correspond to those given in section

3.4 with the $B_y(x)$ in the equations being the dimensionless quantity $B_y(x)/B_S$. Also as the signals measured here represent integrated components of induction we use $B_y(x)$ rather than the normally used $M_y(x)$. Equation (6.2) gives a wall width based on a uniform variation of $B_y(x)$ throughout the wall. The second definition measures the half width of the derivative of the function describing the rotation of spins within the wall and has also been shown to be a useful definition when considering divergent wall images in CTEM (Riemer and Kappart 1969). There the w_2 corresponded to the width of the divergent wall images extrapolated to a defocus distance of z=0 for soft magnetic materials with wide walls. Equation (6.4) is that put forward by Jakubovics (1978) in order to give consistent results when different functions are used to fit the same experimental data.

Calculation of these wall widths with the raw data such as that shown in fig 6.13 would be quite inaccurate and require a fair amount of additional work. In order to be able to perform a reasonably quick and accurate analysis of the results here it was decided to describe the induction variation within the walls by a simple function which matched the observed variation. Hubert (1970) concluded that Neel walls in thin soft magnetic films were well described by one dimensional symmetric variations of the magnetisation and a simple function which is commonly used to describe such a variation is,

$$B_y(x) = B_s . \mathrm{TANH}(\frac{x}{A}) \qquad (6.5)$$

where A is a parameter chosen to give the best fit to the experimental profile. This function is shown to be a satisfactory approximation to the induction variation across Neel walls in thin permalloy film from fig 6.14. Here the

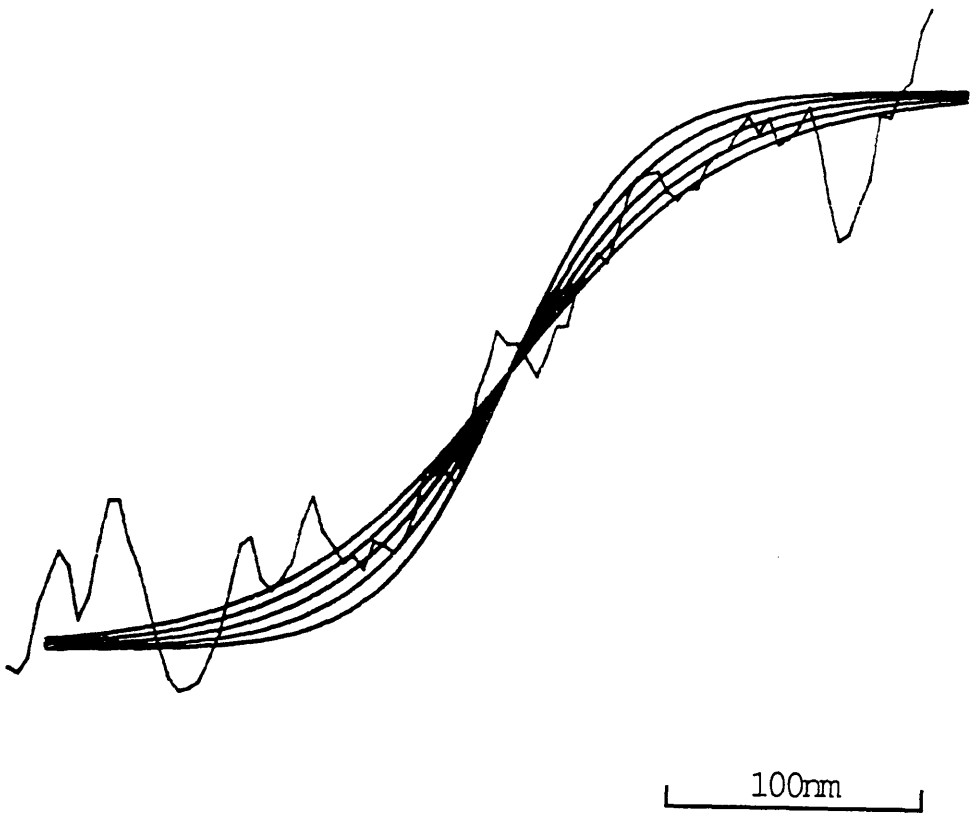

Fig 6.14 Modelling of wall profile by a TANH variation. In this case the profile of a 90^{o} wall in a 20nm thick particle is shown with TANH curves with A values of 40, 50, 60, 70 and 80nm.

profile of a 90° domain wall in a 20nm thick sample is shown with a number of tanh curves drawn over it. Thus even though such a profile contains a quite significant signal variation it is adequately represented by the tanh function (A=70nm in this case). An estimate of the error of this method can be calculated from drawing curves with different A values so that the maximum and minimum A values which can be regarded as reasonable fits can be measured.

The calculation of the wall width by the three definitions are made using the best fit tanh curves. Applying equations (6.2)-(6.4) after substituting in equation (6.5) gives the following values of wall widths for tanh profiles,

$$w_1 = 2A, \qquad w_2 = 1.76A \quad \text{and} \quad w_3 = 4A \qquad (6.6)$$

Wall widths can therefore be calculated using the three definitions and a comparison made with theoretical one dimensional models of Holz and Hubert (1969) who quote values for w_1 and w_2.

Induction profiles of 90° and 180° walls obtained from 20 and 60nm thick samples are shown in figs 6.15 and 6.16 along with the best tanh curve fits in each case. The induction profile given in fig 6.16(b) is from the main wall section of a cross-tie and is therefore really a lower angle wall as discussed in section 6.4.1. Results obtained from these profiles using the three wall definitions are given in table 6.1. Also included are the values of w_1 and w_2 for the theoretical models of Holz and Hubert which were calculated for a material with magnetic constants which correspond closely to those of permalloy.

The results given in table 6.1 indicate that the wall width definition for w_2 provides very good agreement between these experimental results and those predicted from theory. In this case the widths of the four walls

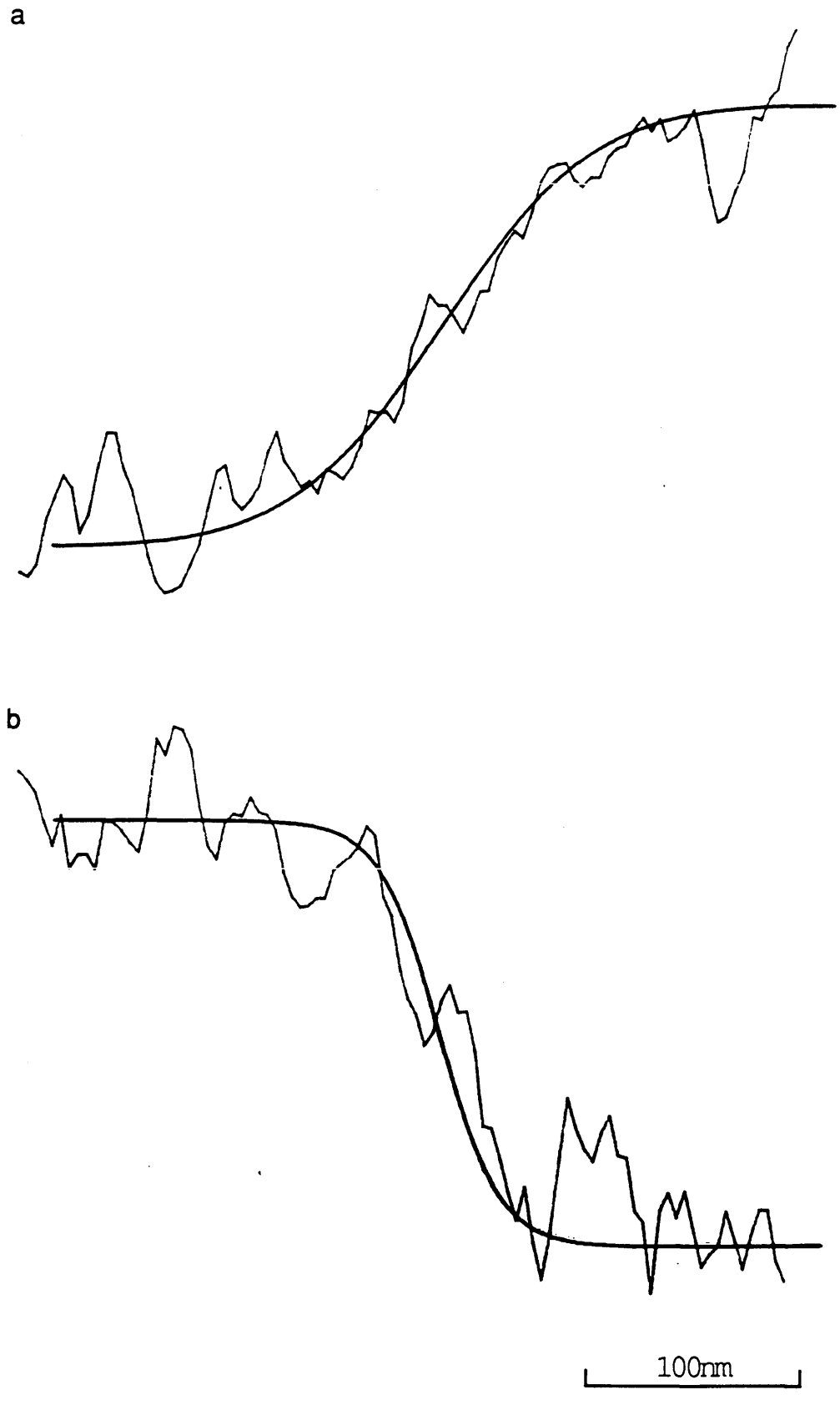

Fig 6.15 Wall profiles from 20nm thick sample with best fit TANH curves. (a) 90° wall with A=70nm curve. (b) 180° wall with A=28nm curve.

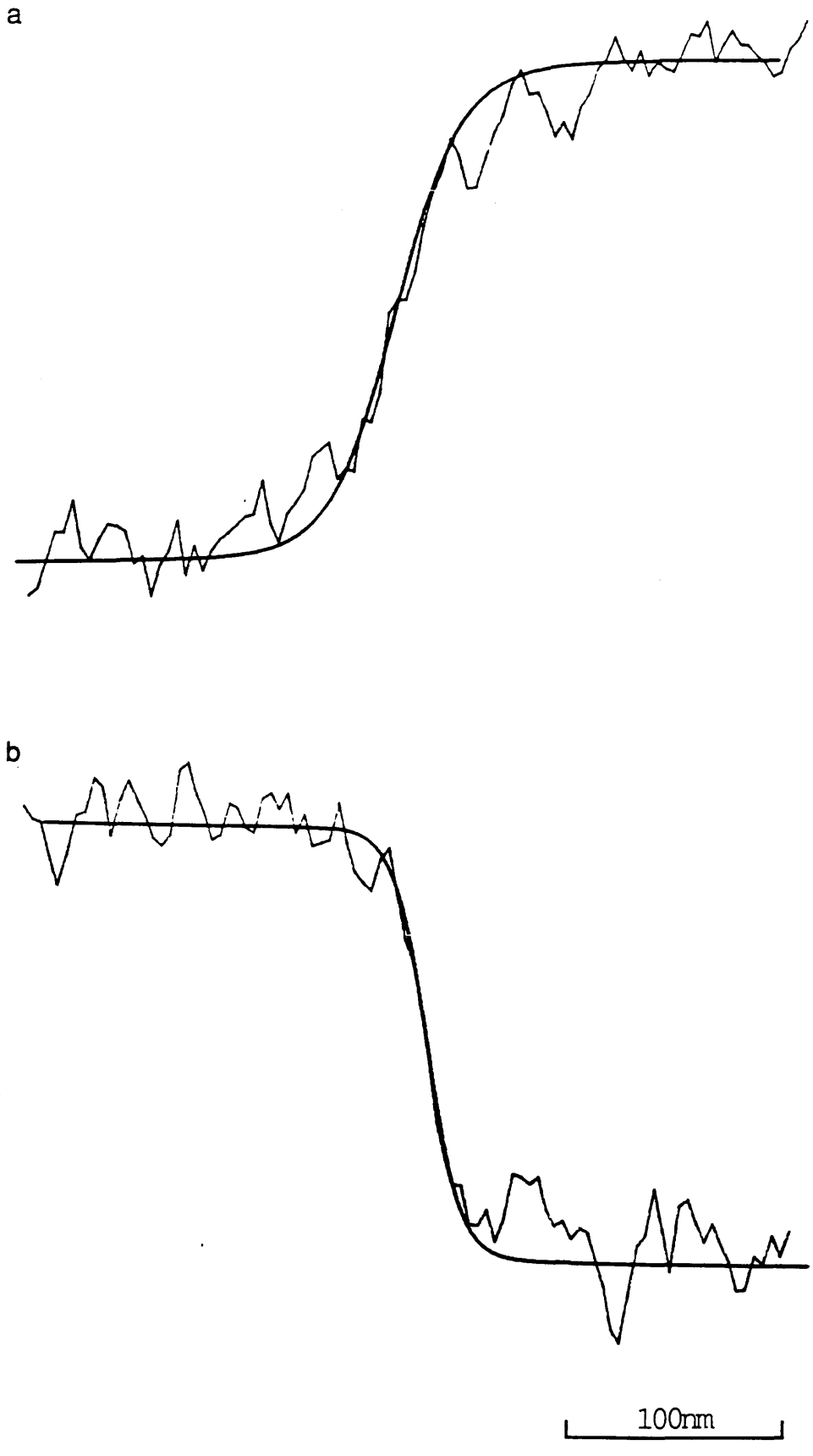

Fig 6.16 As fig 6.15 for wall in 60nm thick sample. (a) 90^{o} wall with A=32nm. (b) 180^{o} (cross-tie) wall with A=16nm.

Table 6.1 Comparison of experimental and theoretical data on domain wall widths.

Wall type (film thickness)	w_1	w_2	w_3
90^o (20nm)	140±20	123±18	280±40
90^o (60nm)	64±8	56±7	128±16
180^o (20nm)	56±8	49±7	112±16
180^o (60nm)	32±4	28±4	64±8

Theoretical values (following Hubert 1970).

90^o (20nm)	440	138
90^o (60nm)	190	63
180^o (20nm)	63	50
180^o (60nm)	38	25

All wall widths quoted are in nm.

considered agree within experimental error from those of the theoretical model. Hubert (1970) showed that the behaviour of w_1 and w_2 for the theoretical model showed the same properties for variation of the film thickness even though the calculated values were considerably different. The discrepancy between the w_1 values is probably due to the fact that this definition relies on the slope of $B_y(x)$ (or $M_y(x)$) at the point of the centre of the wall and for wide walls the rotation in the core region is very much steeper than the tail regions (Collette 1964). Also the tail regions in these walls are predicted to extend for tens of microns from the centre of the wall which would seem to be unfeasible for the particles in question. That the particles dimensions does have an effect on the domain walls has already been observed in the 60nm thick sample from the magnetising experiments (section 5.6). There the cross-tie spacing was noted to be determined by the value of L_2 for the particle and theory (Holz and Hubert 1969) predicts that the tie spacing arises from consideration of the width of the wall sections which make up the cross-tie.

6.5 Summary

In this chapter the magnetisation distributions within the PAT1 particles were re-investigated using the DPC mode of Lorentz microscopy. From the Fresnel observations the regular domain configurations were deduced to have solenoidal magnetisation distributions and confirmation of this was given in section 6.2. Category II structures were not easily interpreted using the Fresnel mode but it was shown in section 6.3 that the observed stray fields indicated the regions at the ends of the particles where $\underline{M}.\underline{n}\neq 0$.

Quantitative information was extracted on the data obtained from domain walls by means of simple image processing techniques. Although the

induction profiles of the walls could not be directly verified, the results taken from modeling the profiles on tanh curves indicated that the walls were of the one dimensional symmetric type. This is expected from theory and the domain wall width measurements also were generally in good agreement with the theoretical values.

CHAPTER 7

INVESTIGATION OF OTHER SHAPES

7.1 Introduction

In this chapter the effect of variation of shape on the domain structure of permalloy particles was studied. The two shapes in particular which were investigated were rhombuses (PAT2) and triangles (PAT3). These shapes were produced by the lithographic process previously described and the two parameters which were varied were L1 and Θ as shown in figs 3.8(a) and (b) for PAT2 and PAT3 respectively. As mentioned in chapter 3 the values taken by these parameters were 1.25, 2.5 and 5μm for L_1 with Θ being 10, 20, 30, 40 or 45^o. Of course the PAT2 particles with Θ=45^o are just simple square shapes identical to those in PAT1. Both patterns were initially studied by the Fresnel mode in CTEM and the results are described in sections 7.2 and 7.3 for particles of thickness 20, 40 and 60nm. It was evident from these studies that some of the particles possessed non-solenoidal magnetisation distributions and the DPC mode allowed a complete picture of the micromagnetic structure to be obtained. In particular an example of particle interaction is given in section 7.5 which shows the advantage of the DPC mode in being able to reveal stray fields directly. The categorisation of domain structures in these shapes is again related to whether flux closure was present or not within the particle i.e. both $\nabla.\underline{M}$ and $\underline{M}.\underline{n}$ are zero within the particle. In this case the classification is just restricted to structures in which flux closure is complete (category I) or incomplete (category II). No sub-division of the categories is made in describing the results in this chapter.

7.2 CTEM Study of PAT2

The results presented in this section are considered in the same order as those in chapter 5 for the PAT1 particles so that the 60nm thick sample is discussed first followed by the 20nm and finally the 40nm thick sample. Sets of micrographs showing typical domain structures are presented as examples of the structures most commonly observed.

7.2.1 60nm Thick Sample

Particles of this thickness tended not to display particularly uniform domain structures. Examples of typical structures revealed by the Fresnel mode are shown in fig 7.1(a)-(e) with (a) corresponding to $\Theta=45^{o}$ and (e) to $\Theta=10^{o}$ as are all sets of Fresnel images given in this chapter. All of these particles had $L_1=2.5\mu m$. Examination of these images suggests that the particles with $\Theta\geq20^{o}$ possess flux closure structures and hence are category I structures. In particular it can be seen that those particles with $\Theta=45$ and 40^{o} (figs 7.1(a) and (b)) have very regular domain structures comprising 4 distinctly separated domains. These images suggest that the magnetisation in each domain is parallel to the nearest edge just like the category I structures seen in PAT1. The structure of the particle with $\Theta=45^{o}$ does, of course, belong to category Ia as it is a square. A schematic representation of the structure of fig 7.1(b) is given in fig 7.2(a) and shows that the angle of rotation of the magnetisation across the domain walls depends on the angle of the vertex in which the domain wall terminates. In this case 80 and 100^{o} domain walls are present in the particle.

A reduction in the value of Θ generally produced complicated domain

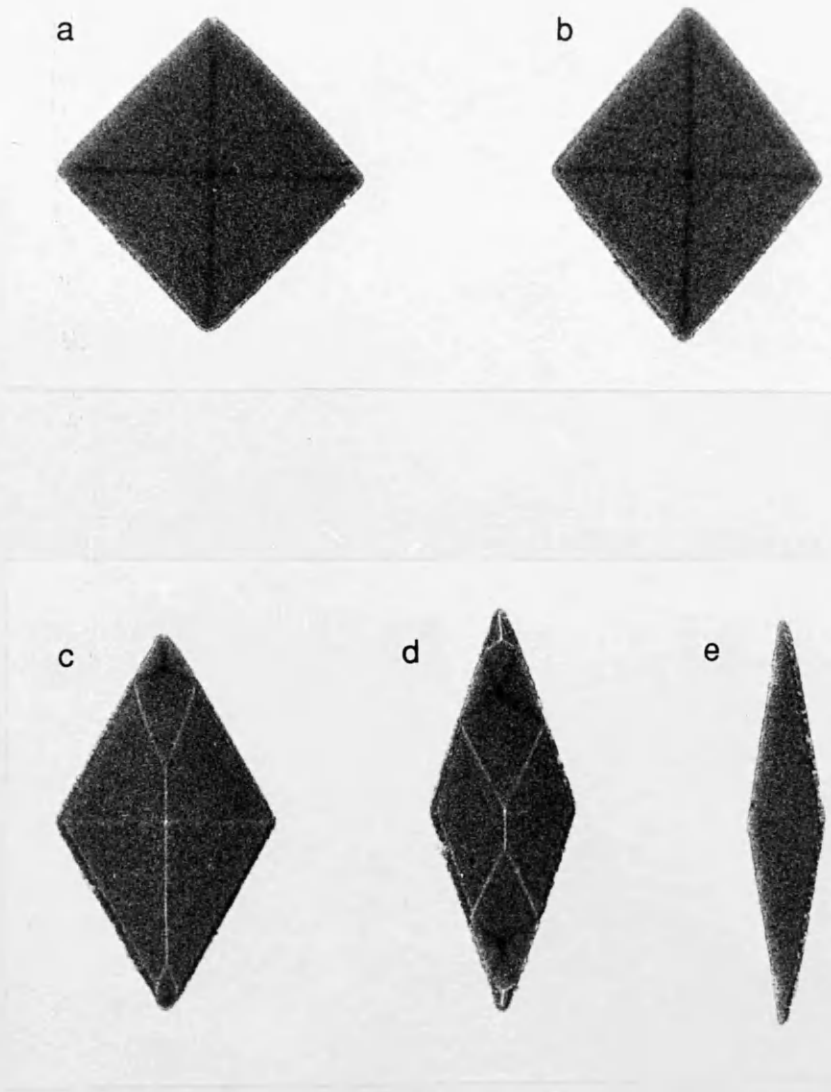

Fig 7.1 Fresnel images from 60nm thick PAT2 particles with L_1=2.5μm. The particles with Θ=45, 40, 30, 20 and 10° correspond to figs (a)-(e) respectively as do all Fresnel images in this chapter.

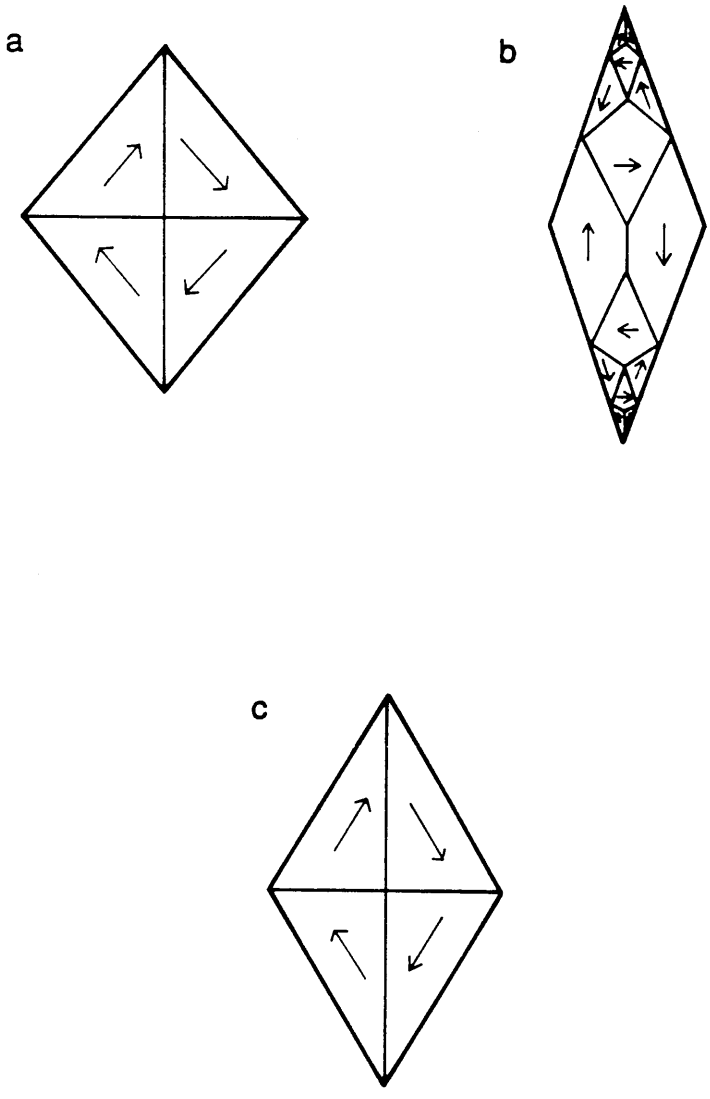

Fig 7.2 Schematic representations of domain structure in PAT2 particles with (a) $\Theta=40^{o}$ (fig 7.1(b)), (b) $\Theta=20^{o}$ (fig 7.1(d)) and $\Theta=30^{o}$ (fig 7.3(c)).

structures as shown by figs 7.1(c) and (d). In both cases the domain structure comprises many small domains in what appears to be a flux closure magnetisation configuration. A schematic representation of the possible magnetisation distribution in these particles is shown in fig7.2(b). Whether flux closure is achieved in these particles is not completely clear from these images alone and further study by means of the DPC mode is required to resolve the structure. The particle in fig7.1(e) shows no discernable magnetic contrast within it and therefore it was concluded to be a single domain particle magnetised along its length. Such particles, which possess category II structures, are not suited for study by the Fresnel mode and results are presented from the DPC investigation in section 7.5.

7.2.2 20nm Thick Sample

The particles in this sample exhibited more regular domain structures than those observed in the 60nm thick sample. Figs 7.3(a) to (e) give an indication of the type of domain configurations present in these particles in which L_1=2.5μm. In figs 7.3(a)-(c) the particles show category I domain structures where flux closure is apparently achieved with four domains separated by domain walls in which the angle of rotation of magnetisation depends on the Θ value of the particle. For example the particle in fig 7.3(b) presumably has a magnetisation distribution as that shown in fig 7.2(a) whereas the particle shown in fig 7.3(c) ($\Theta=30^{o}$) appears to have a domain structure as shown in fig 7.2(c) where the angle of magnetisation rotation in the domain walls is 60 and 120^{o}. The remaining two particles with Θ=10 and 20^{o} have category II structures . The magnetic contrast in these images (figs 7.3(d) and (e)) is not very prominent. Indeed the narrowest particle ($\Theta=10^{o}$) shows no magnetic contrast, as was the case with the

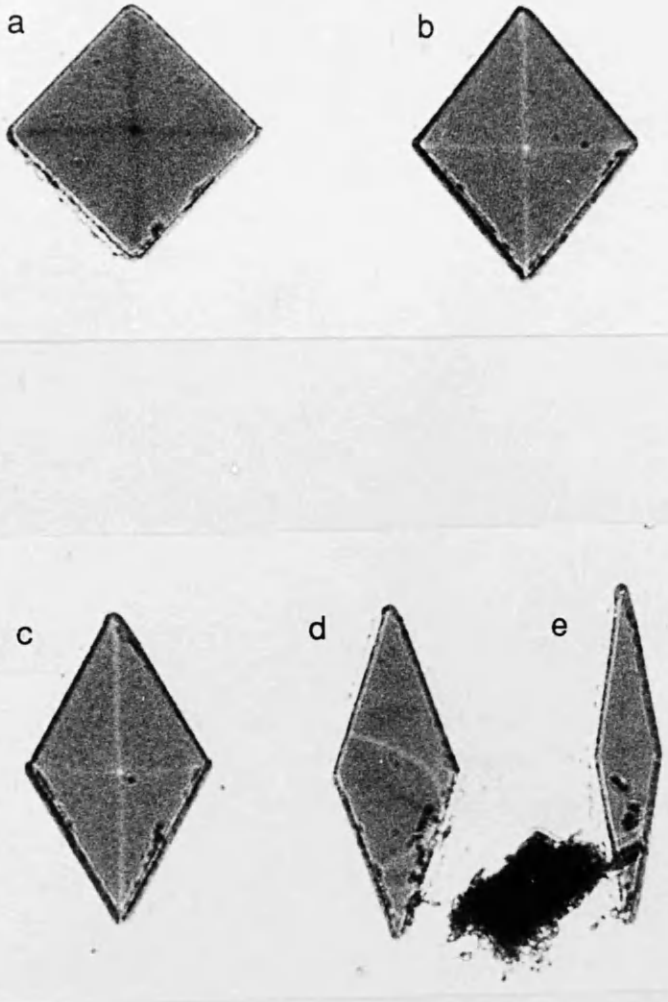

Fig 7.3 Fresnel images of PAT2 particles in 20nm thick sample with L_1=2.5μm.

corresponding 60nm thick particle, indicating that it was probably single domain.

7.2.3. 40nm Thick Sample

The particles in this sample of intermediate thickness were particularly interesting as they tended to adopt very regular domain structures. This is most visibly demonstrated in figs 7.4(a)-(e) for particles with L_1=2.5μm. These images clearly show the transition from single to multi-domain particles, i.e. category I to category II structures. The category I structures are observed in figs 7.4 (a)-(c) and show essentially the basic Ia structure of PAT1. These structures are shown schematically in figs 7.2(a) and (c). This basic domain configuration gives rise to domain walls of various angles as a natural consequence $\underline{M}.\underline{n}\neq 0$.

A reduction in the value of Θ below 30^o resulted in particles with category II domain structures as in figs 7.4 (d) and (e). The complete absence of magnetic contrast in the particle with $\Theta=10^o$ again suggest that it is single domain. By comparison the $\Theta=20^o$ particle shows a little contrast indicating that a slight variation in magnetisation along the length of the particle is present.

7.3 CTEM Study of PAT3

The PAT3 particles at the three thicknesses are now discussed. The domain structures observed had many features in common with those just discussed in the PAT2 particles.

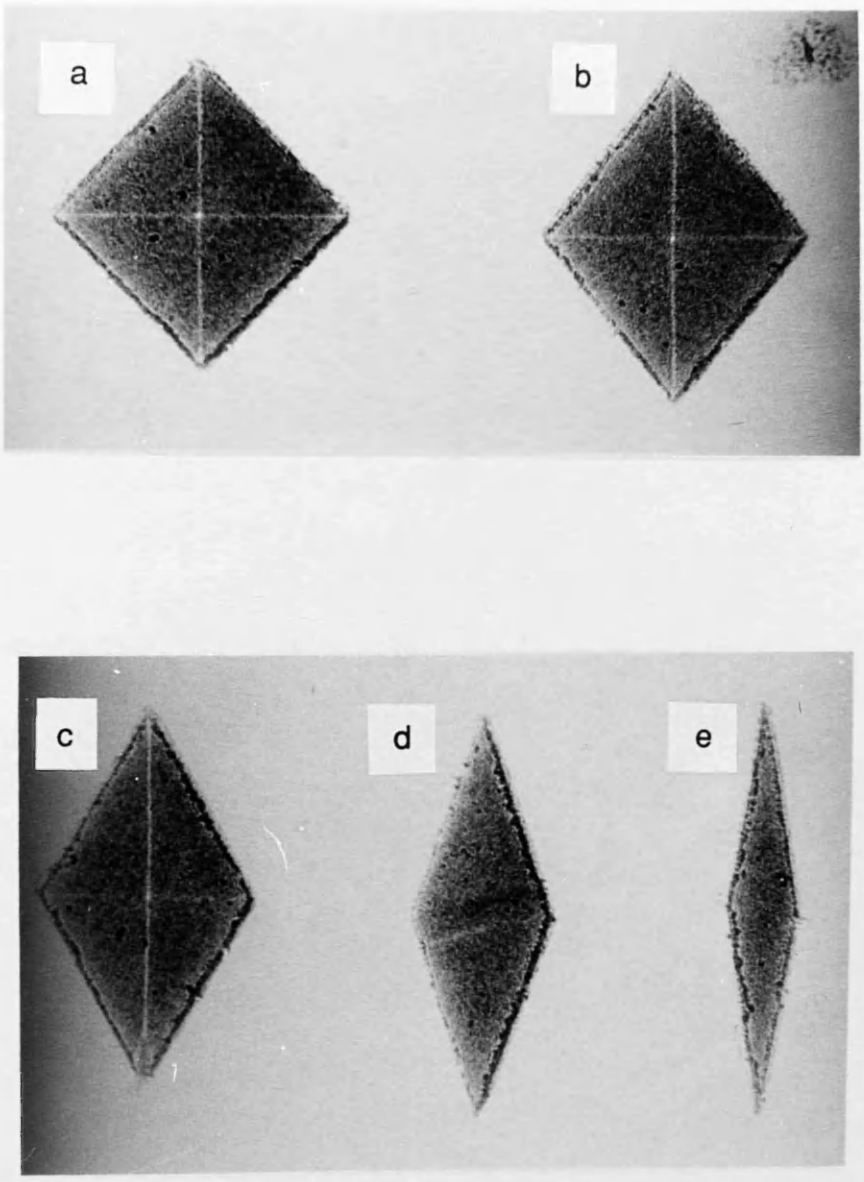

Fig 7.4 Fresnel images of PAT2 particles in 40nm thick sample with L_1=2.5μm.

7.3.1 60nm Thick Sample

At this thickness the particles exhibited complicated structures at large values of Θ and simpler structures at lower Θ values. Typical structures are shown in fig 7.5(a)-(e) for particles with L_1=2.5μm. The structures of the particles in fig 7.5(a) and (b) are not dissimilar to that of the PAT2 particles of the same thickness in fig 7.1(d). An interpretation of the micrograph is given in fig 7.6(a) which shows a possible solenoidal distribution. Such a complex structure seems unlikely to be the lowest energy state for the particle although it shows how flux leakage from the particle can be avoided at the expense of increased length of domain walls. The domain structure present in the $\Theta=30^{o}$ particle in fig 7.5(c) has slightly curved walls and it is unclear as to whether this particle possesses a flux closure structure. A plausible structure is given in fig 7.6(b). At small values of Θ i.e. 10 and 20^{o} no magnetic contrast is visible in the images (fig 7.6(d) and (e)) and the particles appear to be single domain.

7.3.2 20nm Thick Sample

The images from PAT3 particles in this sample showed very little contrast in general. Figs 7.7(a)-(e) give an indication of the low level of contrast in these images compared to those in figs 7.5. Again these particles have L_1=2.5μm and from the images it appears that all of the particles have a non-solenoidal magnetisation distribution. The lack of contrast in figs 7.7(c)-(e) certainly indicates that flux closure is not accomplished in any of these particles. As for the particles in (a) and (b) it does not seem possible to construct a domain configuration which is solenoidal. The schematic diagram in fig 7.6(c) is a possible structure for the particle in fig 7.7(a). Some

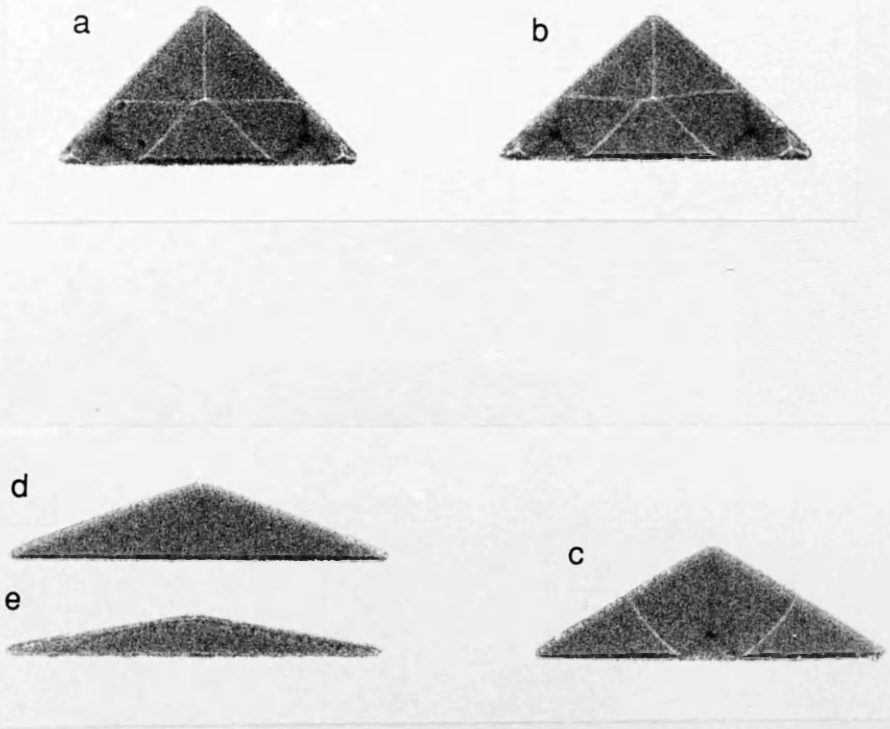

Fig 7.5 Fresnel images of PAT3 particles in 60nm thick sample with L_1=2.5μm.

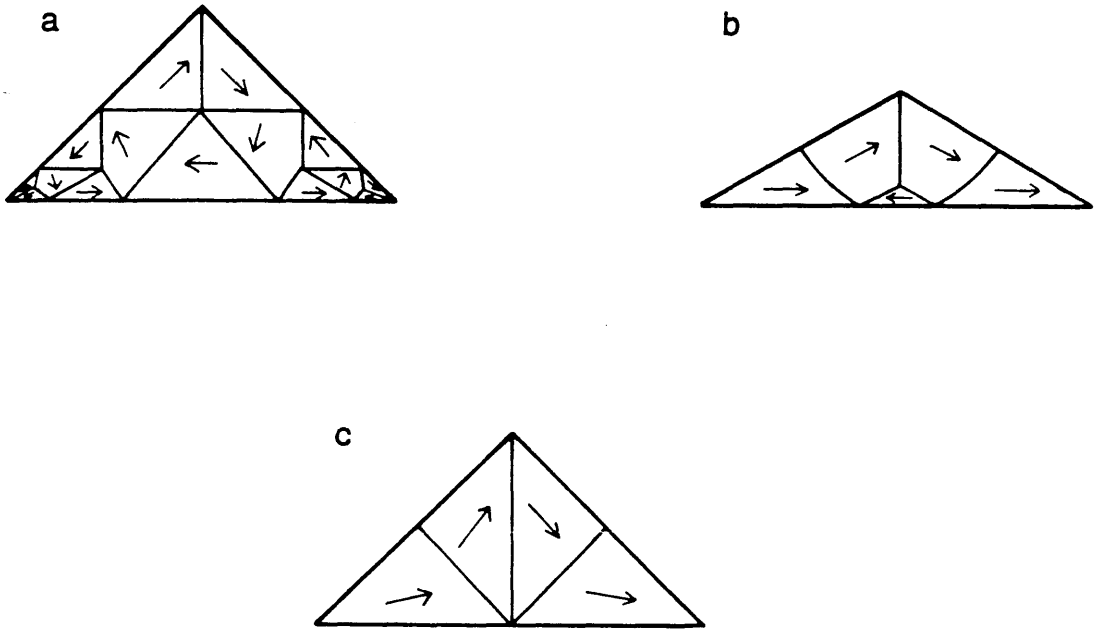

Fig 7.6 Schematic diagrams of domain structures in various PAT3 particles. (a) $\Theta=45^{o}$ (fig 7.5(a)), (b) $\Theta=30^{o}$ (fig 7.5(c)) and (c) $\Theta=45^{o}$ (fig 7.7(a)).

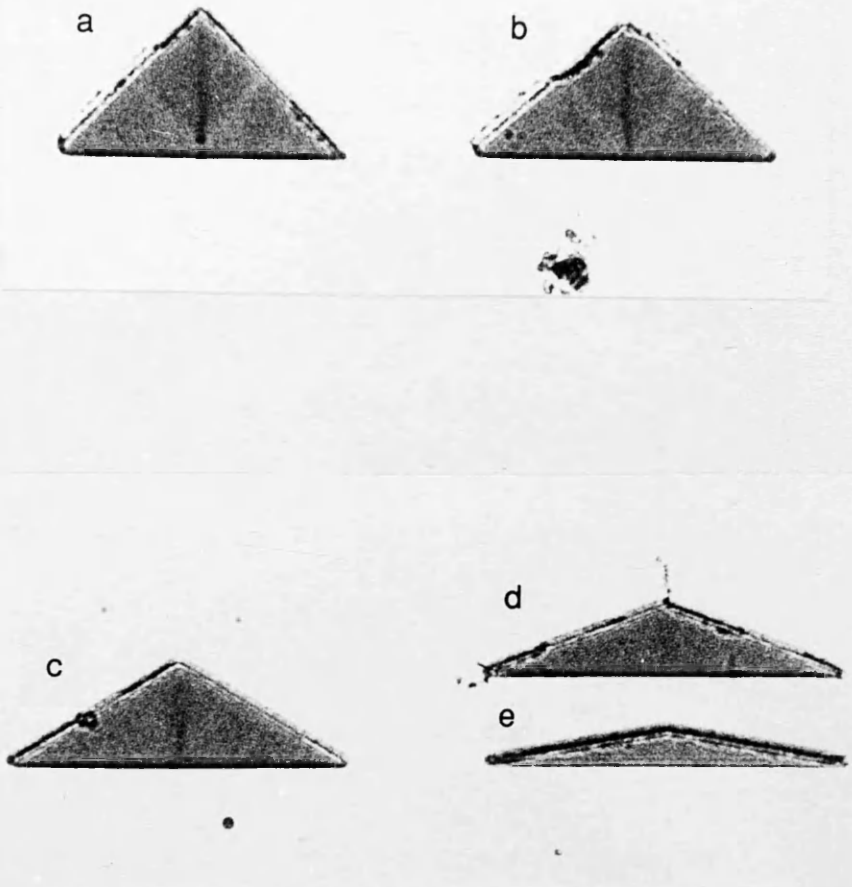

Fig 7.7 Fresnel images of PAT3 particles in 20nm thick sample with L_1=2.5μm.

of the larger particles (with L_1=5μm) did possess what appeared to be flux closure structures and an example is given in section 7.5.

7.3.3 40nm Thick Sample

Particles in the 40nm thick sample displayed almost identical structures to those of the 20nm thick sample. Figs 7.8(a)-(e) show such particles with L_1=2.5μm. Again as Θ decreases the amount of magnetic contrast visible in the particles decreases until they are presumably single domain as in figs 7.8(d) and (e).

7.4 Summary of CTEM Observations

The investigation of the particles of PAT2 and PAT3 by the Fresnel mode of Lorentz microscopy has shown that the shape of the particles significantly affects the domain structure supported. Also the thickness of the particle is a major factor in determining the magnetisation distribution. From the results presented it seems that flux closure is possible in most of the particles with $\Theta \geq 30^{o}$ whereas for $\Theta \leq 30^{o}$ many of the particles displayed little or no magnetic contrast suggesting incomplete flux closure and in some cases uniformly magnetised particles. A notable exception to this was that category II structures seemed to occur for nearly all particles in PAT3 with a thickness of 20 or 40nm. The DPC mode is ideal for observing such particles. As shown in the previous chapter for category II structures in PAT1, the presence of stray field is directly revealed.

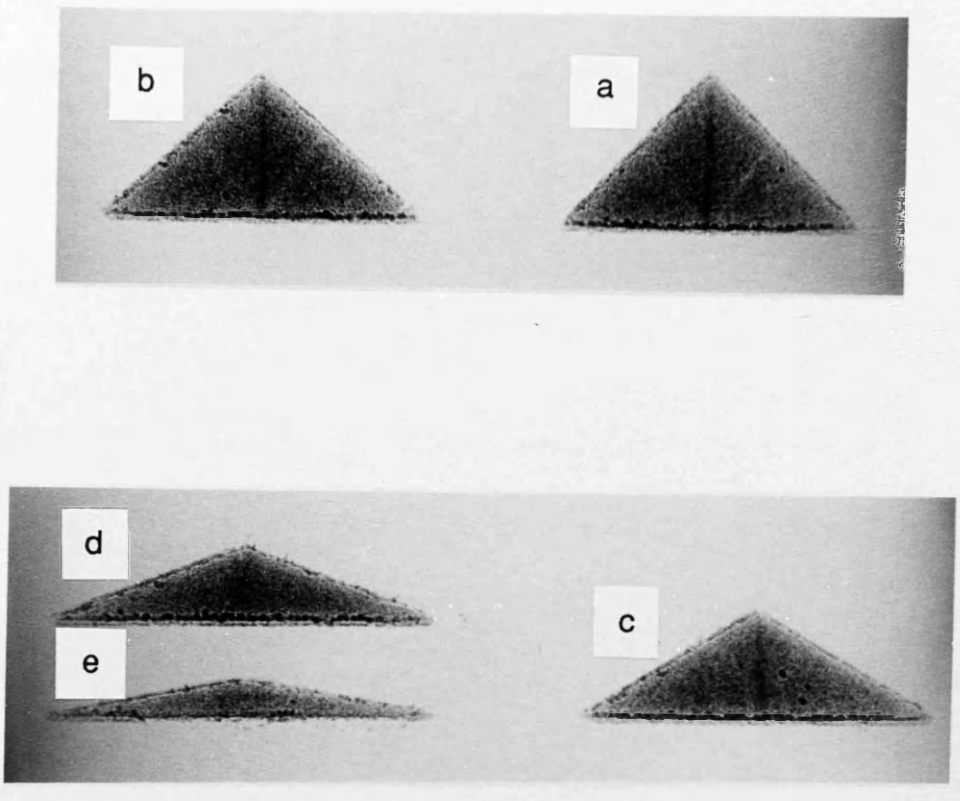

Fig 7.8 Fresnel images of PAT3 particles in 40nm thick sample with L_1=2.5μm.

7.5 DPC Imaging of PAT2 and PAT3 Particles

The DPC mode allowed a fuller study of PAT2 and PAT3 particles than that possible using the Fresnel mode alone. Many of the assumptions made in the previous sections are confirmed along with some observations showing the advantage of using the DPC mode for detecting magnetic contrast. The most notable example is the observation of two interacting particles given in section 7.5.2.

7.5.1 Flux Closure and Near Flux Closure Structures

In the previous sections many of the particles with $\Theta \geq 30^{o}$ appeared to possess flux closure domain configurations (category I). This could not be verified directly from Fresnel observations alone and some of the complicated domain structures were difficult to interpret. An example of the simple flux closure structures is shown in fig 7.9 for a 20nm thick PAT3 particle with $L_1=5\mu m$ and $\Theta=45^{o}$. Such a simple magnetisation distribution is easily reconstructed from these images and is given in fig 7.9(c). The particle supports 3 domains which are magnetised in a direction parallel to the nearest edge and separated by domain walls in which the magnetisation rotates through 90^{o} (at the right angle corner) and 135^{o}. This domain configuration is a good example of the simple domain structure predicted by the Van den Berg (1984) algorithm for solenoidal magnetisation distributions in thin film objects. This structure is not always supported by this shape of particle as can be seen in fig 7.7(a) for a particle of the same thickness but with $L_1=2.5\mu m$.

Another example of a simple flux closure configuration is that of a PAT2 particle of thickness 20nm with L1=5μm and $\Theta=40^{o}$ as in fig 7.10. The

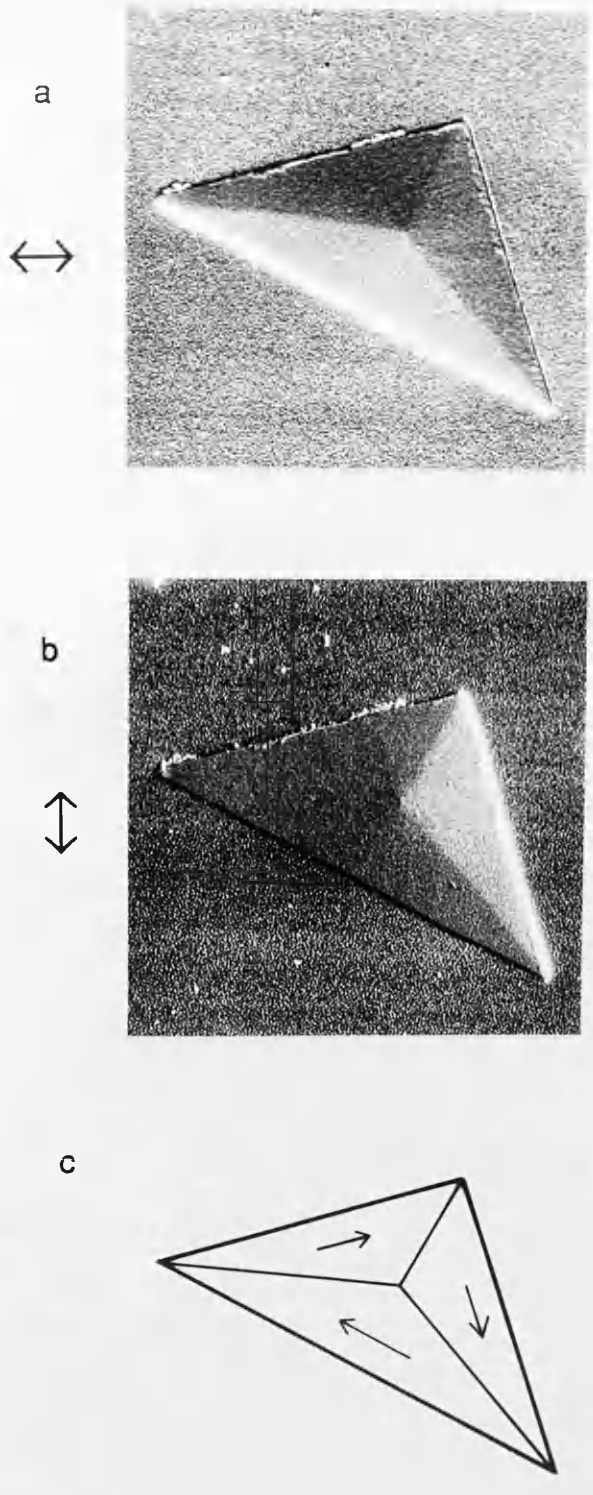

Fig 7.9 DPC images of 20nm thick PAT3 particle with $\Theta=45^{o}$ and $L_1=5\mu m$. The arrows beside the figure indicate the component of induction mapped and the schematic distribution is shown in (c).

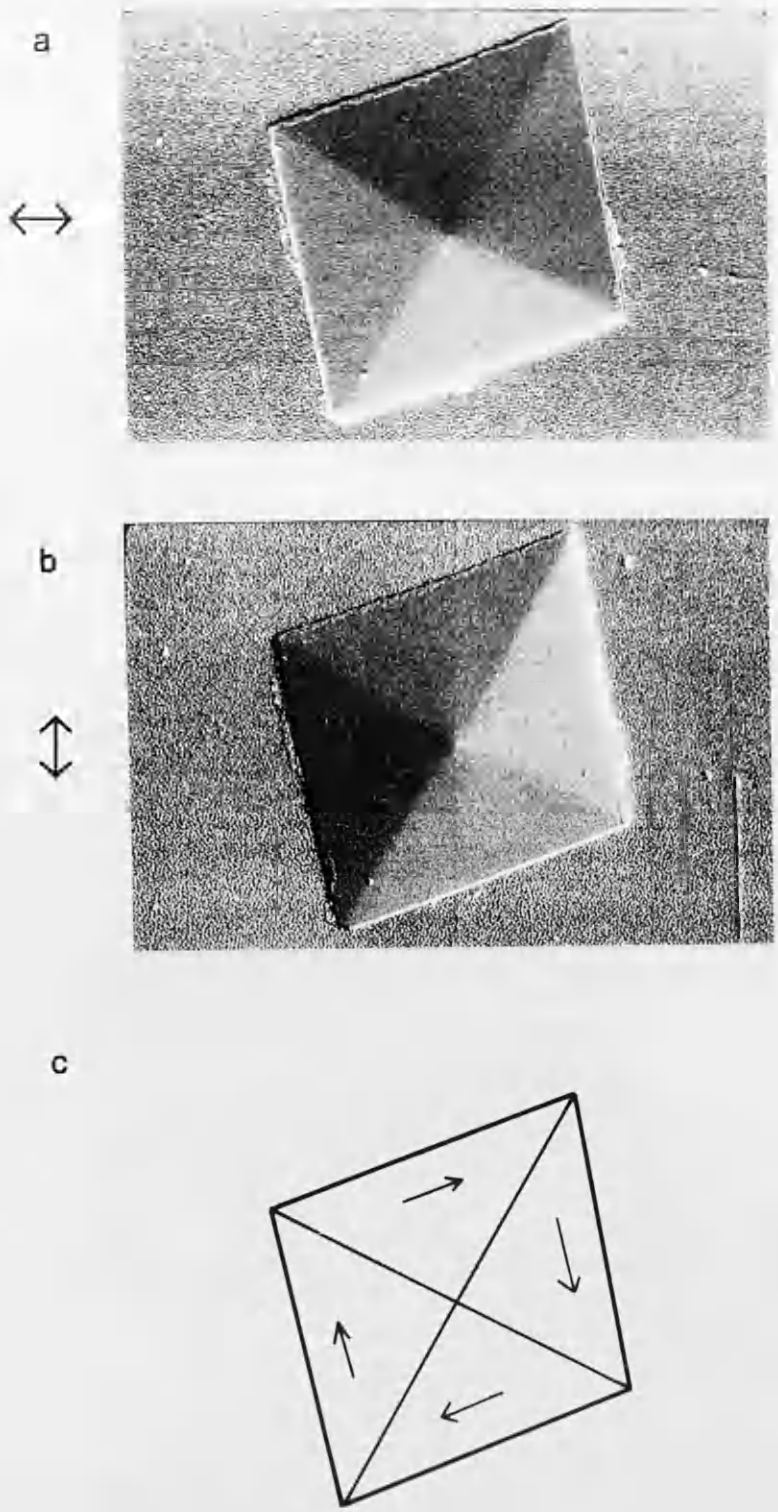

Fig 7.10 DPC images of 20nm thick PAT2 particle with $\Theta=40^{o}$ and $L_1=5\mu m$.

schematic representation given in fig 7.10(c) is very much in the same grouping as the category Ia structures observed in the PAT1 samples. Here the distribution is of four domains which are magnetised parallel to the edges of the particle as in the category Ia case. The difference, in the present situation, is that this leads to the domains being separated by walls where the magnetisation direction rotates through either 80 or 100° depending on the angle of the corner on which the domain wall terminates.

A few of the particles in both sets of shapes were noted to have rather complicated domain configurations, notably those in figs 7.1(d) and 7.5(a). A typical example of this type of structure is shown in fig 7.11 for a PAT2 particle of thickness 60nm and L_1=2.5μm and Θ=20°. It is evident that flux closure is not complete within this particle as the presence of stray field outside of the particle is detected. The schematic distribution is given in fig 7.11(c). It is surprising that this type of particle should accommodate such an irregular and complex structure which does not give flux closure as from the studies in chapter 5 flux closure appeared to be the dominant mechanism in determining the domain structure supported by the particles.

7.5.2 Incomplete Flux Closure Structures

One of the most notable features from the Fresnel observations of the PAT2 and PAT3 particles was the absence of magnetic contrast on the micrographs of many of the particles with Θ=10 and 20°. This suggested that the particles possessed category II structures which in some cases were single domain.

An example of a DPC image of the typical structures seen in the the PAT3 particles is given in fig 7.12 of a 20nm thick particle which has L_1=5μm and Θ=20°. These images confirm that such a particle does not achieve flux

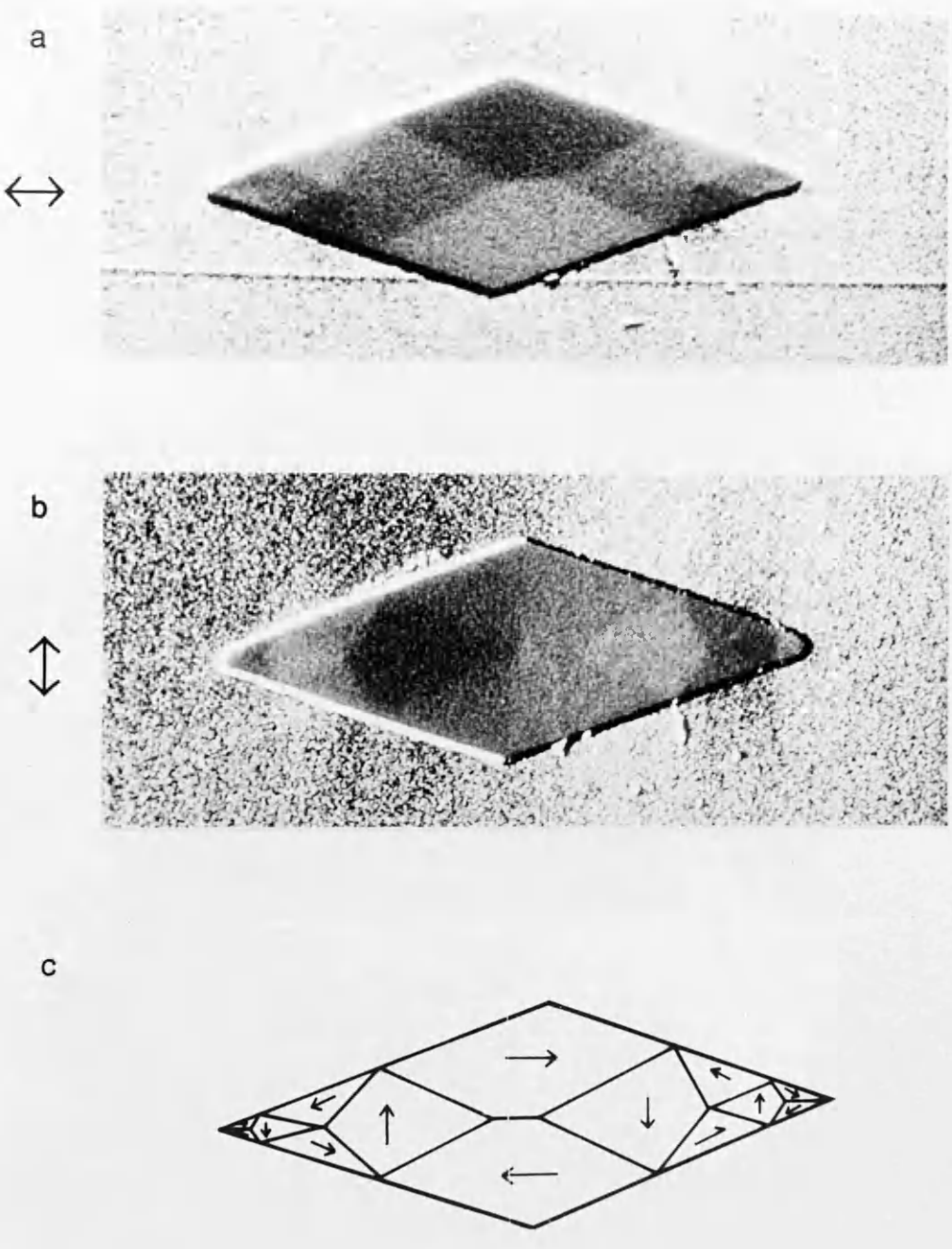

Fig 7.11 DPC images showing domain structure and stray field distribution of a 60nm thick PAT2 particle with $\Theta=20^{o}$ and $L_1=2.5\mu m$.

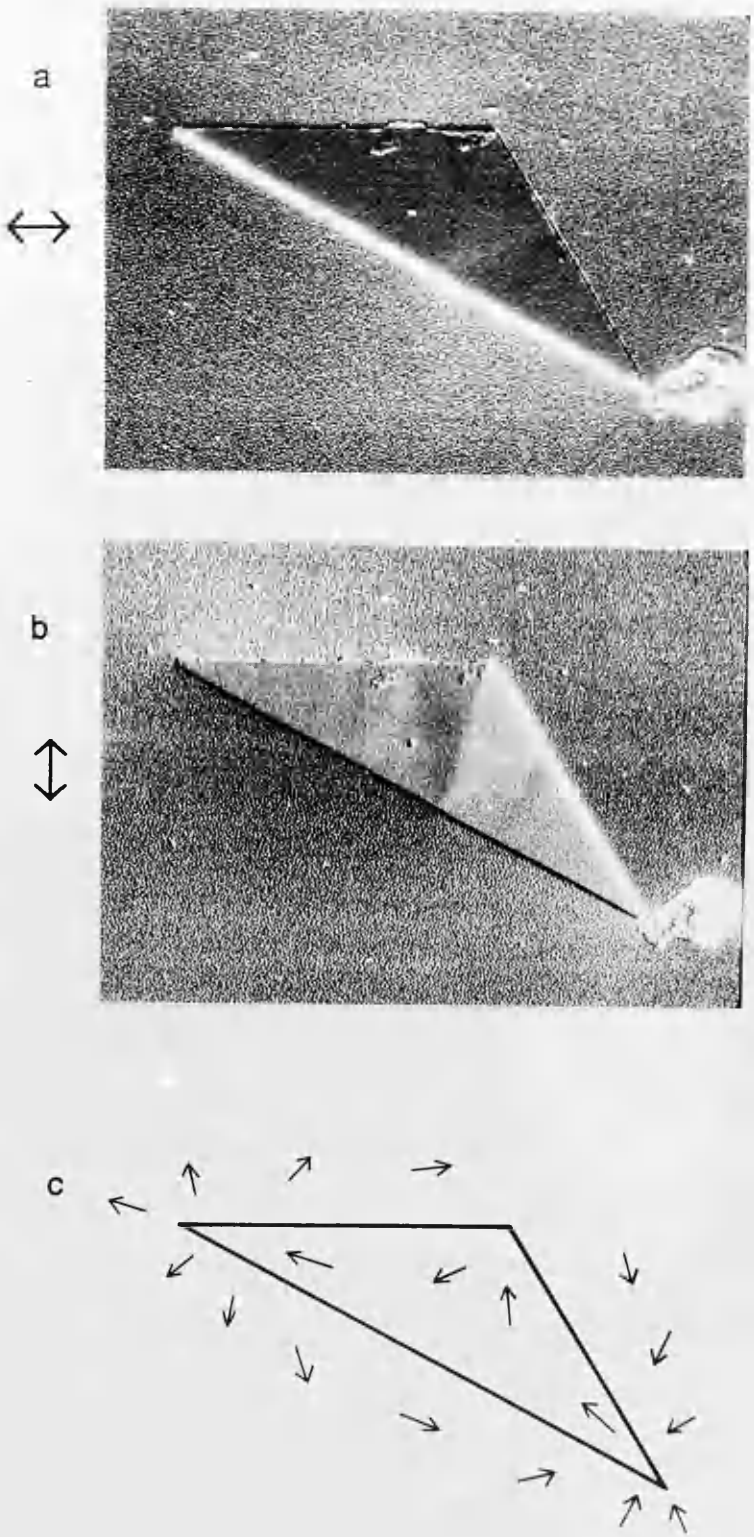

Fig 7.12 DPC images of 20nm thick PAT3 particle with $\Theta=20^{o}$ and $L_1=5\mu m$ showing incomplete flux closure.

closure but is essentially magnetised along its length with a only a small variation in direction as indicated in the schematic diagram in fig 7.12(c). The resulting stray field distribution is also shown.

Almost all of the PAT2 particles with Θ=10 and 20^o displayed no perceptible magnetic contrast using the Fresnel mode. Fig 7.13 shows DPC images of a 60nm thick particle in PAT2 with L_1=2.5μm and Θ=10^o. An interpretation of these images is given in fig 7.13(c) and it is obvious that the particle is uniformly magnetised along its length with stray field being clearly shown to be emanating from the edges where $\underline{M}.\underline{n}\neq 0$. The stray field distribution is consistent with that of a uniformly magnetised diamond shape.

The stray field distributions from single and almost single domain particles as shown in figs 7.13 and 7.14 have established that the stray field distribution of such particles extends to a distance comparable to the width of these particles. When the pattern of particles was initially designed i.e. PAT1 (section 3.3) they were to be produced so that they would be non-interacting and calculations were undertaken to determine a reasonable spacing between the particles. In the case of the PAT2 and PAT3 particles the spacing was roughly chosen in accord with these findings with the exception of the Θ=10 and 20^o which were put very close together as could be seen from the Fresnel images given in section 7.3. From these observations it was noted that the images of these particles possessed very little magnetic contrast. By comparison a pair of DPC images from these particles with L_1=5μm and thickness 60nm is shown in fig 7.14. These images suggest that these particles are indeed interacting. The schematic induction distribution is given in fig 7.14(c). From fig 7.14(a) it is obvious that the two particles are magnetised in the opposite direction from each other. This is to be expected when one considers the stray field distribution of the two particles. With the Θ=10^o particle being uniformly

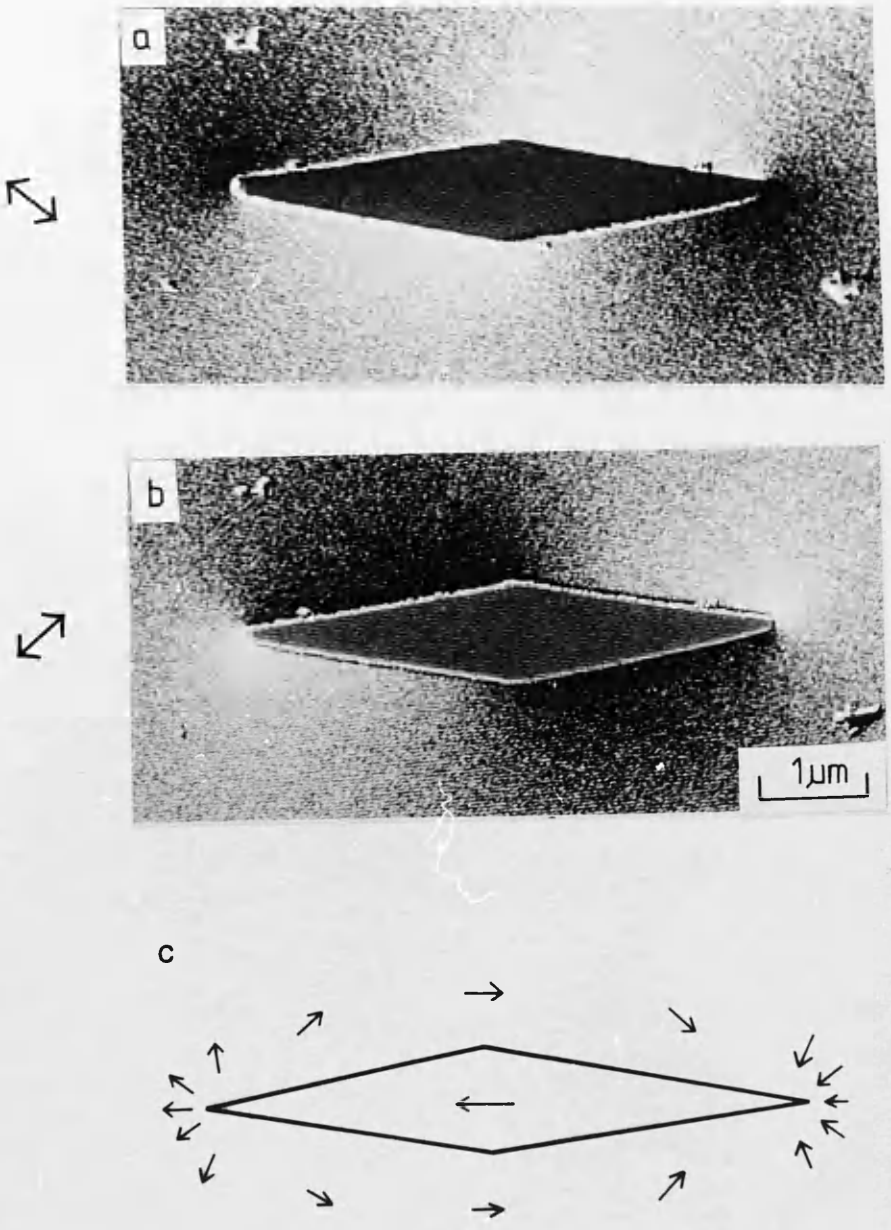

Fig 7.13 DPC images of 60nm thick PAT2 particle with $\Theta=10^{o}$ and $L_1=2.5\mu m$ which is single domain.

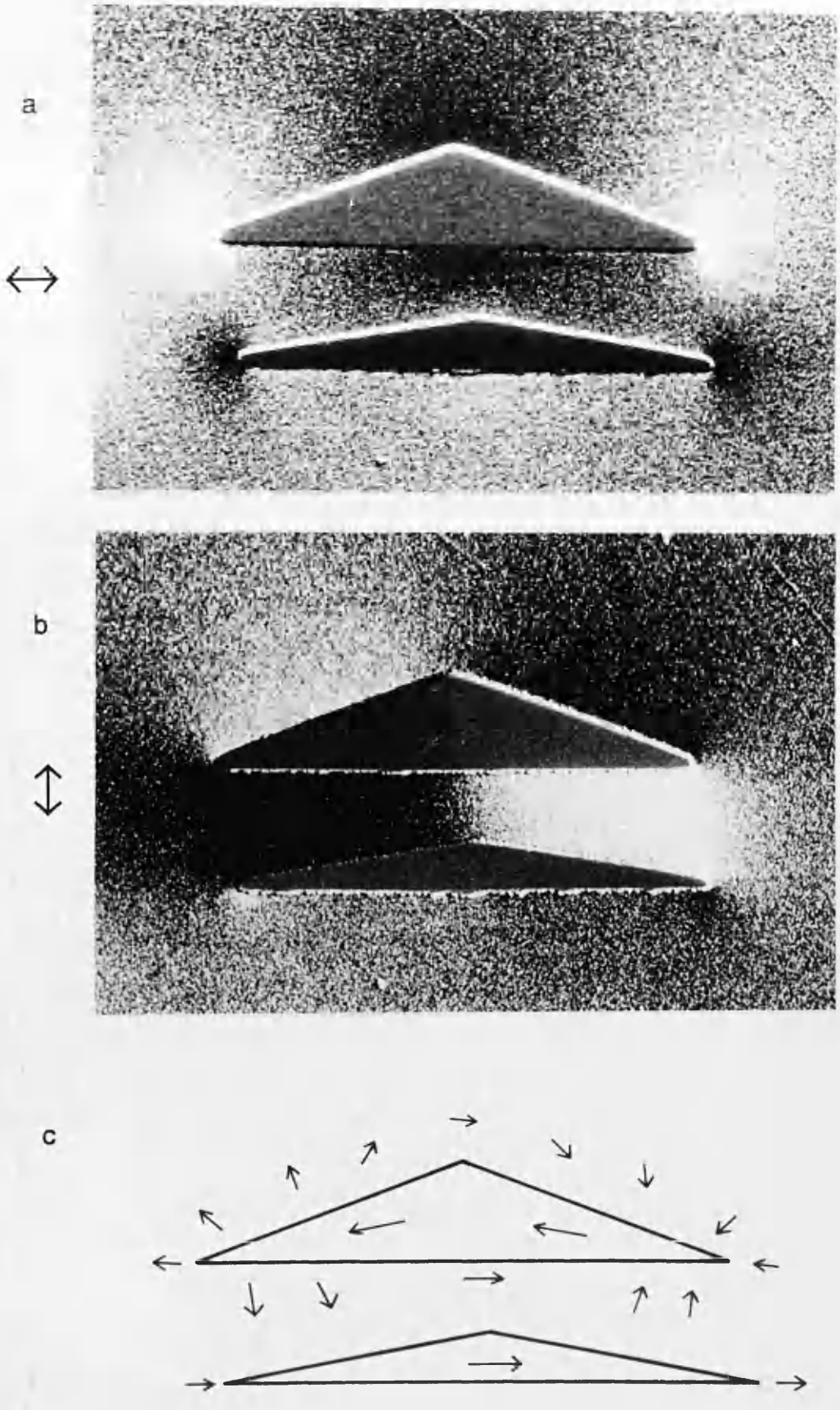

Fig 7.14 DPC images showing interaction between two adjacent 60nm thick PAT3 particles with Θ=10 and 20^{o} and L_1=2.5μm.

magnetised the stray field follows a path between the two surfaces where $\underline{M}.\underline{n}\neq 0$ as was shown in fig 7.12(c). Thus provided the $\Theta=20^{o}$ particle is magnetised in the opposite direction to the lower particle there is an easy return path for the stray field. A configuration with the two particles magnetised in the same direction would lead to an unfavourable stray field distribution and would necessarily be a higher energy state. It is also noted from the DPC images that the upper particle has a slight variation in magnetisation direction along its length although this may not be necessarily due to the stray field from the lower particle.

7.6 Summary

The results presented in this chapter confirm that the particle shape again makes a major contribution to the domain structure supported. Flux closure configurations still appear to be favoured when these particles have $\Theta=45$, 40 or 30^{o}. The structures observed were not as regular as those in the PAT1 particles although there were some exceptions e.g. fig 7.4. As occurred with the PAT1 particles when they were long and thin, incomplete flux closure structures were observed in the PAT2 and PAT3 particles when the angle Θ was reduced to 30^{o} and below. Single domains were supported by many particles with $\Theta=10$ and 20^{o} and in the case of the PAT3 particles it was noted that when two such particles were close together the magnetisation configuration indicated that they were interacting.

CHAPTER 8

CONCLUSIONS AND FUTURE WORK

The work presented in this thesis has shown the characteristics of domain structures in regularly shaped particles of various shapes and thicknesses. By using electron beam lithography and lift-off techniques to generate the shapes the in-plane dimensions of the particles fabricated were of an order of magnitude smaller than those of previous studies e.g. Huijer and Watson (1979). These particles were found to possess very regular domain structures and as such were ideal for the detailed study of domain walls. An attempt was made to classify the domain structures of the square and rectangular particles of PAT1 from observations in CTEM as described in chapter 5. Quantitative information on the micromagnetic structure in the particles was investigated in chapter 6 using the DPC mode in which domain wall widths of the different type of walls observed in the samples were measured. This mode was also used to determine the magnetisation distribution in particles with complex domain structures and also to investigate the stray field distribution from particles possessing incomplete flux closure.

8.1 Conclusions

From observations of the particles in their as grown state given in chapters 5 and 7 it was noted that many of the particles possessed simple flux closure structures. The type of structures seen depended on the shape of the particle and its thickness. Van den Berg's (1984) treatment of the micromagnetics of soft magnetic materials discussed in chapter 1 considers

that flux closure is the dominant mechanism in the formation of the domain structure in thin films when the in-plane dimensions are greater than the critical dimension (~5nm for permalloy). Thus both $\underline{M}.\underline{n}$ and $\nabla.\underline{M}$ are assumed to be zero. His calculations for an ideal soft magnetic material i.e. one with negligible anisotropy, led to the formulation of an algorithm which was demonstrated in fig 1.2. The algorithm can be used to predict the domain structures in any shape of thin film object.

8.1.1 PAT1

The majority of the work in this thesis was involved with the study of the domain structures in the square and rectangular shapes of PAT1. Examples of the domain structures used in the classification of the flux closure magnetisation distributions are given in fig 8.1. The thickness of the particles was shown to be an important factor in the determination of their domain structures and as the 60nm thick sample provided the easiest to classify the results from this sample will be analysed in the greatest detail.

60nm Thick Sample

The domain structures observed in the particles in this sample were notable in that the different flux closure structures were associated with a specific aspect ratio of the in-plane dimensions of the particles. From chapter 5 (table 5.1) it was noted that the two particular types of flux closure structures adopted by the particles were the category Ia and Ib structures. The dominance of these two structures meant that the domains were separated mainly by 90^{o} walls with short cross-tie walls appearing in the Ib structures.

The domain structures predicted by the Van den Berg algorithm for

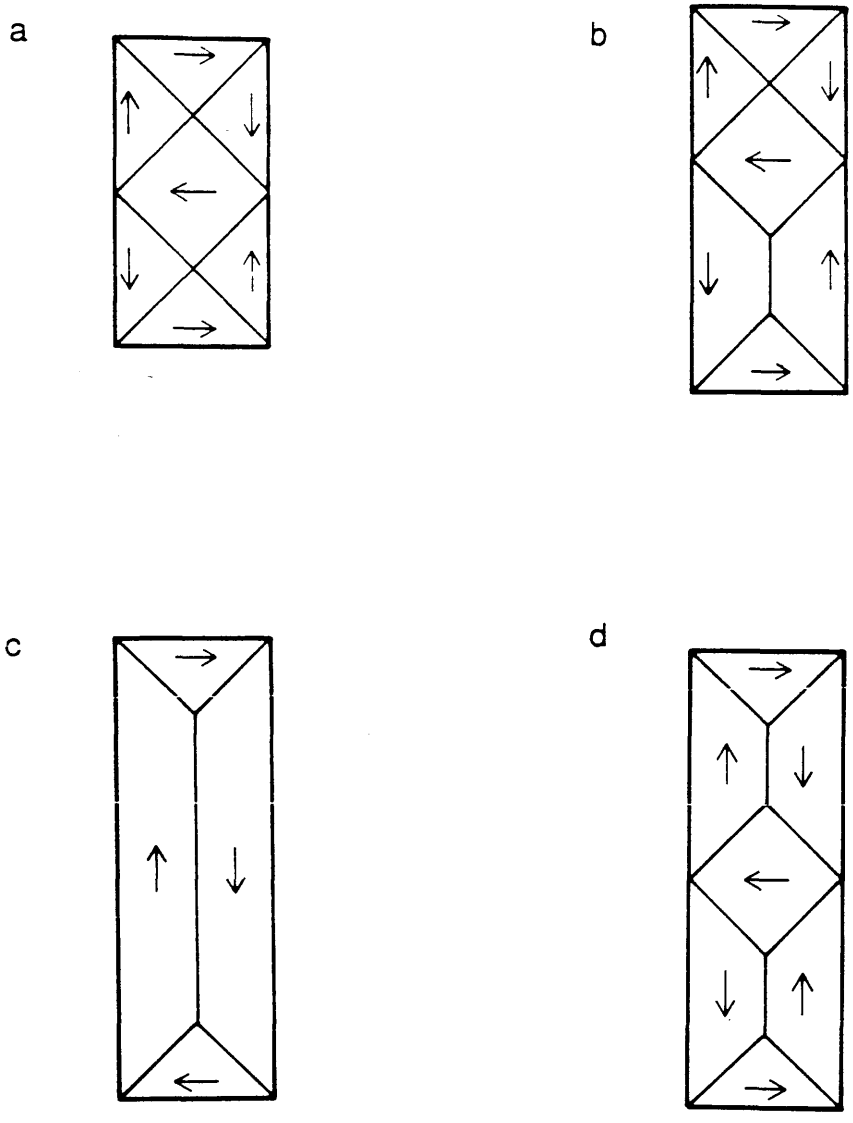

Fig 8.1 Examples of the different domain structures. (a) Ia, (b) Ib, (c) Ic and (d) Id.

rectangular particles indicate that the simplest structures would be expected to be the Ic structure such as that shown in fig 8.1(c). In order to generate the observed domain structures using this algorithm one would need to make at least one subdivision of the object to get these composite structures by then applying the algorithm to the separate areas. The need for these subdivisions and the fact that the predicted simple structures are not seen can be explained by considering the energy of the walls observed in this sample. It has been shown, even from simple wall calculations (Middelhoek 1963), that the energy of a domain wall depends on the angle of rotation of magnetisation across the wall and the thickness of the film so that it is to be expected that the wall energies are an important factor in the determination of the domain structure in the particles. As an example we consider the possible domain structures of a 4 by 2μm particle with Ia and Ic structures such as those shown in fig 8.1(a) and (c) respectively. The energy of these two configurations is given below,

$$E_{Ia} = 2\sqrt{2}\, L_1 L_3\, \sigma_{90}$$
$$E_{Ic} = 2\sqrt{2}\, L_2 L_3\, \sigma_{90} + L_3(L_1 - L_2)\, \sigma_{CT} \qquad (8.1)$$

where σ_{90} and σ_{CT} are the domain wall energy per unit wall surface area for 90^o and cross-tie walls respectively. These relations are true for all integral aspect ratio particles with $n \leq 4$. Now the Ia configuration is possessed by almost all of the integral aspect ratio particles at this thickness so that the following relations may be proposed,

$$E_{Ia} \leq E_{Ic}$$
$$\Rightarrow \sigma_{CT} \geq 2\sqrt{2}\, \sigma_{90} \qquad (8.2)$$

The calculations on domain wall structure and energy discussed in chapter 3 indicate that for permalloy of thickness 60nm the domain walls are expected to be one dimensional symmetric Neel walls (Hubert 1970) although cross-tie walls are energetically more favourable than 180° Neel walls at this thickness (Kosinski 1977). A summary of the quantities of interest is given in table 8.1 where the lower energy of the cross-tie wall is that of Holz and Hubert (1969) which does not include the energy of interaction between the Neel wall sections or the energy of the Bloch lines. Equation 8.2 is thus seen to be consistent with these theoretical predictions.

The above discussion shows that a consideration of the domain wall energies in the particles with flux closure explains why the composite structures are preferred at this thickness to the basic structure predicted by the Van den Berg algorithm. The calculations of the relative domain wall energies were made using equations 8.1 and 8.2 but it is also possible to make estimates of the upper limits for some of the domain wall energies from the observations. In chapter 5 it was noted that the transition from category I to II structures occurred when the aspect ratio of the particles was about 4 for the 60nm thick particles. Now this is obviously an indication that the ratio of magnetostatic to domain wall energy becomes comparable for the expected domain configurations of these particles. For these particles the incomplete flux closure means that the Van den Berg algorithm does not apply. In order to make an estimate of the domain wall energy a comparison is made between the total energy of the observed structure and that of an identical uniformly magnetised particle. The calculation of the energy of the observed flux closure configuration is just that of the domain wall energy whereas the energy of a uniformly magnetised particle was taken from the calculations of Rhodes and Rowlands (1954). It was considered unfeasible to calculate the energy of a category II structure due to its complicated

Table 8.1 Calculated theoretical wall surface energies of the different types of domain walls observed in the 60nm thick sample.

1. One dimensional symmetric Neel 90°	σ_{90}=0.4mJ.m^{-2}
2. Lower energy estimate of cross-tie	σ_{CT} >1.4mJ.m^{-2}
3. Cross-tie	σ_{CT} =3mJ.m^{-2}
4. One dimensional symmetric Neel 180°	σ_{180}=3.2mJ.m^{-2}

Energies from calculations of Holz and Hubert (1969) for 1, 2 and 4 and Kosinski (1977) for 3.

Table 8.2 Comparison of energies of uniformly magnetised (E_S) and Ia structure for particles with L_2 =0.5μm and L_3 =60nm.

L_1 (μm)	E_S (J)	E_{Ia} (J)
1	8.28x10^{-16}	1.7x10$^{-13}\sigma_{90}$
2	8.6x10^{-16}	3.4x10$^{-13}\sigma_{90}$
3	8.71x10^{-16}	5.1x10$^{-13}\sigma_{90}$
4	8.76x10^{-16}	6.8x10$^{-13}\sigma_{90}$

nature. In this case we consider particles with constant L_2 and L_3 and varying values of L_1 with L_1/L_2 taking an integer value. In this case the observations of chapter 5 are used for particles with L_2=0.5μm, L_3=60nm and L_1=1,2,3 and 4μm. The energies of these particles were calculated for a uniformly magnetised particle and for one possessing a category Ia structure which was observed for these particles with n≤4. Table 8.2 gives the values for each with the Ia structure energy being quoted in units of σ_{90}. It is evident from the figures given that E_S, the energy of the single domain particle, increases slightly with increasing L_1 whereas E_{Ia} increases by amounts of $1.7\text{x}10^{-13}\sigma_{90}$ as the aspect ratio increases as shown. From the observations given in chapter 5 it was noted that category Ia structures were accommodated in the 1 by 0.5μm and usually in the 2 by 0.5μm particle whereas the incomplete flux closure category II structures were observed in the 3 by 0.5μm and 4 by 0.5μm particles. Obviously there is no clear transition from the Ia structure to uniformly magnetised particle as the particle presumably achieves a lower energy state in the form of the category II structure. A reasonable proposition would be to conclude that for the 2 by 0.5μm particle the Ia structure is energetically more favourable than the uniformly magnetised state i.e. $E_{Ia} < E_S$. This leads to an estimate of $\sigma_{90}<2.5\text{mJ.m}^{-2}$. From table 8.1 the value for σ_{90} for a 60nm thick film from Hubert's calculations was found to be 0.4mJ.m^{-2}. Considering that category II structures are seen instead of uniformly magnetised particles the value calculated here for σ_{90} of 2.5mJ.m^{-2} is most probably a considerable overestimate although again it must be noted that theoretical calculations were performed for walls in a film with infinite dimensions in the plane of the film.

The energy of the cross-tie walls in this thickness of film from table 8.1 is noted to be $\sigma_{CT}\sim3\text{mJ.m}^{-2}$ (Kosinski 1977). This model was also calculated for an infinite planar sheet and the predicted cross-tie spacing and length

were calculated to be of the order 1-2μm and 4μm respectively for a film of thickness 60nm. In the as grown state only one cross-tie was ever observed in the individual wall sections with the tie length being approximately equal to the L_2 value of the particle. This point is also discussed in section 8.1.3 in the context of the magnetising and anisotropy experiments.

20nm Thick Sample

At a film thickness of 20nm the observed domain structures in the PAT1 particles displayed notable differences from the 60nm thick sample. Again category Ia and Ic flux closure structures were observed but in many of the particles the walls were curved which is not predicted by the algorithm. Clearly the nature of the walls at this thickness of film allow for a variation in the rotation of magnetisation along the length of the wall so that the walls themselves will contain regions where $\nabla.\underline{M} \neq 0$. Also the wall width at this thickness of film are much wider than the 60nm thick sample, as is shown in chapter 6, so that the walls cannot really be regarded as thin lines of discontinuity where the magnetisation performs a sudden jump in its direction.

Category II' structures observed in this sample were noted to be much simpler than those in the 60nm thick sample. The magnetostatic energy of uniformly magnetised particles at this thickness are about an order of magnitude less than those in the 60nm thick sample so that it is to be expected that the flux leakage is not as expensive energetically. This is also reflected in the fact that the transition from category I to II' structures is less distinct in this sample with a few category II' structures being observed in particles with n<4.

Overall the 20 and 60nm thick samples showed that the shape of the particle was critical in determining its domain structure. This is most readily

observed in the appearance of category II domain structures at aspect ratios of about 4. The particles possessing category I structures displayed a variety of domain configurations with the aspect ratio of the particle being a more decisive factor in the determination of the domain structure in the 60nm thick sample.

8.1.2 PAT2 and PAT3

Investigation of variation of the particle shape, derived from the observations of PAT1, indicated that the domain structures in long thin particles did not possess flux closure. This has been attributed to the ratio of domain wall to magnetostatic energy for these particles. The other shapes studied also bore out these findings as was demonstrated in chapter 7 for the PAT2 and PAT3 particles. Flux closure structures were normally observed in the particles with $\Theta \geq 30^{o}$ in both patterns with the simplest structures being similar to the category Ia domain structure in the case of the PAT2 particles. Particles with smaller values of Θ were noted to possess incomplete flux closure structures which in some cases were single domain particles.

8.1.3 Magnetising and Anisotropy Experiments

The most salient points to be drawn from the magnetising and anisotropy experiments discussed in chapter 5 is the non-uniqueness of the domain structure of certain particles. Specifically this has been shown to be dependent on their magnetic history i.e. alignment with respect to the external/anisotropy field. In section 5.6 it was seen that particles with an integral aspect ratio of 4 or less usually possessed either a Ia or Ic domain

structure depending on whether the external field was parallel or perpendicular to the longer in-plane dimension of the particle respectively. This was also true of the anisotropic samples in the as deposited state where particles with larger aspect ratios possessed these structures. Thus it is possible to switch between two stable and simple domain structures by applying an external field in a specific direction.

A further point of note was the observations of the cross-tie walls in these samples. Kosinski's (1977) model for the cross-tie wall predicts that at a fixed film thickness the cross-tie length and spacing will be constant for an infinite planar film. The observations in chapter 5 indicate that the length of the cross-tie was equal to the L_2 value of the particle and the spacing decreased with decreasing L_2. Thus the proximity of edges play an important role in determining the nature of the cross-tie walls. These results are in agreement with the findings of Herman et al (1987) from magnetising experiments.

8.2 Future Work

There are many possible avenues which could be followed from the present work. Those considered of greatest interest are given below:

[1] The magnetising experiments discussed in chapter 5 displayed some very interesting results. Observations of these domain structures were essentially in remanent states and very little could be said of the magnetisation processes which allowed these states to be reached.In order to understand the results of these magnetising experiments it would be useful to be able to apply fields to the particles while they are still in the microscope. Such a magnetising specimen stage would be extremely helpful in the understanding of the dynamic behaviour of these particles as

the changes in the domain configurations could be monitored. This stage could be made with small coils placed either side of the specimen with a variable current source connected to allow control of the field strength. A rotation mechanism for this stage would also be convenient to allow the field to be applied in any direction to the particles without taking them out of the microscope.

[2] Most of the particles made in this work were well separated to ensure that they would be non-interacting. Incomplete flux closure structures were noted to exist in many of the particles fabricated with stray field distributions as shown in chapters 6 and 7. It would be very easy to design patterns of particles with variable spacing so that one could observe the effects of stray fields of the particles on the domain structure of its neighbours. That such interactions do occur was shown for the example of two PAT3 particles in chapter 6. Performing dynamic experiments on these particles with a magnetising stage would also be of interest.

[3] In section 5.7 anisotropic samples were studied by depositing the samples in an aligning magnetic field. Also of interest would be to investigate the domain structures of particles of a material with magnetocrystalline anisotropy. One could then determine the effect of this additional energy consideration on the magnetisation distribution within the particles.

APPENDIX

A.1 Calculation of field of uniformly magnetised block

In chapter 3 the equations required for the calculation of the magnetic field from a uniformly magnetised block were given in order to determine the spacing of the PAT1 particles. The three components of $\underline{H}$ are now calculated from equations (3.6) and (3.7) and the following notation is used for clarity,

$$x\text{-}x' = \alpha \qquad z\text{-}z' = \gamma$$

$$x\text{-}L_1 = a_- \qquad y\text{-}L_2 = b_- \qquad z\text{-}L_3 = c_- \qquad (A.1)$$

$$x\text{+}L_1 = a_+ \qquad y\text{+}L_2 = b_+ \qquad z\text{+}L_3 = c_+$$

Equation (3.6) is now used to give the three components of $\underline{H}$.

Component H_x

The expression for H_x using the substitutions of (A.1) is,

$$H_x = \frac{M_s}{4\pi}\left[\int_{a_-}^{a_+}\int_{c_-}^{c_+} \frac{\alpha\, d\alpha\, d\gamma}{[\alpha^2 + b_-^2 + \gamma^2]^{\frac{3}{2}}} - \int_{a_-}^{a_+}\int_{c_-}^{c_+} \frac{\alpha\, d\alpha\, d\gamma}{[\alpha^2 + b_+^2 + \gamma^2]^{\frac{3}{2}}}\right] \qquad (A.2)$$

which are basically two very similar integrals and if we consider one of these

with the substitution $\omega=\alpha^2+b^2+\gamma^2$ and $d\omega=2\alpha d\alpha$ then,

$$\int_{c_-}^{c_+} d\gamma \int_{a_-}^{a_+} \frac{d\omega}{2\omega^{\frac{3}{2}}} = -\int_{c_-}^{c_+} \left[\frac{1}{[\alpha^2+b^2+\gamma^2]^{\frac{1}{2}}} \right]_{a_-}^{a_+} d\gamma \qquad (A.3)$$

this integral is easily solved and is,

$$\int_{c_-}^{c_+} \frac{d\gamma}{[a^2+b^2+\gamma^2]^{\frac{1}{2}}} = \ln(\gamma+[a^2+b^2+\gamma^2]^{\frac{1}{2}})\Big/_{c_-}^{c_+} \qquad (A.4)$$

Thus the complete expression for H_x is calculated as a sum of many terms like equation (A.4) and is,

$$H_x=\frac{M_s}{4\pi}\{\ln(c_+ + [a_-^2+b_-^2+c_+^2]^{\frac{1}{2}}) - \ln(c_+ + [a_+^2+b_-^2+c_+^2]^{\frac{1}{2}})$$

$$- \ln(c_- + [a_-^2+b_-^2+c_-^2]^{\frac{1}{2}}) + \ln(c_- + [a_+^2+b_-^2+c_-^2]^{\frac{1}{2}})$$

$$- \ln(c_+ + [a_-^2+b_+^2+c_+^2]^{\frac{1}{2}}) + \ln(c_+ + [a_+^2+b_+^2+c_+^2]^{\frac{1}{2}})$$

$$+ \ln(c_- + [a_-^2+b_+^2+c_-^2]^{\frac{1}{2}}) - \ln(c_- + [a_+^2+b_+^2+c_-^2]^{\frac{1}{2}})\} \qquad (A.5)$$

Component H_y

From equation (3.6) the expression for H_y using the notation of (A.1) is,

$$H_y = \frac{M_s}{4\pi}\left[b_- \int_{c_-}^{c_+}\int_{a_-}^{a_+} \frac{d\alpha\, d\gamma}{[\alpha^2 + b_-^2 + \gamma^2]^{\frac{3}{2}}} - b_+ \int_{c_-}^{c_+}\int_{a_-}^{a_+} \frac{d\alpha\, d\gamma}{[\alpha^2 + b_+^2 + \gamma^2]^{\frac{3}{2}}} \right] \quad (A.6)$$

Again we have two double integrals with the basic form this time being,

$$\int_{c_-}^{c_+} d\gamma \int_{a_-}^{a_+} \frac{d\alpha}{[\alpha^2 + b^2 + \gamma^2]^{\frac{3}{2}}} \quad (A.7)$$

Integration with respect to the variable α is a standard formula which then leaves,

$$\int_{c_-}^{c_+} \left[\frac{\alpha}{(b^2 + \gamma^2)(\alpha^2 + b^2 + \gamma^2)^{\frac{1}{2}}} \right]_{a_-}^{a_+} d\gamma \quad (A.8)$$

Solving this integral is fairly complicated requiring a number of substitutions to be made the first being $\gamma = u \tan\theta$ with $u^2 = \alpha^2 + b^2$ and $d\gamma = u \sec^2\theta\, d\theta$, so that the terms from equation (A.8) are of the form,

$$\int_{c_-}^{c_+} \frac{u \sec^2\theta \, d\theta}{[u^2 - \alpha^2 + u^2\tan^2\theta][u^2 + u^2\tan^2\theta]^{\frac{1}{2}}}$$

$$= \int_{c_-}^{c_+} \frac{\sec\theta \, d\theta}{[u^2\sec^2\theta - \alpha^2]} = \int_{c_-}^{c_+} \frac{\cos\theta \, d\theta}{[u^2 - \alpha^2\cos^2\theta]} \qquad (A.9)$$

using the basic rules of trigonometry, and can be further simplified by arranging equation (A.9),

$$= \int_{c_-}^{c_+} \frac{\cos\theta \, d\theta}{[\alpha^2 + b^2 - \alpha^2\cos^2\theta]} = \int_{c_-}^{c_+} \frac{\cos\theta \, d\theta}{[b^2 + \alpha^2\sin^2\theta]} \qquad (A.10)$$

and now the substitution $v=\alpha \sin\theta$ with $dv=\alpha \cos\theta \, d\theta$ means that,

$$= \frac{1}{\alpha} \int_{c_-}^{c_+} \frac{dv}{[b^2 + v^2]} = \frac{1}{\alpha}\left[\frac{1}{b}\tan^{-1}\left(\frac{v}{b}\right)\right]_{c_-}^{c_+} \qquad (A.11)$$

which gives on substituting the variables back gives,

$$= \frac{1}{\alpha b}\tan^{-1}\left(\frac{\alpha}{b}\sin\left[\tan^{-1}\left(\frac{y^2}{[\alpha^2 + b^2]^{\frac{1}{2}}}\right)\right]\right)\Big/_{c_-}^{c_+} \qquad (A.12)$$

This cumbersome expression is essentially the basic form of the component H_y which from equation (A.6) is,

$$H_y = \frac{M_s}{4\pi}\{ \tan^{-1}\left(\frac{a_+}{b_-}\sin\left(\tan^{-1}\left(\frac{c_+}{(a_+^2+b_-^2)^{\frac{1}{2}}}\right)\right)\right)$$

$$- \tan^{-1}\left(\frac{a_+}{b_-}\sin\left(\tan^{-1}\left(\frac{c_-}{(a_+^2+b_-^2)^{\frac{1}{2}}}\right)\right)\right) - \tan^{-1}\left(\frac{a_-}{b_-}\sin\left(\tan^{-1}\left(\frac{c_+}{(a_-^2+b_-^2)^{\frac{1}{2}}}\right)\right)\right)$$

$$+ \tan^{-1}\left(\frac{a_-}{b_-}\sin\left(\tan^{-1}\left(\frac{c_-}{(a_-^2+b_-^2)^{\frac{1}{2}}}\right)\right)\right) - \tan^{-1}\left(\frac{a_+}{b_+}\sin\left(\tan^{-1}\left(\frac{c_+}{(a_+^2+b_+^2)^{\frac{1}{2}}}\right)\right)\right)$$

$$+ \tan^{-1}\left(\frac{a_+}{b_+}\sin\left(\tan^{-1}\left(\frac{c_-}{(a_+^2+b_+^2)^{\frac{1}{2}}}\right)\right)\right) + \tan^{-1}\left(\frac{a_-}{b_+}\sin\left(\tan^{-1}\left(\frac{c_+}{(a_-^2+b_+^2)^{\frac{1}{2}}}\right)\right)\right)$$

$$- \tan^{-1}\left(\frac{a_-}{b_+}\sin\left(\tan^{-1}\left(\frac{c_-}{(a_-^2+b_+^2)^{\frac{1}{2}}}\right)\right)\right)\} \qquad (A.13)$$

Component H_z

The calculation of H_z from equation (3.6) involves solving the following integral,

$$H_z = \frac{M_s}{4\pi}\{\int_{c_-}^{c_+}\int_{a_-}^{a_+} \frac{\gamma\, d\alpha\, d\gamma}{[\alpha^2+b_-^2+\gamma^2]^{\frac{3}{2}}} - \int_{c_-}^{c_+}\int_{a_-}^{a_+} \frac{\gamma\, d\alpha\, d\gamma}{[\alpha^2+b_+^2+\gamma^2]^{\frac{3}{2}}}\} \qquad (A.14)$$

the similarity between this equation and that for H_x in (A.2) is noted so that the calculations are identical with γ replacing α thus the full expression for H_z may be written straight away as,

$$H_z = \frac{M_s}{4\pi}\{ \ln(a_+ + [a_+^2 + b_-^2 + c_-^2]^{\frac{1}{2}}) - \ln(a_+ + [a_+^2 + b_-^2 + c_+^2]^{\frac{1}{2}})$$

$$- \ln(a_- + [a_-^2 + b_-^2 + c_-^2]^{\frac{1}{2}}) + \ln(a_- + [a_-^2 + b_-^2 + c_+^2]^{\frac{1}{2}})$$

$$- \ln(a_+ + [a_+^2 + b_+^2 + c_-^2]^{\frac{1}{2}}) + \ln(a_+ + [a_+^2 + b_+^2 + c_+^2]^{\frac{1}{2}})$$

$$+ \ln(a_- + [a_-^2 + b_+^2 + c_-^2]^{\frac{1}{2}}) - \ln(a_- + [a_-^2 + b_+^2 + c_+^2]^{\frac{1}{2}}) \} \qquad (A.15)$$

A.2 Application to DPC images of cobalt foil.

The above equations can be used to model the stray field distribution from a cobalt foil (McFadyen 1986). The sample used in this case was a large grain polycrystalline cobalt foil and the area studied was a grain in which the c-axis was inclined at a small angle to the foil surface and with the in-plane component of magnetisation normal to the edge of the sample which was 35nm thick. The domain structure of this sample in the area was noted to comprise anti-parallel domains from a lower magnification image. In the area shown in the DPC images of fig A.1(a) and (b) the magnetisation is directed normal to the edge of the sample as shown in fig A.1(c) and results in the stray field distribution shown in the DPC images.

The model proposed to represent this configuration is one of uniformly magnetised blocks placed side by side which are alternately magnetised in opposite directions. The resulting field from such a model is easily calculated from the equations in section A.1. Mapping of the integrated stray field from an array of eight such blocks with the individual dimensions of each block chosen to match the domain size observed in the images (i.e.

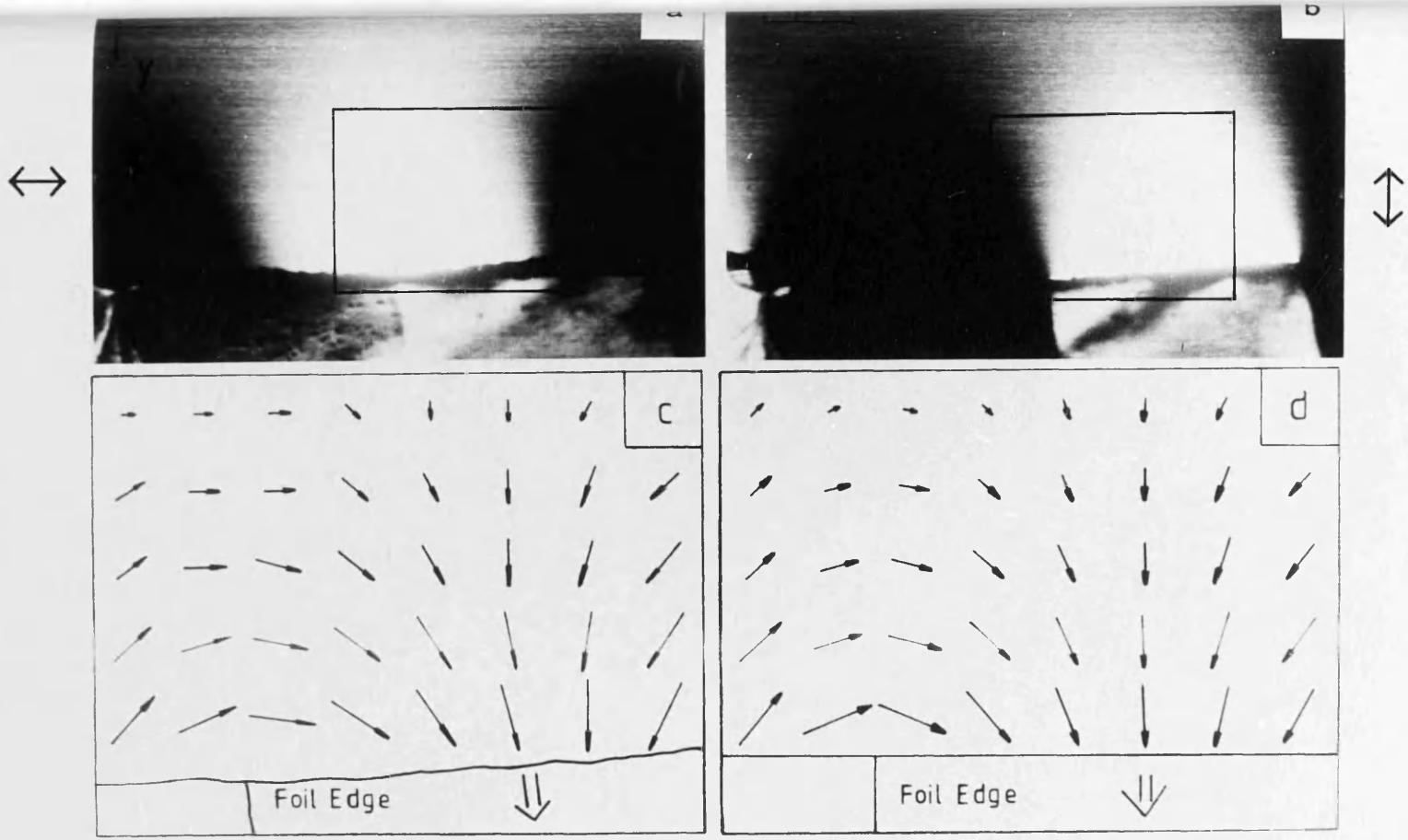

Fig A.1 (a) and (b) are DPC images from a large grain polycrystalline cobalt foil of thickness 35nm. The vector map of the stray field beyond the edge of the film as measured using the DPC images is shown in (c). (d) is the vector map of the theoretical stray field distribution of a model of an array of uniformly magnetised blocks. In both (c) and (d) the arrows drawn are proportional to the logarithm of the integrated component of induction.

$2L_1$=8μm, $2L_2$=100μm and $2L_3$=35nm) was performed using programs in the NAG library which can numerically integrate, with respect to z, the functions for H_x and H_y given in equations (A.5) and (A.6) respectively. The results of these calculations is mapped in fig A.1(d). Comparison of this theoretical model with the experimental results (McFadyen 1986) involved using programs developed on the Toltec computer which allowed the digital images to be processed. Induction maps of the stray field distribution of images such as figs A.1(a) and (b) were produced by subtracting the null induction signal from the two images so that the magnitude of the signals in each image could then be used to determine the integrated value of the respective component of induction. Analysis of figs A.1(a) and (b) in this way resulted in a stray field map shown in fig A.1(c) where the logarithm of the integrated induction is drawn. These results are in excellent agreement with the predictions of the theoretical model in fig A.1(d).

REFERENCES

Chapter 1

R. Becker, Z. Physik, **62**, 253 (1930).

F. Bitter, Phys. Rev., **38**, 1903 (1931).

W. F. Brown, 'Micromagnetics', pubs. Interscience, (1963).

W. Heisenberg, Z.Physik, **49**, 619 (1928).

A. Hubert, Phys. stat. sol., **32**, 519 (1969).

A. E. LaBonte, J. Appl. Phys., **40**, 2450 (1969).

L. Landau and E. Lifshitz, Phys. Z. Sowjetunion, **8**, 153 (1935).

H. A. M. Van den Berg, Ph. D Thesis, Delft University, (1984).

H. A. M. Van den Berg, J. Appl. Phys., **60**, 1104 (1986).

P. Weiss , J. Phys., **6**, 661 (1907).

Chapter 2

Y. Aharonov and D. Bohm, Phys. Rev., **115**, 485 (1959).

B. E. Argyle, B. Petek and D. A. Herman Jr., J. Appl. Phys., **61**, 4303 (1987).

F. Bitter, Phys. Rev., **38**, 1903 (1931).

J. N. Chapman, E. M. Waddell, P. E. Batson and R. P. Ferrier, Ultramicroscopy, **4**, 283 (1979).

J. N. Chapman and G. R. Morrison, J. Magn. Magn. Mater., **35**, 254 (1983).

C. Chorbok and M. Hofman, Phys. Lett., **57A**, 257 (1976).

C. Colliex and C. Mory in 'Quantitative Electron Microscopy', proc. 25th Scottish Universities Summer School in Physics, eds. J. N. Chapman and A. J. Craven, pubs. SUSSP, 149 (1983).

J. M. Cowley, Appl. Phys. Lett., **15**, 58 (1969).

J. M. Cowley, Ultramicroscopy, **2**, 3 (1976).

N. H. Dekkers and H. de Lang, Philips Tech. Rev., **37**, 1 (1977).

J. F. Dillon Jr., J. Appl. Phys., **29**, 1286 (1958).

R. P. Ferrier and R. H. Geiss, Proc.11th. Int. Cong. on Electron Microscopy, eds. T. Imura, S. Maruse and T. Suzuki, Japanese Society of Microscopy, Tokyo, 1725 (1986).

R. P. Ferrier, R. H. Geiss and P. S. Alexopoulos, Proc.11th. Int. Cong. on Electron Microscopy, eds. T. Imura, S. Maruse and T. Suzuki, Japanese Society of Microscopy, Tokyo, 1727 (1986).

H. Gong and J. N. Chapman, J. Magn. Magn. Mater., **67**, 4 (1987).

K. Koike, H. Matsuyama, H. Todokoro and K. Hayakawa, Japn. J. Appl. Phys., **24**, 1078 (1985).

T. Matsuda, A. Tonomura, R. Suzuki, J. Endo, N. Osakabe, H. Umezaki, H. Tanabe, Y Sugita and H Fujiwara, J. Appl. Phys, **53**, 5444 (1982).

G. R. Morrison, Ph. D Thesis, University of Glasgow, (1981).

L. Reimer and H. Kappert, Z. angew. Phys., **26**, 58 (1969).

B. W. Roberts and C. P. Bean, Phys. Rev., **96**, 1494 (1954).

A. Tonomura, T. Matsuda, J. Endo, T. Arii and K. Mihama, Phys. Rev. Lett., **44**, 1430 (1980).

A. Tonomura, H. Umezaki, T. Matsuda, N. Okasabe, J. Endo and Y. Sugita, Phys. Rev. Lett., **51**, 331 (1983).

S. Tsukahara in 'Recent Magnetics for Electronics', ed. Y. Sakurai, pub. OHMSHA Ltd. and North Holland, **15**, 295 (1984).

E. Zeitler, Ultramicroscopy, **9**, 237 (1982).

Chapter 3

F. Bloch, Z. Phys., **74**, 295 (1931).

J. N. Chapman, G. R. Morrison, J. P. Jakubovics and R. A. Taylor, J. Magn. Magn. Mater., **49**, 277 (1985).

R. Collette, J. Appl. Phys., **35**, 3294 (1964).

E. Feldtkeller, Z. angew. Phys., **15**, 206 (1963).

S. R. Herd, K. Y. Ahn and S. M. Kane, IEEE Trans. Mag., **MAG-15**, 1824 (1979).

D. A. Herman Jr., B. E. Argyle and B. Petek, J. Appl. Phys., **61**, 4200 (1987).

A. Holz and A. Hubert, Z. angew. Phys., **26**, 145 (1969).

E. E. Huber Jr., D. O. Smith and J. G. Goodenough, J. Appl. Phys., **29**, 294 (1958).

A. Hubert, Phys. stat. sol., **32**, 519 (1969).

E. Huijer and J. K. Watson, J. Appl. Phys., **50**, 2149 (1979).

J. P. Jakubovics, Phil. Mag., **30**, 983 (1974).

C. Kittel, Phys. Rev., **70**, 965 (1946).

R. Kosinski, Acta Physica Polonica, **A51**, 647 (1977).

A. E. LaBonte, J. Appl. Phys., **39**, 855 (1969).

L. Landau and E. Lifshitz, Phys. Z. Sowjetunion, **8**, 153 (1935).

D. S. Lo, G. J. Cosimini, L. G. Zierhut, R. H. Dean and M. C. Paul, IEEE Trans. Mag., **MAG-21**, 1776 (1985).

I. R. McFadyen, Ph. D Thesis, University of Glasgow, (1986).

S. Middelhoek, J. Appl. Phys., **34**, 1054 (1963).

L. Neel, Compt. Rend., **421**, 533 (1955).

E. J. Ozimek and D. I. Paul, J. Appl. Phys., **55**, 2232 (1984).

P. Rhodes and G. Rowlands, Proc. Leeds Phil. and Lit. Soc., **6**, 191 (1954).

H. Riedel and A. Seeger, Phys. stat. sol. (b), **46**, 377 (1971).

C. Tsang and S. K. Decker, J. Appl. Phys., **53**, 2602 (1982).

Chapter 4

S. P. Beaumont, P. G. Bower, T. Tamamura and C. D. W. Wilkinson, Appl. Phys. Lett., **38**, 436 (1985).

'Electron-Beam Lithography in Microelectronic Fabrication', ed. G. Brewer, pub. Academic Press, chapter 1 (1980).

M. Hatzakis, J. Vac. Sci. Tech., **12**, 1276 (1975).

W. S. Mackie, Ph. D Thesis, University of Glasgow, (1984).

W. S. Mackie and S. P. Beaumont, Solid State Tech., **28**, 117 (1985).

R. Glang and L. V. Gregor in 'Handbook of Thin Film Technology' eds. L. I. Maissel and R. Glang, pub. McGraw-Hill, chapter 7 (1970).

S. A. Rishton, Ph. D Thesis, University of Glasgow, (1984).

F. A. N. Van der Voort and H. A. M. Van den Berg, IEEE Trans. Mag., **MAG-23**, 250 (1987).

Chapter 5

K. L. Chopra, 'Thin Film Phenomena', pub. McGraw-Hill, (1969).

J. W. Edington, 'Electron Diffraction in the Electron Microscope', pub. MacMillan, (1973).

E. Feldtkeller and E. Fuchs, Z. angew. Phys., **18**, 1 (1964).

D. A. Herman Jr., B. E. Argyle and B. Petek, J. Appl. Phys., **61**, 4200 (1987).

E. Huijer and J. K. Watson, J. Appl. Phys., **50**, 2149 (1979).

R. Kosinski, Acta Physica Polonica, **A51**, 647 (1977).

I. R. McFadyen, Ph. D Thesis, University of Glasgow, (1986).

H. A. M. Van den Berg, Ph. D Thesis, Delft University, (1984).

Chapter 6

J. N. Chapman, G. R. Morrison, J. P. Jakubovics and R. A. Taylor, J. Magn. Magn. Mater., **49**, 277 (1985).

R. Collette, J. Appl. Phys., **35**, 3294 (1964).

A. Holz and A. Hubert, Z. angew. Phys., **26**, 145 (1969).

A. Hubert, Phys. stat. sol., **38**, 699 (1970).

J. P. Jakubovics, Phil. Mag. B, **38**, 401 (1978).

R. Kosinski, Acta Physica Polonica, **A51**, 647 (1977).

I. R. McFadyen, Ph. D Thesis, University of Glasgow, (1986).

L. Reimer and H. Kappert, Z. angew. Phys., **26**, 58 (1958).

Chapter 7

H. A. M. Van den Berg, Ph. D Thesis, Delft University, (1984).

Chapter 8

A. Holz and A. Hubert, Z. angew. Phys., **26**, 145 (1969).

A. Hubert, Phys. stat. sol., **38**, 699 (1970).

E. Huijer and J. K. Watson, J. Appl. Phys., **50**, 2149 (1979).

R. Kosinski, Acta Physica Polonica, **A51**, 647 (1977).

S. Middelhoek, J. Appl. Phys., **34**, 1054 (1963).

P. Rhodes and G. Rowlands, Proc. Leeds Phil. and Lit. Soc., **6**, 191 (1954).

H. A. M. Van den Berg, Ph. D Thesis, Delft University, (1984).

Appendix

I. R. McFadyen, Ph. D Thesis, University of Glasgow, (1986).